Technological and design aspects of the processing of composites and nanocomposites

Volume III

University of Minho
Lublin University of Technology
Technical University of Košice

TECHNOLOGICAL AND DESIGN ASPECTS OF THE PROCESSING OF COMPOSITES AND NANOCOMPOSITES

Volume III

Monography

edited by

Prof. **António Gaspar Cunha**, Ph.D., D.Sc.
University of Minho

Prof. **Janusz W. Sikora**, Ph.D., D.Sc.
Technical University of Košice

Guimarães
University of Minho
2020

Scientific-Practical International Workshop
under a Project H2020-MSCA-RISE-2016-734205

This project has received funding from the European Union's Horizon 2020 research and innovation programme under the Marie Skłodowska-Curie Grant Agreement No 734205–H2020-MSCA-RISE-2016

Editors:

António Gaspar-Cunha, Janusz W. Sikora

ISBN 978-989-99344-4-3

PREFACE

Processing of composites and nanocomposites materials constitutes nowadays an important area of research given the growing interest by these types of materials due to its singular properties, namely in what concerns technological and design aspects.

This monography presents the developments taking place in the framework of the NEWEX project during the fourth year of its duration, which is a sequence of other two previous monographies.

The main objective of the NEWEX project entitled “Investigation and development of a new generation of machines for the processing of composite and nanocomposites materials” is the exchange of researchers from the institutions participating in the project. Another important objective consists in develop permanent international and inter-sector collaboration between academic research centres (Lublin University of Technology, Technical University of Kosice, University of Minho) and industrial organizations (Zamak-Mercator LLC and SEZ-Krompachy a.s., Dirmeta UAB).

The contents of this book reflects the work done within the NEWEX project. It starts by presenting the results obtained concerning new concepts for the extruder parts studied and the manufacturing of those extruder parts. Then, some approaches for modelling and optimizing and to study experimentally the process are described, which includes mixing analysis and monitoring. Finally, a practical and state-of-the-art application of the extrusion is identified, namely 3D printing.

It is expected that the nine chapters of this monography be useful to the industry of plastics processing and for scientific organisations dealing with technologies and processing of polymer composites and nanocomposites.

António Gaspar-Cunha
Janusz W. Sikora

TABLE OF CONTENTS

Mirosław Ferdynus[1], Janusz W. Sikora[2], Ľudmila Dulebová[3]

NEW CONCEPTS OF A ACTIVE GROVVED FEED SECTION FOR A NEW GENERATION EXTRUDER – CAD MODELS

Abstract: *The work presents various design concepts of a active grooved feed section (AGFS), geometrically adapted to cech konstrukcyjnych cylindra wytłaczarki. Ten different design solutions of active grooved feed section were presented in the form of CAD models. Next, numerical calculations were carried out aiming at strength and heat analysis of selected models. Numerical calculations were conducted using the method of finished elements. As a calculating tool ABAQUS® program was used. The AGFS was loaded with the torque, the pressure, the torgue and the pressure, as well as with the temperature. Calculations have shown that the proposed active grooved feed section designs are correct, under load they operate in a safe range of stresses, and their operation at a higher temperature is stable.*
Keywords: *extruder, grooves, grooved feed section, CAD*

1. CAD Models

The preliminary assumptions of the presented visualizations are the following:

- Models are made in Catia v5 system as 3D models, they are fully functional. They were tested for their regularity and collision occurrence. Also, virtual prototypes were created to determine the risk of any irregularities during movement.
- In visualizations, some constructional solutions were neglected (joining elements, seals, etc.) as not important in relation to functioning.

The constructional assumptions of an adjustable grooved section are the following:

- The grooved section is 5D long, therefore it is 100 mm,
- The width of the grooves is 6 mm,
- The maximum height of the grooves is 6 mm,
- The inner diameter of the barrel is 25 mm.

Ten different constructional solutions of an adjustable grooved section were presented in the form of CAD models. They are the development of existing

[1] *Lublin University of Technology, Faculty of Mechanical Engineering, Department of Machine Design and Mechatronicsg, ul. Nadbystrzycka 36, 20-618 Lublin, Poland, m.ferdynus@pollub.pl*

[2] *Lublin University of Technology, Faculty of Mechanical Engineering, Department of Technology and Polymer Processing, ul. Nadbystrzycka 36, 20-618 Lublin, Poland, janusz.sikora@pollub.pl*

[3] *Technical University of Kosice, Faculty of Mechanical Engineering, Department of Engineering Technologies and Materials, Masiarska 74, 040 01 Kosice, Slovakia, l.dulebova@tuke.sk*

solutions but also totally new ones. Most of them have innovative advantages and they will be submitted for legal protection in the form of appropriate industrial property rights.

1.1. Concept No 1

The functioning rule of an adjustable grooved section in this concept is the possibility of closing the grooves (section without grooves) and their partial opening (section with grooves) by means of rotating the segments. In Figure 1 an axonometric view of the concept model is presented. The particular elements are also visualised in the exploded view - Figure 2. In this concept, the taper angle of grooves

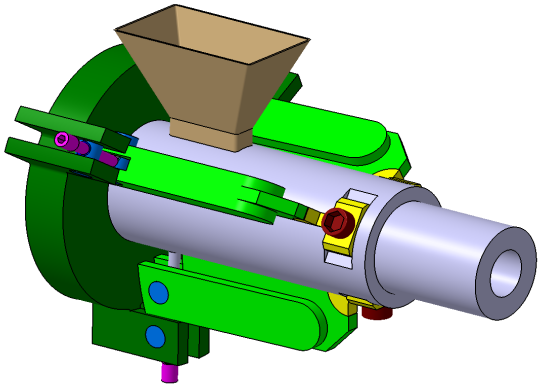

Fig. 1. Concept model No 1. Assembly view

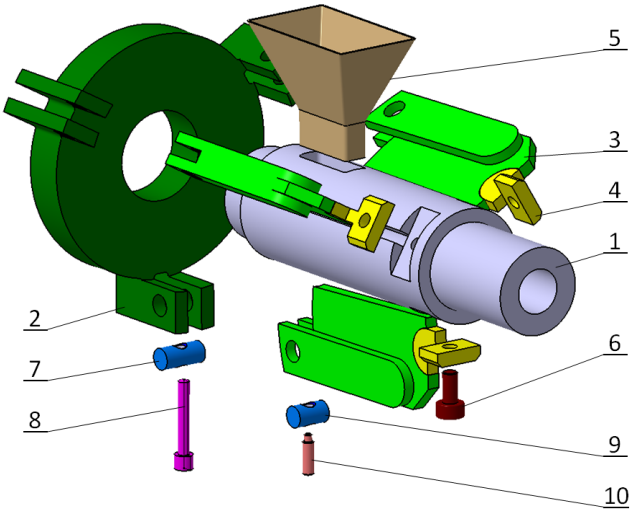

Fig. 2. Concept model No 1. Exploded view: 1 – main sleeve, 2 – fixing plate, 3 – moving segment, 4 – hinge, 5 – hopper, 6 – fixing screw, 7 – front pivot, 8 – adjusting screw, 9 – back pivot, 10 – adjusting metal bolt

can be changed and therefore also the grooves depth can be changed along the grooved section, either in an individual way, independently adjusting each groove, or in a collective way, adjusting all grooves simultaneously.

The closing (lack of screws) and the opening of the grooved section is achieved by rotating the moving segments 3 around the hinge axis 4. The rotation is forced by an adjusting bolt 10. In the moment of achieving an appropriate depth of the groove, the rotational movement of the segment is blocked by means of an adjusting screw 8. In Figures 3 and 4 the visualization of the placement of moving segments is presented in the close (without grooves) and open (with grooves) position.

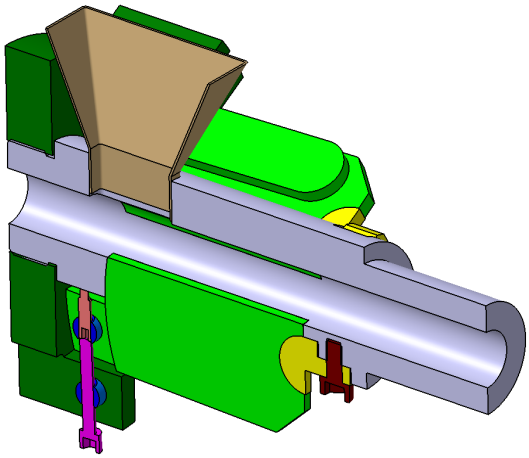

Fig. 3. Concept model No 1 in the placement without grooves (close)

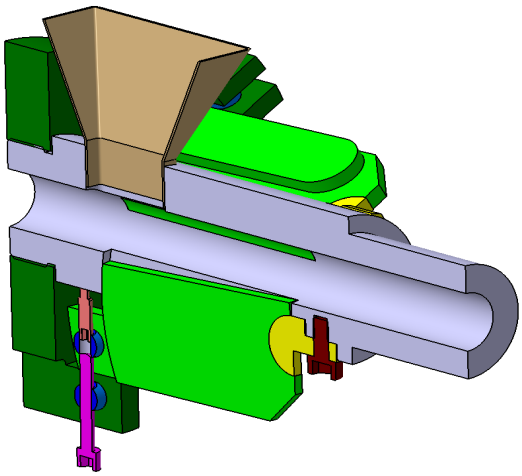

Fig. 4. Concept model No 1 in the placement with grooves (open)

The main elements of an adjustable grooved section are presented in Figures 5, 6 and 7.

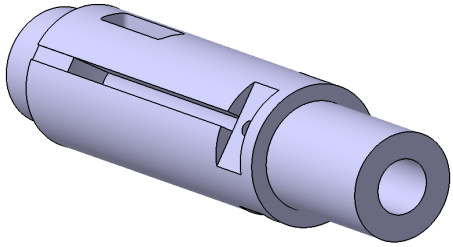

Fig. 5. Concept model No 1 – barrel segment

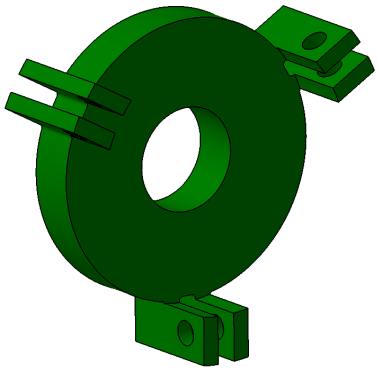

Fig. 6. Concept model No 1 – clamping ring

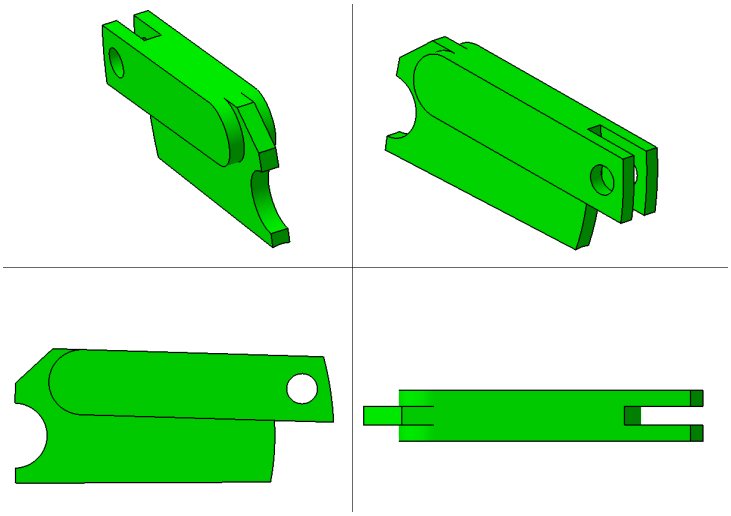

Fig. 7. Concept model No 1 – moving segments

1.2. Concept No 2

The most important thing in concept No 2 is the possibility of creating an adjustable grooved section with torsional grooves, right-hand or left-hand. The grooves can run along the roller (longitudinal grooves) or can have the direction of the helical line (helical grooves). In order to enable that, the main element of the grooved section – the main sleeve has to be fixed at one end, while the other end has to rotate in a right-hand or left-hand direction (within the range of elastic deformation of the sleeve material). This section is presented in Figures 8 and 9.

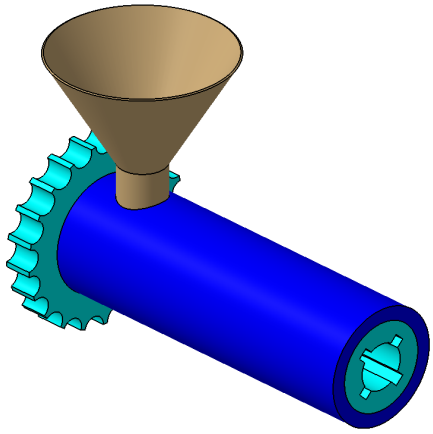

Fig. 8. Concept model No 2. Assembly view

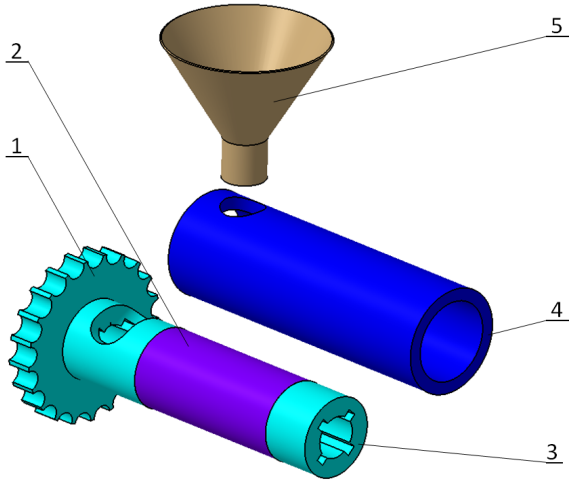

Fig. 9. Concept model No 2. Exploded view: 1 – main sleeve, tensioning part, 2 – main sleeve, flexible part, 3 – main sleeve, fixed part, 4 – barrel, 5 – hopper

In Figures 10 and 11 an adjustable grooved section is presented in the positions when the grooves are longitudinal and when they are helical. The effect of the torsion of grooves is achieved by rotating and blocking the sleeve 1 in a new position, the sleeve 3 should be fixed. The appropriate shape of the opening in the sleeve 1 (Fig. 9) ensures a proper polymer input when the sleeve is in torsion.

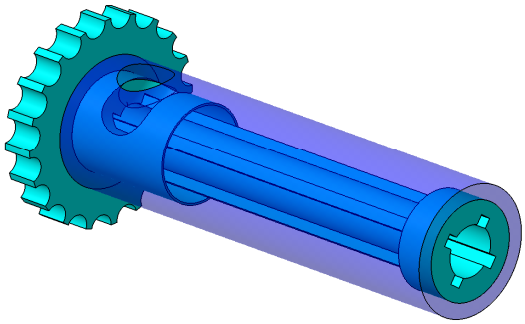

Fig. 10. Concept model No 2. Longitudinal grooves

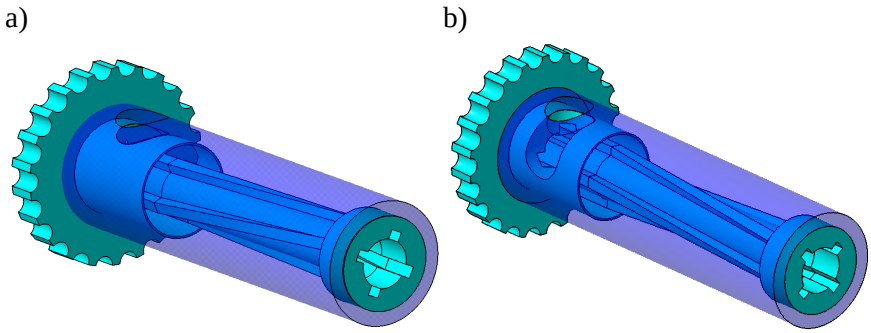

Fig. 11. Concept model No 2. Helical grooves: a) left-hand, b) right-hand

1.3. Concept No 3

Concept No 3 is a modification and significant improvement of concept No 1.

The functioning rule of this adjustable grooved section is the possibility of changing the depth of the grooves along the section without the necessity to stop the extrusion process and make a troublesome exchange of the grooved sleeve. In the assembly Figure 12 the axonometric view of concept model No 3 is presented, the particular elements are shown also in the exploded view (Fig. 13).

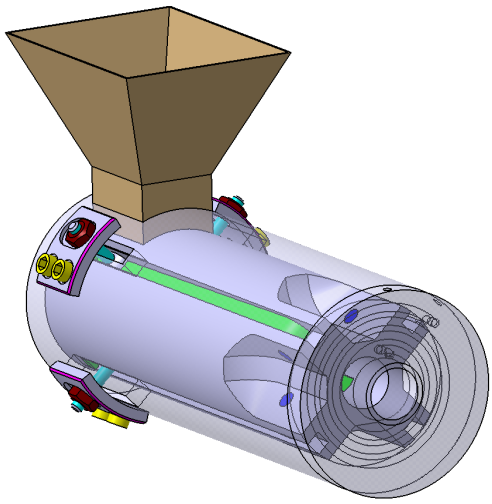

Fig. 12. Concept model No 3. Assembly view

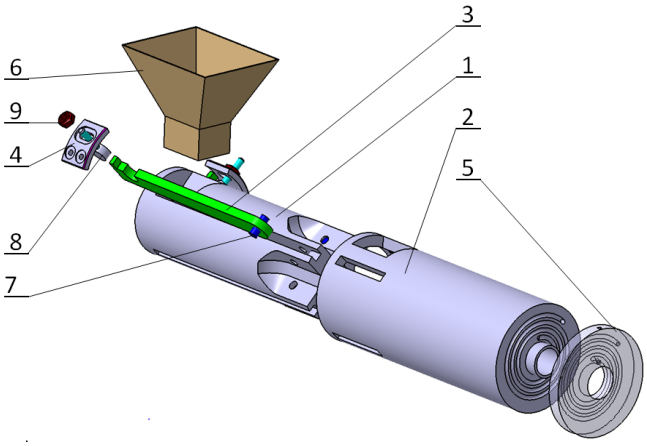

Fig. 13. Concept model No 3. Exploded view: 1 – main sleeve, 2 – barrel, 3 – moving segment, 4 – fixing element, 5 – separating cooling disc, 6 – hopper, 7 – fixing pivot, 8 – adjusting screw, 9 – nut

The closing (smooth inner surface) and opening (grooves) of the grooved section is achieved by rotating segments 3 around the axis of pivots 7. This rotation is forced by an adjusting screw 8. In Figures 14 and 15 the visualization of segment placements in their extreme positions is presented - without grooves (closed position) and with grooves (open position).

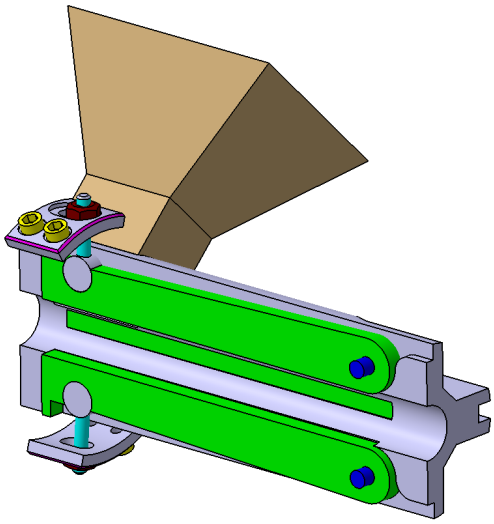

Fig. 14. Concept model No 3 in the closed position (without grooves)

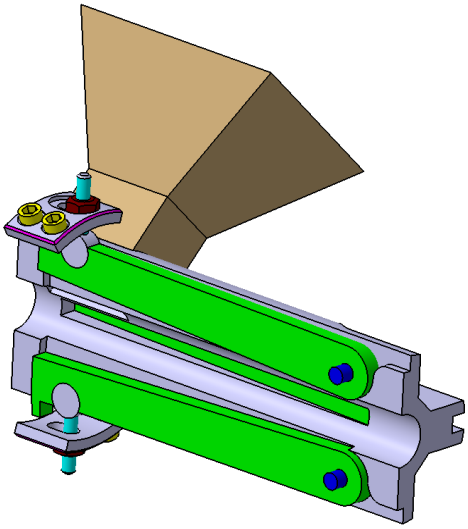

Fig. 15. Concept model No 3 in the open position (with grooves)

The main construction elements of this concept of an adjustable grooved section are presented in Figures 15, 17, 18 and 19.

In the presented solution, the feed section is not cooled intensively, it was decided that the heat section of the plasticizing system will be separated from the feed section

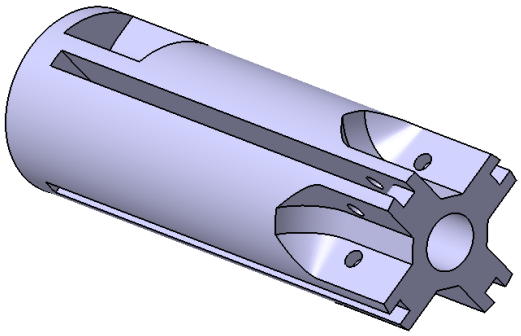

Fig. 16. Concept model No 3 – main sleeve

section by an innovative element – a separating disc (Fig. 18) in which a spiral groove was made. In the front part of the barrel (Fig. 17) a spiral groove was made, whose shape is a mirror of the one made on the disc. The openings through which the cooling agent goes in and out are made on the side surface of the disc and barrel. It is necessary to provide the sealing between the separating cooling disc and barrel.

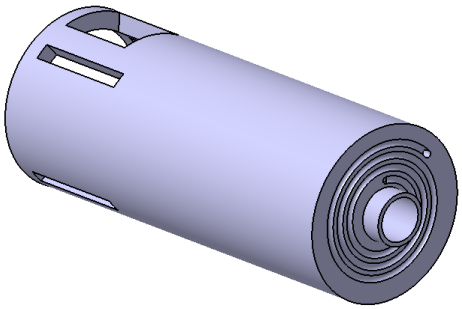

Fig. 17. Concept model No 3 - barrel

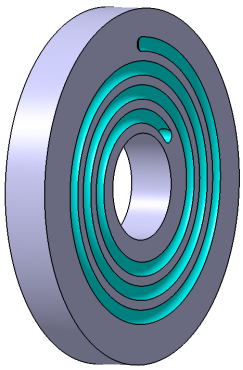

Fig. 18. Concept model No 3 – separating cooling disc

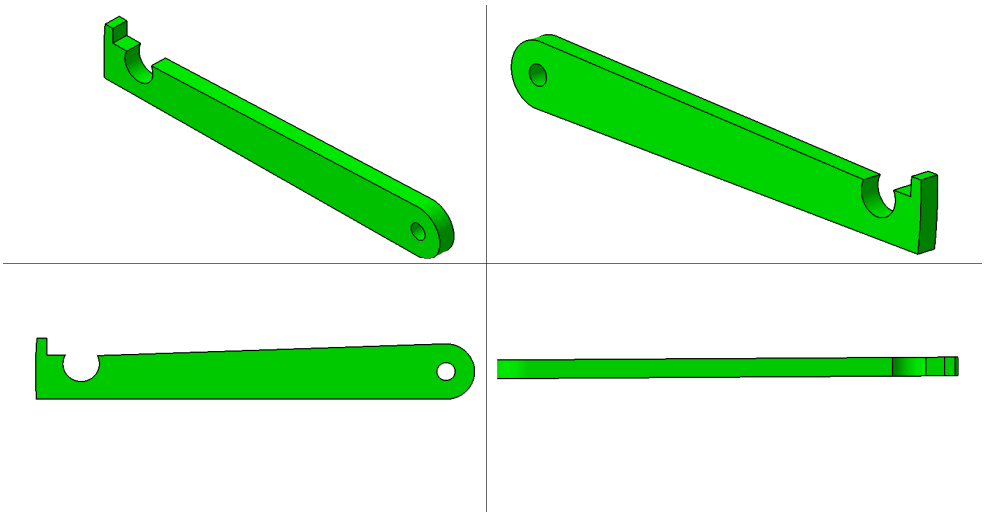

Fig. 19. Concept model No 3 – moving segment

After conducting numerical analysis and computer simulations of temperature distribution, tension and pressure in the grooved section, it was decided to introduce constructional changes, including:

- shortening of the segments,
- modification of the cooling section,
- modification of the adjusting mechanism.

The first two changes caused the constructional changes in most of the elements, including the placement of the rotation axis of the segment.

The improved concept model is presented in Figure 20, while the exploded view in Figure 21.

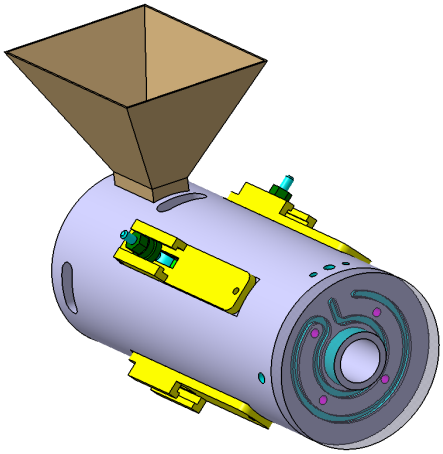

Fig. 20. Modified concept model No 3

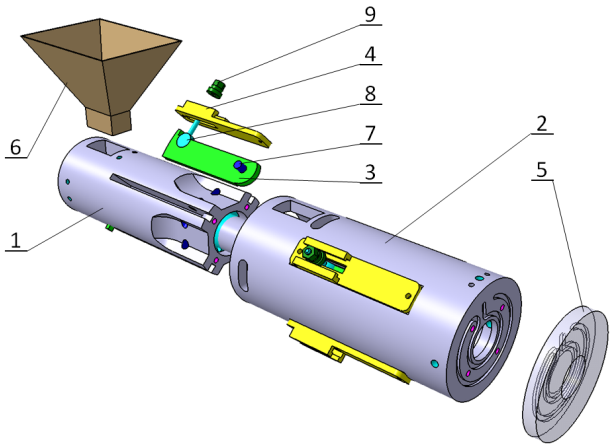

Fig. 21. Modified concept model No 3. Exploded view: 1 – main sleeve, 2 – barrel, 3 – moving segment, 4 – fixing element, 5 – separating cooling disc , 6 – hopper, 7 – rotational pivot, 8 – adjusting screw, 9 – special nut

The grooves in the grooved section are obtained by rotating the segments 3 around the axis of pivots 7. This rotation is forced by an adjusting screw 8. In Figures 22 and 23 the visualization of segment placement is presented - in a closed position (without grooves) and in an open position (with grooves).

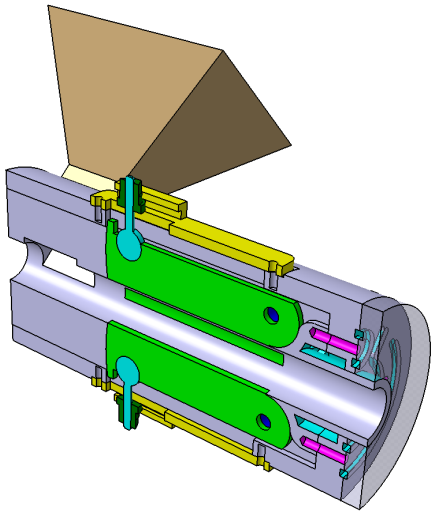

Fig. 22. Modified concept model No 3 in a closed position (without grooves)

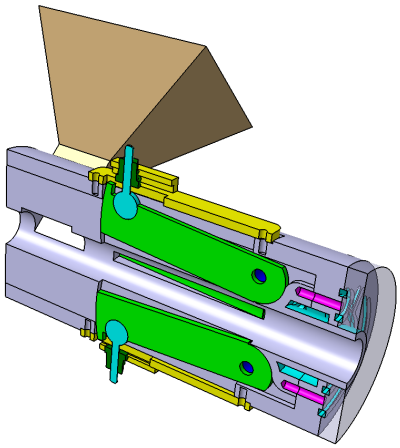

Fig. 23. Modified concept model No 3 in an open position (with grooves)

The main construction elements of the presented adjustable grooved section are presented in Figures 24, 25, 26, 27 and 28.

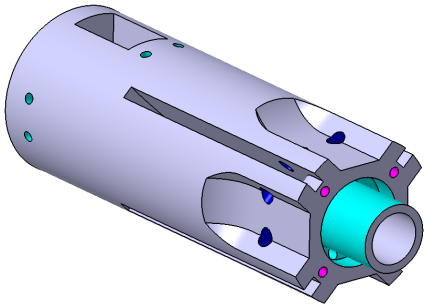

Fig. 24. Modified concept model No 3 – main sleeve

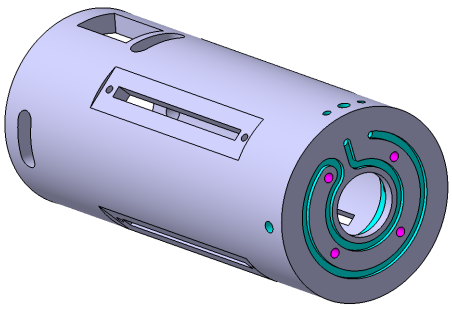

Fig. 25. Modified concept model No 3 - barrel

In Figures 24 – 26 the surfaces in contact with the cooling agent are visualised in a blue colour. For constructional reasons, the shape of the cooling groove was changed. In this concept, the input and output openings for the cooling agent are placed on the side surface of the sleeve.

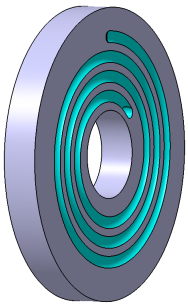

Fig. 26. Modified concept model No 3 – separating cooling disc

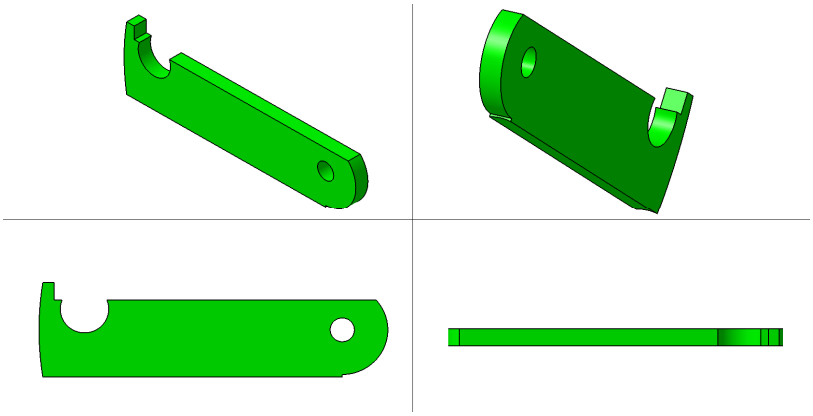

Fig. 27. Modified concept model No 3 –moving segment

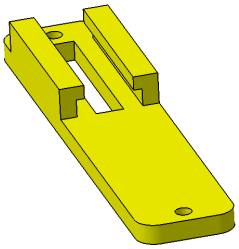

Fig. 28. Modified concept model No 3 – fixing element

1.4. Concept No 4

In Figure 29 an axonometric view of concept model No 4 is presented, the particular elements are also visualised in the exploded view (Figure 30).

Similarly as in model No 1 and No 3, an adjustable grooved feed section is achieved by rotating the moving segments 3. This rotation is forced by the sliding motion of the adjusting element with a group of wedges. The sliding motion of this element is forced by a special nut 8, which is appropriately fixed in the barrel. It is possible to obtain the sliding motion in another way, too (e.g. using a hydraulic or pneumatic cylinder).

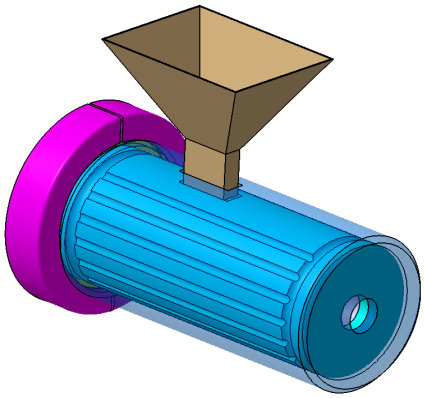

Fig. 29. Concept model No 4. Assembly view

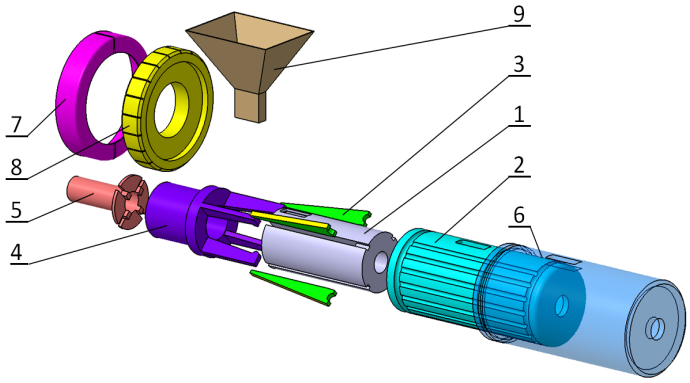

Fig. 30. Concept model No 4. Exploded view: 1 – main sleeve, 2 – cooling barrel, 3 – moving segment, 4 –adjusting element with a group of wedges, 5 – sleeve with a closing disc, 6 – external sleeve, 7 – circular protective element, 8 – special nut, 9 – hopper

The closing (smooth surface) and opening (grooved surface) of the grooved section is achieved by rotating segments around cylindrical elements formed in the

main sleeve. In Figures 31 and 32 the visualisation of segment placements in their extreme positions is presented – closed (without grooves) and open (with grooves).

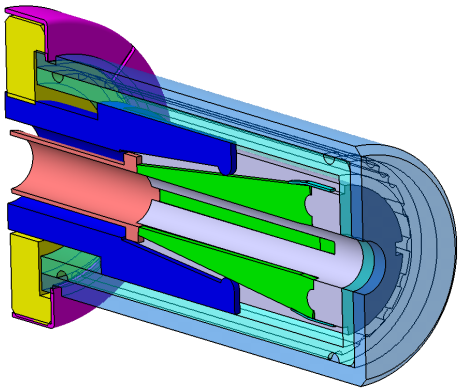

Fig. 31. Concept model No 4 in the closed position (without grooves)

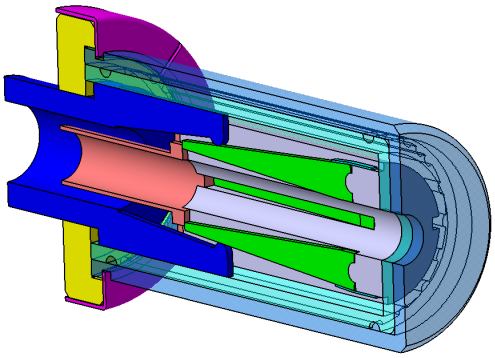

Fig. 32. Concept model No 4 in the open position (with grooves)

Main construction elements of the presented adjustable grooved feed section are shown in Figures 33, 34, 36 and 37.

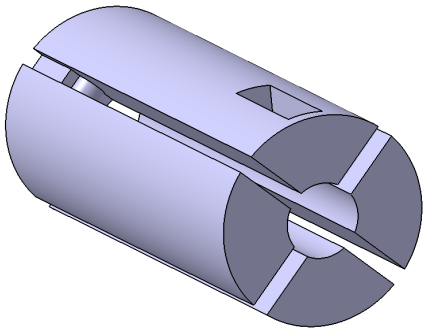

Fig. 33. Concept model No 4 – main sleeve

The main sleeve provides the appropriate direction of movement for moving segments. In the cuts in the main sleeve, cylindrical elements were made, to provide axis for the rotation of segments From the other side, the space, in which the moving segments rotate, is closed by a sleeve with a closing disc 5.

A very important element of the presented adjustable grooved feed section is the adjusting element with a group of wedges (Fig. 34). The rotation to the right, of the special nut 8 with a fine thread, protected against axial movement by means of protective elements 7, induces a sliding motion of the adjusting element with a group of wedges 4. On its cylindrical part, a fine thread was cut of identical parameters as the special nut, while grooves in the main sleeve 1, by blocking the rotational movement of this element, force its axial movement.

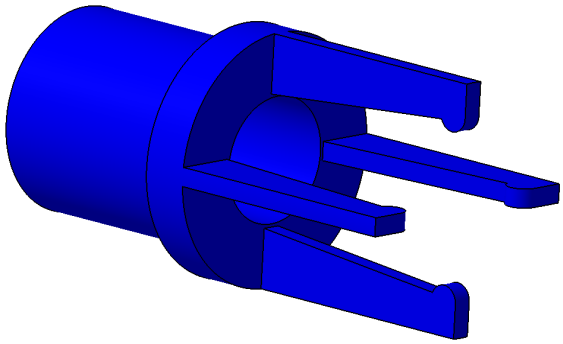

Fig. 34. Concept model No 4 – adjusting element with a group of wedges

Cylindrical tips in the adjusting element 4, during the sliding motion towards the front, press on the moving segments 3, which are put into the rotational movement, closing the space of grooves (section without grooves). Analogically, the rotation of the nut to the left, will induce the opening of the grooved section (the creation of grooves). This effect is encouraged by flat elastic elements, mounted on the upper

surface of the segment and in the cavity, in which they are fixed. These springs can be seen in Figures 31 and 32 and in enlargement in Fig. 35.

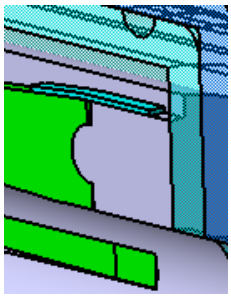

Fig. 35. Concept model No 4 – flat spring

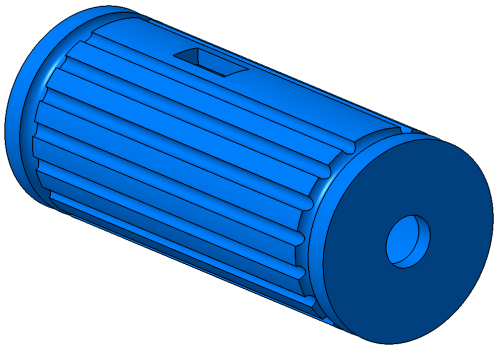

Fig. 36. Concept model No 4 – cooling sleeve

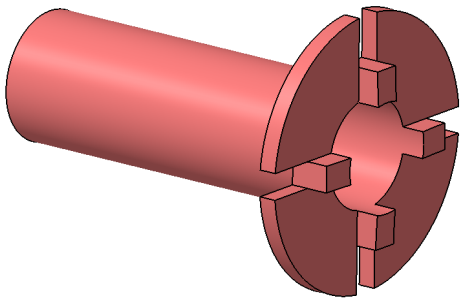

Fig. 37. Concept model No 4 – sleeve with a closing disc

1.5. Concept No 5

In Figure 38 an axonometric view of concept model No 5 is presented, the particular elements are also visualised in the exploded view Fig. 39 The idea of this concept consists in using circular rotational segments with grooves of different shape (Fig. 40). The first from the circular segments (from the side of the hopper) is mounted in the main sleeve, the others can move to the right or to the left within a certain, limited range of the angle of rotation. The appropriate rotation of these segments can influence the geometry of the grooves, that is longitudinal grooves can become helical, right-handed or left-handed (Fig. 41).

a) b)

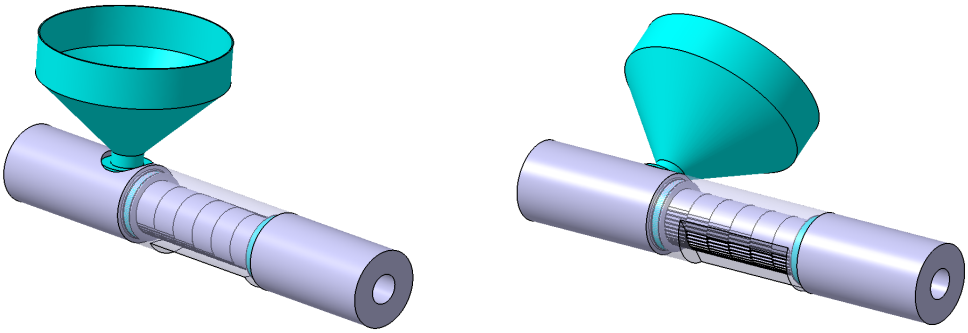

Fig. 38. Concept model No 5. Assembly view: a) axonometric view, b) axonometric view showing the geometry of the outer surface of the rotational segments and the way of adjusting the segments

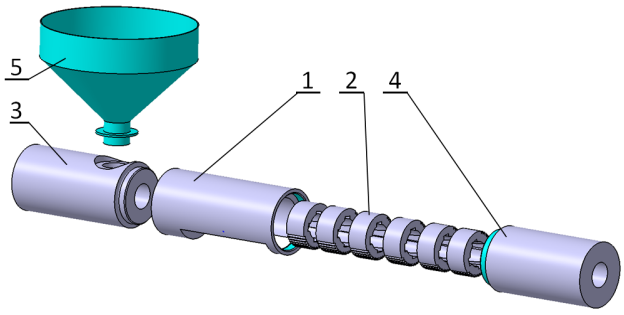

Fig. 39. Concept model No 5. Exploded view: 1 – barrel, 2 – circular grooved segment, 3 – input sleeve, 4 – output sleeve, 5 – hopper

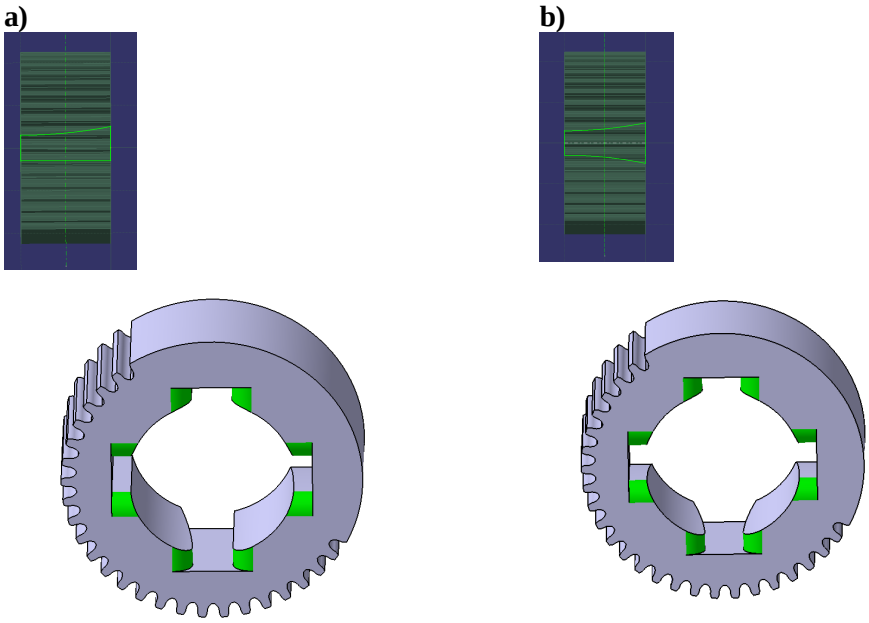

Fig. 40. Concept model No 5. Circular grooved segment: a) outline of the groove one-sidedly curvilinear, b) outline of the groove mutually curvilinear

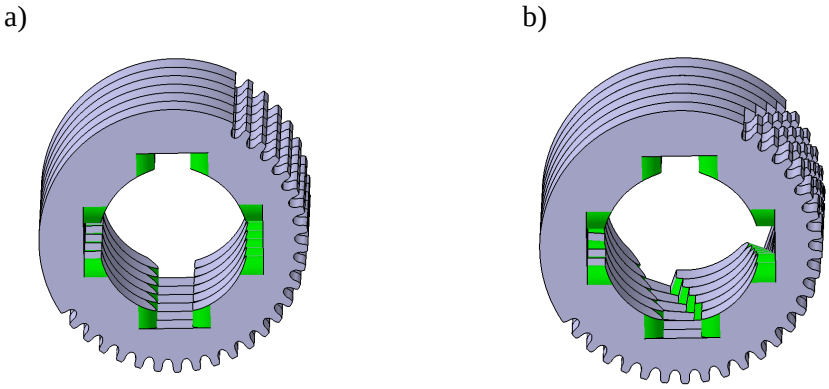

Fig. 41. Concept model No 5. A group of circular grooved segments of one-sidedly curvilinear outline: a) relative angle of rotation 0°, b) relative angle of rotation 5° to the left (left-handed grooves)

1.6. Concept No 6

In the presented concept, the sliding motion of moving segments is in the radial direction. However, it is forced, similarly as in concept No 4, by the axial movement of the threaded sleeve with four wedges. It is possible to develop such constructional solutions, in which the movement of segments will be forced in another way e.g. gear with a stepper motor, straight adjusting screw as in concept No 3. An effective grooved section appears or disappears along the width of the groove simultaneously. In Figure 42 an axonometric view of concept model No 6 is presented, the particular elements are also visualised in the exploded view Fig. 43.

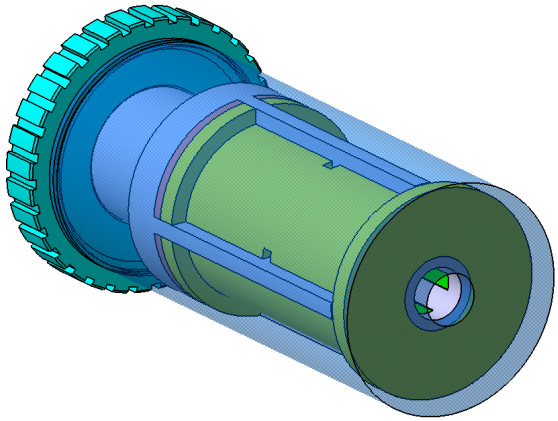

Fig. 42. Concept model No 6. Assembly view

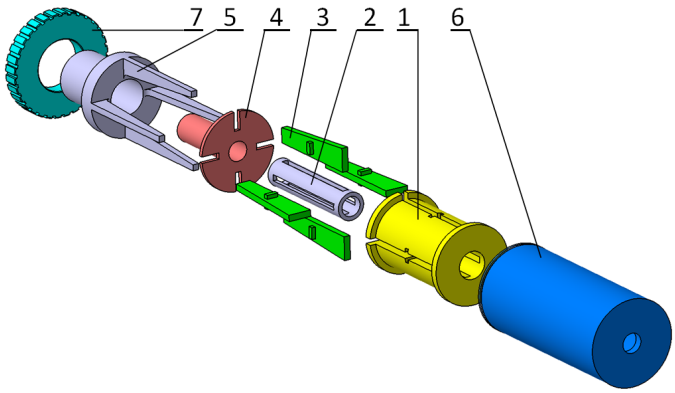

Fig. 43. Concept model No 6. Exploded view: 1 – main sleeve, 2 – guide sleeve, 3 – segment with a wedge surface, 4 – sleeve with a closing disc, 5 – adjusting element with a group of wedges, 6 – body, 7 – nut

Grooves in the grooved feed section are achieved by a sliding motion of segments with a wedge surface 3 in the radial direction. This motion is forced by an adjusting element with a group of wedges 5, which has the possibility of axial movement without the possibility of rotation. In Figures 44 and 45, the visualisation of the palcement of segments is presented in the extreme positions – closed (without grooves) and open (with grooves).

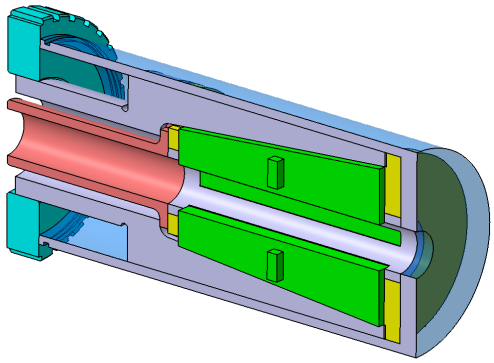

Fig. 44. Concept model No 6 in the closed position (without grooves)

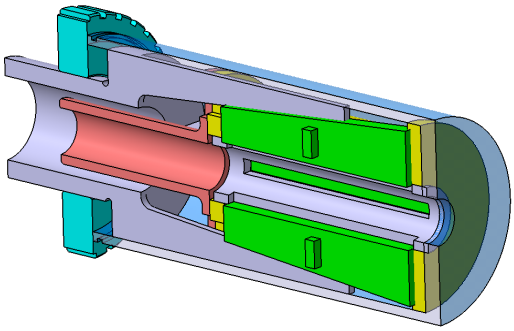

Fig. 45. Concept model No 6 in the open position (with grooves)

The main elements of this adjustable grooved section are presented in Figures 46, 47, 48, 49 and 50.

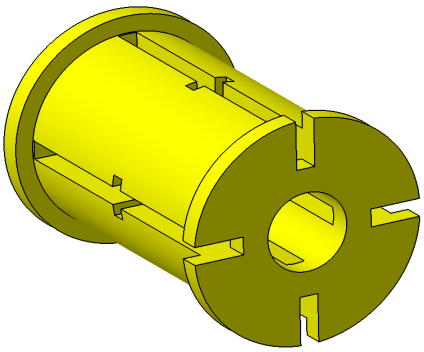

Fig. 46. Concept model No 6 – main sleeve

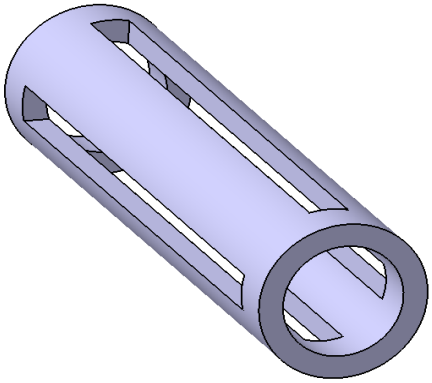

Fig. 47. Concept model No 6 – guide sleeve

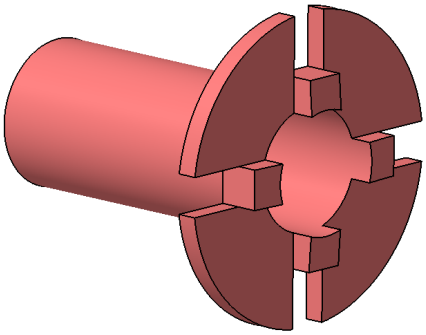

Fig. 48. Concept model No 6 – closing sleeve

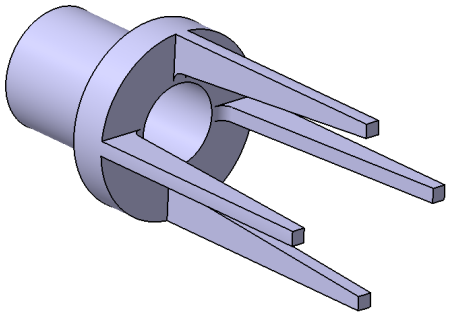

Fig. 49. Concept model No 6 – adjusting element with a group of wedges

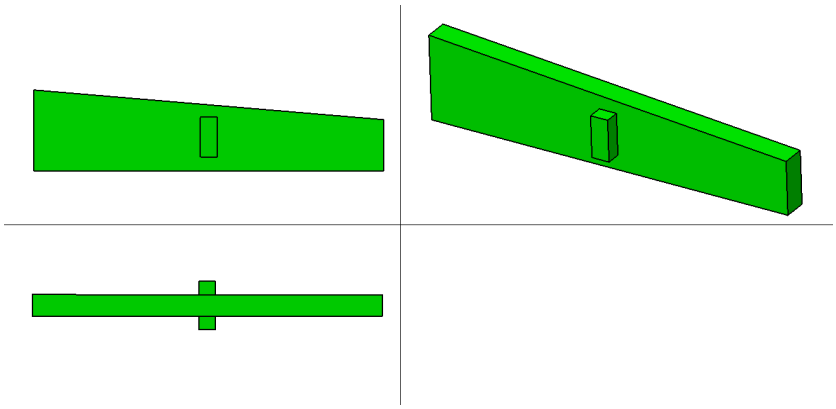

Fig. 50. Concept model No 6 - segment with a wedge surface

1.7. Concept No 7

The most important characteristic of this solution is the possibility to change the length of the grooves while maintaining their other geometrical features. The main element of the presented grooved section is an appropriately shaped sleeve with grooves and openings, through which goes a specially shaped and well fitted element with a group of inlets. It is put into motion by two pneumatic or hydraulic cylinders. The axonometric view of this grooved section is shown in assembly Figure 51, while in Figure 52 an exploded view is shown.

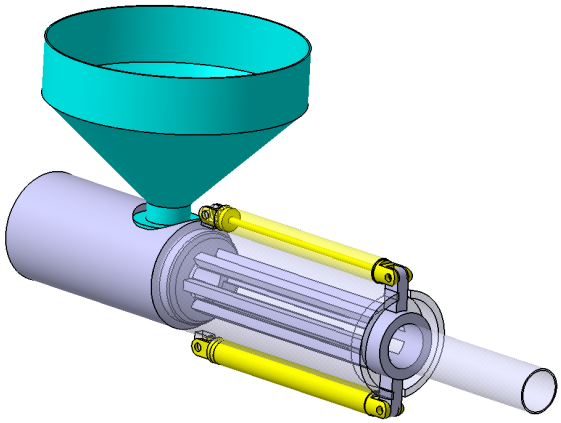

Fig. 51. Concept model No 7. Assembly view

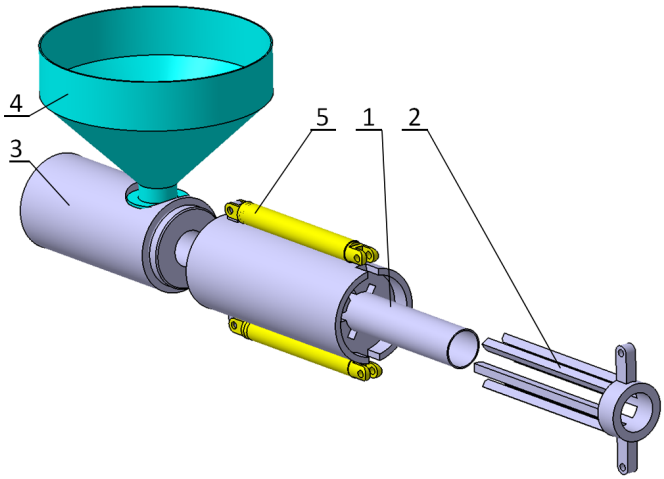

Fig. 52. Concept model No 7. Exploded view: 1 – main sleeve, 2 – closing element with a group of inlets, 3 – initial sleeve, 4 – polymer hopper, 5 – cylinder

In Figure 53, an adjustable grooved section with the longest grooves is shown (open position), while in Figure 51 the same section is shown, but without grooves – in the closed position.

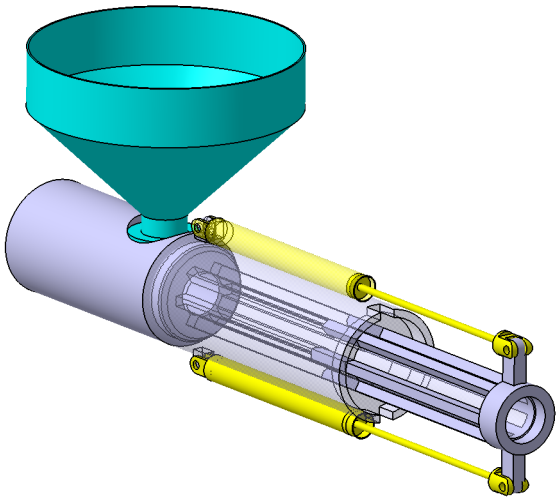

Fig. 53. Concept model No 7. Grooved section with the longest grooves

The main construction elements of this section are presented in Figures from 54 to 56.

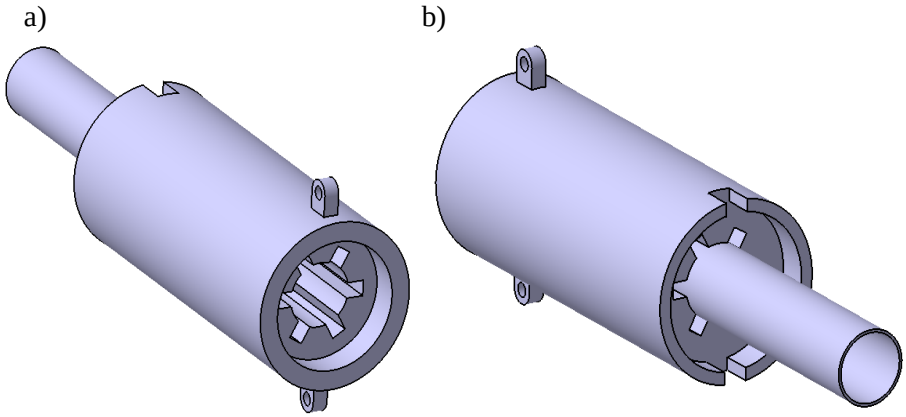

Fig. 54. Concept model No 7 – main sleeve: a) axonometric view from the side of the extruder head, b) axonometric view from the side of the hopper

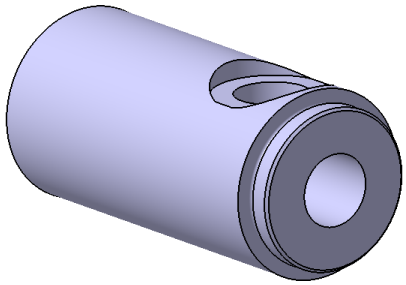

Fig. 55. Concept model No 7 – initial sleeve

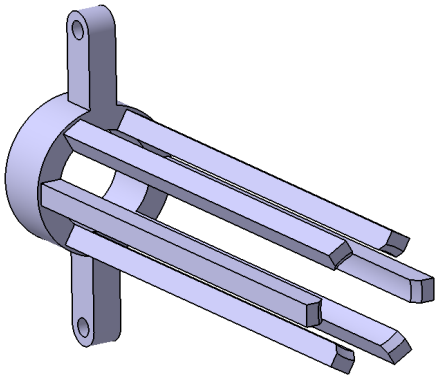

Fig. 56. Concept model No 7 – closing element with a group of inlets

1.8. Concept No 8

The concept of this adjustable grooved section is similar to the one presented in the solution No 7, and the modification consists in avoiding the assembly problems because the pneumatic or hydraulic cylinders are mounted on the side of the hopper and not on the side of the extruder head. The sliding motion of the closing element takes place on the side of the hopper, which required different constructional solutions. The main construction element of this section is the appropriately shaped sleeve with grooves and openings, through which goes a specially shaped and well fitted element with a group of inlets. It is put into motion by two pneumatic or hydraulic cylinders. The axonometric view of this grooved section is shown in Figure 57, while in Figure 58 an exploded view is shown.

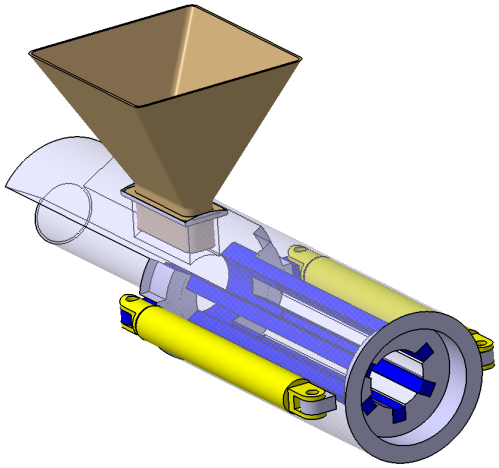

Fig. 57. Concept model No 8. Assembly view

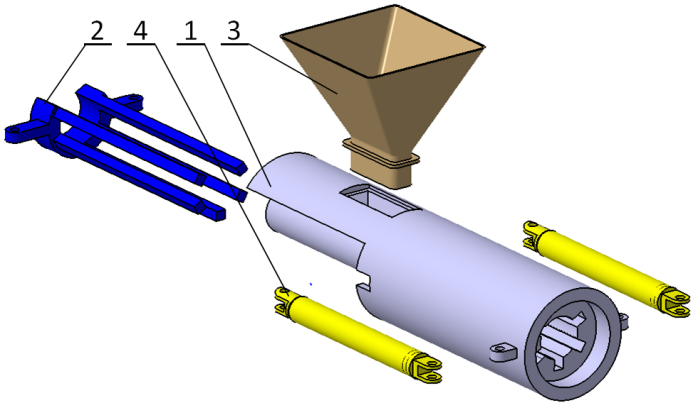

Fig. 58. Concept model No 8. Exploded view: 1 – main sleeve, 2 – closing element with a group of inlets, 3 – polymer hopper, 4 – pneumatic cylinder

In Figure 59 an adjustable grooved section is shown with the longest grooves (open position), while in Figure 57 the same section is shown but without grooves – in the closed position.

The main construction elements of the presented adjustable grooved section are presented in Figures 60 and 61.

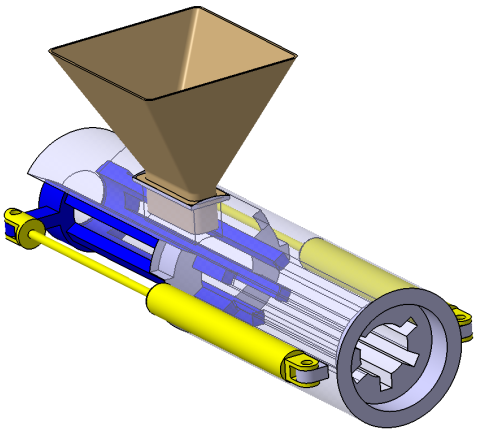

Fig. 59. Concept model No 8. Grooved section with the longest grooves (open position)

a) b)

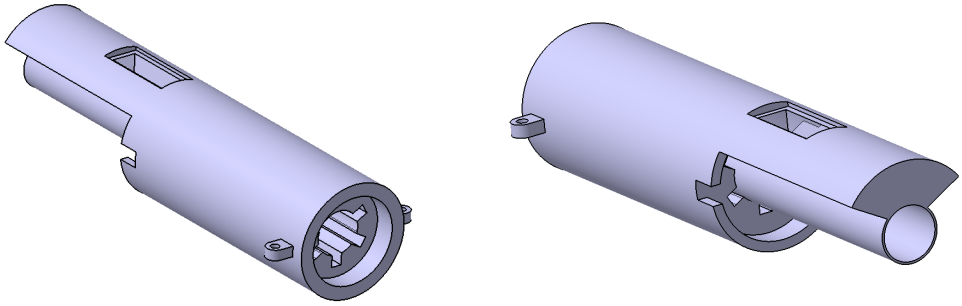

Fig. 60. Concept model No 8. Main sleeve: a) axonometric view from the side of the extruder head, b) axonometric view from the side of the hopper

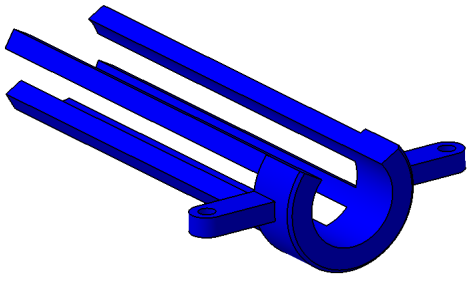

Fig. 61. Concept model No 8 – closing element with a group of inlets

1.9. Concept No 9

The concept of this adjustable grooved section is similar to the solution presented in concept No 8, and the modification consists in using an additional element with a group of inlets moved by additional pneumatic or hydraulic cylinders. The sliding-return motion of the closing element with a group of double inlets takes place on the side of the hopper, while the sliding-return motion of the additional element with a group of single inlets takes place in the opposite direction, on the side of the extruder head. Similarly as in other concepts, the main construction element of this section is an appropriately shaped sleeve with grooves and openings, through which goes into the space of grooves, a specially shaped and well fitted closing element with a group of double inlets, which is put into motion by two cylinders. The inlets have grooves, into which go single inlets of the additional element. This solution enables to change the width and length of the grooves.

The axonometric view of the adjustable grooved section is presented in Figure 62, while in Figure 63 the exploded view is shown.

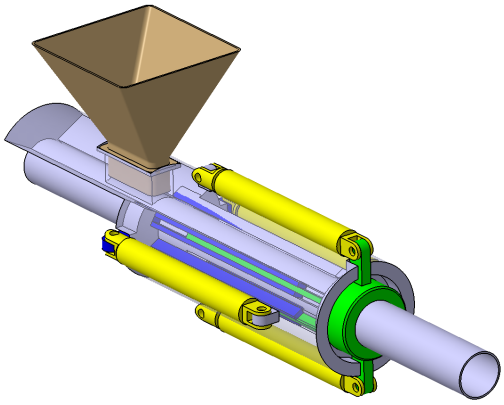

Fig. 62. Concept model No 9. Assembly view

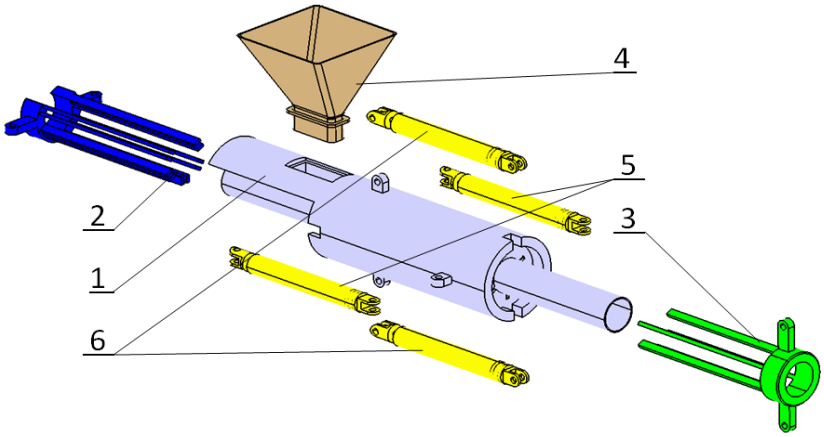

Fig. 63. Concept model No 9. Exploded view: 1 – main sleeve, 2 – closing element with a group of inlets, 3 – additional element with a group of inlets, 4 – polymer hopper, 5 – cylinder of the closing element, 6 – cylinder of the additional element

In Figure 64 the adjustable grooved section is shown with the longest and widest grooves (open position), while in Figure 65 the grooved section with the longest but the narrowest grooves is presented. In Figure 66 the discussed section is shown in the partially open position, when the space of the groove is divided by a narrow inlet into two halves. In Figure 67 the same section but without grooves is shown - in the totally closed position.

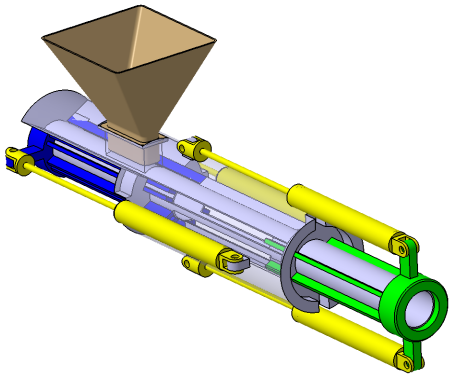

Fig. 64. Concept model No 9. Adjustable section with the longest and widest grooves (totally open position)

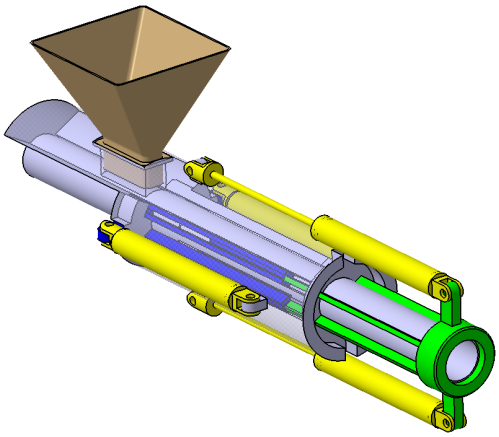

Fig. 65. Concept model No 9. Adjustable section with the longest and narrowest grooves (partially open position)

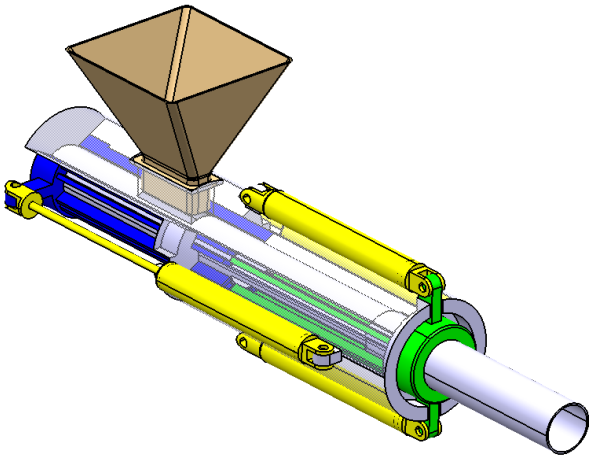

Fig. 66. Concept model No 9. Adjustable section with double grooves (partially open position)

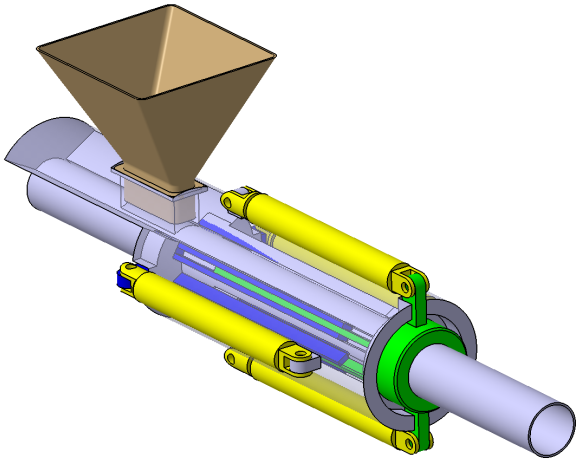

Fig. 67. Concept model No 9. Adjustable section totally closed

The main elements of the discussed adjustable grooved section are presented in Figures 68 and 69. The main sleeve, with appropriately made grooves, is the most important, key part of this section. The grooves are not distributed evenly because of the necessity to mount the polymer hopper. The width of the grooves is 9 mm and their depth is 6 mm. Two thin-walled pipes are tightly fitted into the sleeve and they are simultaneously guideways for the closing elements. The above mentioned thin-walled pipes close constructionally the space around the screw. There remain only the longitudinal notches, in which closing elements move: the main and the additional one. Depending on the position of the cylinders, the space of the grooves can have the width of: 0 mm (Figure 67), 3 mm (Figure 65), 2 x 3 = 6 mm (Figure 66), 3 x 3 = 9 mm (Figure 64). In the case of a double groove 2 x 3 mm, the groove of the width 9 mm is divided by the inlet of the width 3 mm. Then two grooves of 3 mm each appear.

a) b)

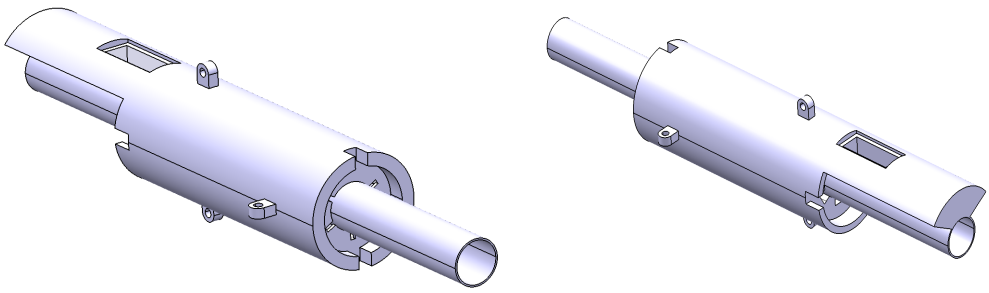

Fig. 68. Concept model No 9. Main sleeve: a) axonometric view from the side of the extruder head, b) axonometric view from the side of the hopper

In Figure 69 innovative closing elements are shown. The main closing element consists of the group of 5 double inlets placed in a circular order corresponding to the grooves made in the main sleeve. An auxiliary closing element consists of a group of single narrow inlets placed in a circular order.

a) b)

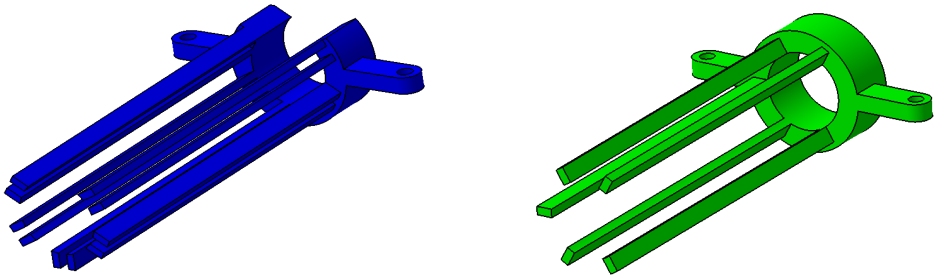

Fig. 69. Concept model No 9: a) closing element with a group of double inlets, b) additional element with a group of single inlets

1.10. Concept No 10

The concept of this adjustable grooved feed section is similar to the solution presented in Concept No 7, however, helical grooves are used in the main sleeve. The element which closes the space of the groove is the innovative closing element whose shape resembles a thin-walled, empty bolt of the rectangular outline of the "thread". It has multiple flights characterised by a small angle of pitch. This element has a flange of the properties of the plain bearing (longitudinal, rolling ball bearing can also be used) in which a double clamp is fixed. Thanks to these properties, the

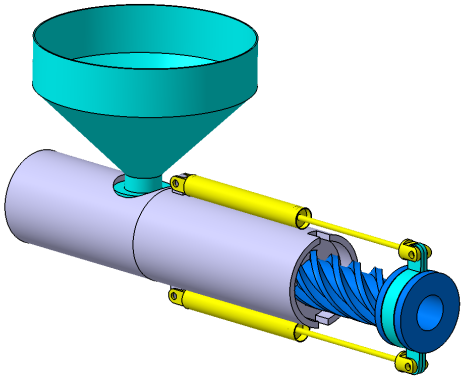

Fig. 70. Concept model No 10. Assembly view

sliding motion of pneumatic or hydraulic cylinders can put the additional closing element into the rotational movement, totally or partially closing the grooved space.

The axonometric view of the presented grooved feed section is shown in Figure 70, while in Figure 71 an exploded view is shown.

In Figure 70 the presented adjustable grooved feed section is shown with the longest helical grooves (open position), while in Figure 72 this section is shown, but without grooves – in the closed position.

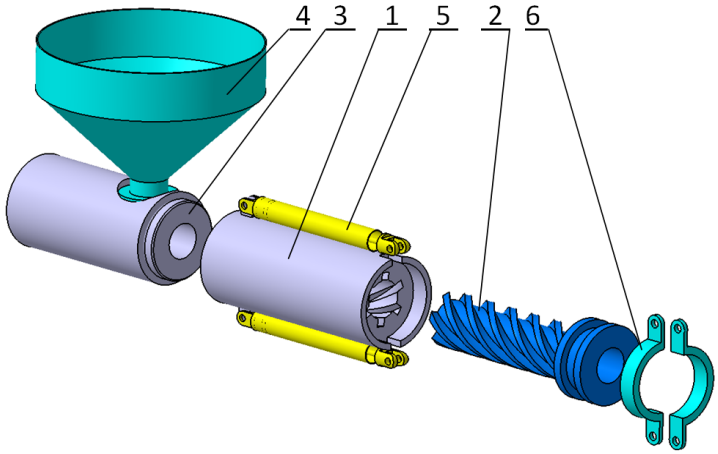

Fig. 71. Concept model No 10. Exploded view: 1 – main sleeve, 2 – helical closing element, 3 – initial sleeve, 4 – polymer hopper, 5 – cylinder, 6 – clamp

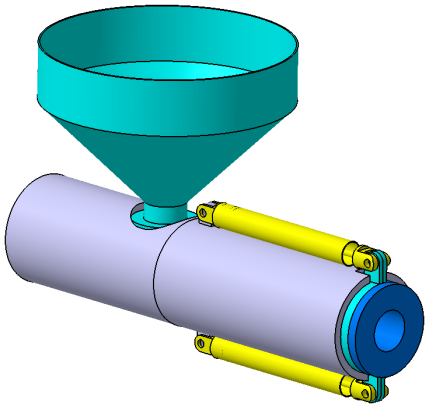

Fig. 72. Concept model No 10. The grooved section in the closed position (without grooves)

The main construction elements of the presented adjustable grooved feed section are presented in Figure 73 and Figure 74.

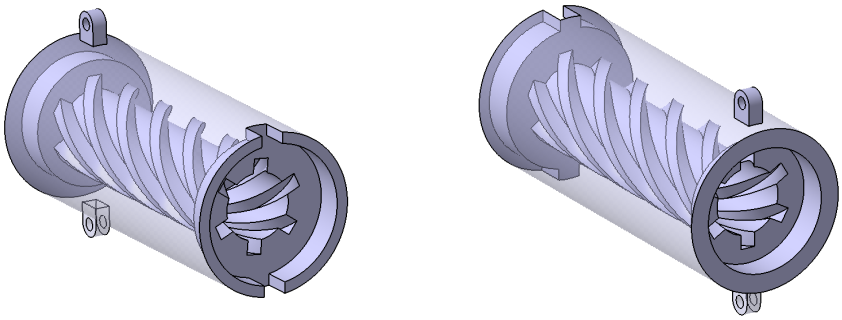

Fig. 73. Concept model No 10. Main sleeve (for better visualisation, the outer cylindrical surface is transparent)

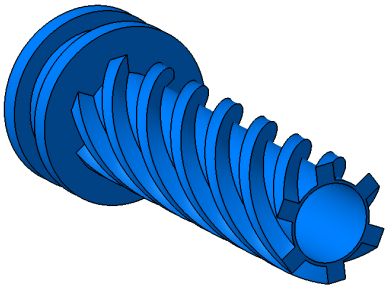

Fig. 74. Concept model No 10. Helical closing element

2. Conclusion

All presented construction models of the active grooved zone are new and are protected by intellectual property rights. After analyzing the possibilities of their production, it was decided to choose three models for which heat and strength computational computer simulation was performed using the ABAQUS program.

Mirosław Ferdynus[1], Janusz W. Sikora[2], Alžbeta Perháčová[3]

NEW CONCEPTS OF A ACTIVE GROVVED FEED SECTION FOR A NEW GENERATION EXTRUDER – THERMAL AND STRENGTH ANALYSIS

Abstract: *Numerical calculations were carried out aiming at strength and heat analysis of selected models. Numerical calculations were conducted using the method of finished elements. As a calculating tool ABAQUS® program was used. The AGFS was loaded with the torque, the pressure, the torgue and the pressure, as well as with the temperature. Calculations have shown that the proposed active grooved feed section designs are correct, under load they operate in a safe range of stresses, and their operation at a higher temperature is stable.*
Keywords: *extruder, grooved feed section, MES, thermal and strength analysis.*

1. Aim and range of numerical calculations

The aim of the conducted numerical calculations was to analyse the strength of the new construction of the adjustable grooved feed section of a single-screw extruder. Three constructional solutions were analysed. The numerical simulation was made on the basis of assembling of the construction elements made in CATIA V5 programme, a method of finished elements ABAQUS® implemented to the programme. Geometrical models accepted for numerical calculations of the analysed constructions are presented in Figures from 1 to 3.

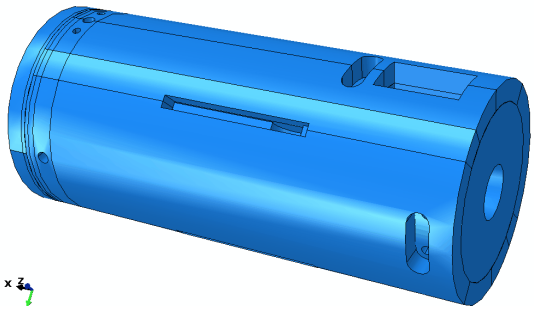

Fig. 1. Model of the adjustable grooved section-option 1(concept no 3, Fig. 20, part I)

[1] *Lublin University of Technology, Faculty of Mechanical Engineering, Department of Machine Design and Mechatronicsg, ul. Nadbystrzycka 36, 20-618 Lublin, Poland, m.ferdynus@pollub.pl*
[2] *Lublin University of Technology, Faculty of Mechanical Engineering, Department of Technology and Polymer Processing, ul. Nadbystrzycka 36, 20-618 Lublin, Poland, janusz.sikora@pollub.pl*
[3] *SEZ KROMPACHY a.s., Hornádska 585/1, 053 42 Krompachy, Slovakia, betka.perhacova@sez-krompachy.sk*

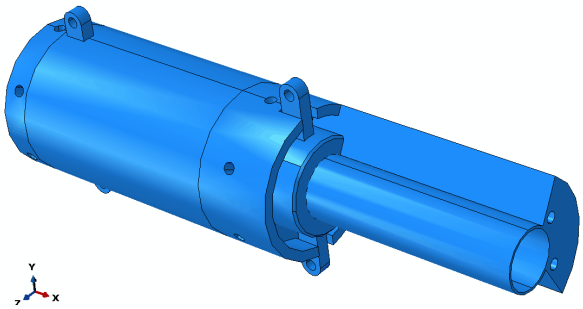

Fig. 2. Model of the adjustable grooved feed section - option 2 (concept no 8 – Fig. 39, part I)

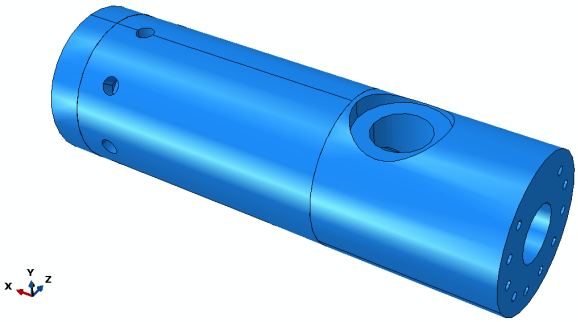

Fig. 2. Model of the adjustable grooved feed section – option 3 (concept no 5 – Fig. 57, part I)

The range of the conducted numerical analyses included calculations concerning the estimation of the strength of construction elements exposed to the pressure caused by the transfer of polymer in the form of pellets as well as thermal calculations enabling to receive the temperature distribution as a result of friction of the material against the inner walls of the grooved section. Within the numerical calculations, the following tasks were carried out:

- developing discrete models enabling the numerical analysis using the method of finished elements,
- determining material models and limiting cases of loading the construction,
- conducting numerical simulations enabling to determine the distribution of reduced stress and nodal displacement of construction,
- evaluation of stiffness and strength of construction on the basis of the received results of numerical analysis,
- estimation of temperature distribution in the elements of construction during the exploitation of the grooved section,

- conclusions of the conducted numerical analysis, presenting the evaluation of the proposed constructional solutions.

1.1. Discretization of construction

Numerical calculations were conducted using the method of finished elements. As a calculating tool ABAQUS® programme was used. The construction of discrete models was made on the basis of the developed geometrical models of analysed constructions. In all variants concerning the strength calculations, the discretization of a geometrical model was made using tetragonal solid elements, type C3D10, which constitute 10-nodal elements with the shape function of the second order and full integration as well as solid elements of hexagonal type marked C3D8R, which constitute 8-nodal elements with the shape function of the second order and reduced integration. Additionally, in thermal analysis, tetragonal elements, type C3D10MT and hexagonal elements type C3D20MT were used to enable to take into account in a numerical analysis a thermal degree of freedom. In all variants it was accepted that elements of construction are made of steel marked 40HM.

In strength calculations, a bilinear model of material was accepted, of elastic-plastic characteristics, for which the following material properties were accepted (table 1).

In thermal calculations, a bilinear model of material was accepted, of elastic-plastic characteristics, for which the following thermal properties were accepted (table 2).

In order to imitate the cooperation of joint elements of the model, interactions of type *Tie* were defined - they ensure a constant connection of elements through joining all degrees of freedom on contacting surfaces of construction elements.

In this way it was possible to model the possibility of constant transfer of loads and displacements between the joint construction elements.

Table 1. Mechanical properties of steel 40HM

Material properties – steel 40HM	
Young modulus E [Pa]	$2.1 \cdot 10^{11}$
Poisson number [-]	0.3
Yield strength R_e [Pa]	$8.8 \cdot 10^{+11}$
Strength limit R_m [Pa]	$1.03 \cdot 10^{12}$
Elongation at break [%]	10

Table 2. Material properties for thermal calculations

Material properties – steel 40HM	
Density ρ [kg/m^3]	7860
Linear expansion coefficient [1/K]	$1.2 \cdot 10^{-5}$
Heat conduction coefficient λ [W/(m·K)]	58
Specific heat [J/(kg·K)	450

In the case of cooperation of construction elements consisting in taking into account mutual mechanical and thermal influences, contact interactions were used, which enable to model mechanical influence at the normal and tangential direction of the cooperating elements of the model as well as take into account the possibility of heat transfer on the surfaces of cooperation.

1.2. Boundary conditions and loading of construction

The definition of boundary conditions in particular numerical models was carried out by fixing nodes placed in the specified surfaces of the model (depending on the construction variant), blocking the possibility of their displacement (translational degrees of freedom of nodes placed on these surfaces) in three directions X, Y and Z. Exemplary boundary conditions with marked fixing surfaces, defined in the openings of mounting holders, for variant 2 are presented in Fig. 4.

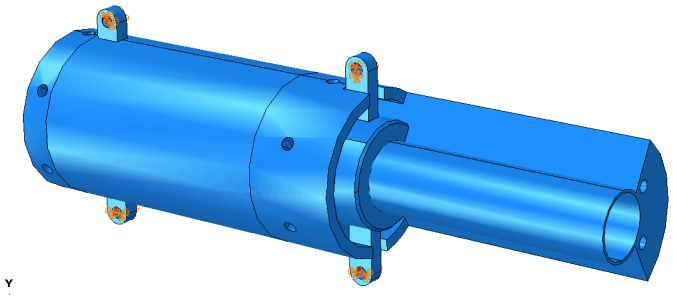

Fig. 4. Boundary conditions of the model – variant No 2

In particular numerical models, identical cases of loading concerning the mechanical and thermal analysis were defined. In strength analysis, the loading of the model was constituted by the pressure caused by the transfer of polymer pellets in the extruder screw. In this case, the exponential pressure distribution along the grooved section equalling L_R = 100 mm, whose maximum value (at the end of the section, counting from the feed opening zone) equalled p = 10 MPa. The scheme of

introducing pressure into the construction of the grooved section is presented in Figure 5.

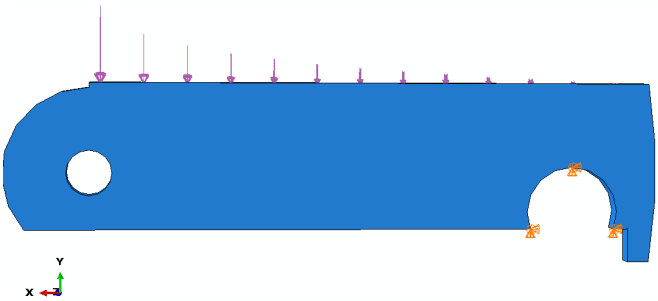

Fig. 5. Loading the grooved section with pressure of exponential distribution

In thermal analysis, loading was constituted by temperature produced by friction of polymer pellets transported by the screw. In all variants, temperature was applied to the surface of the grooved section in an analogical way as pressure, e.i. exponential distribution was accepted along the grooved section equalling L_R = 100 mm, whose maximum value (at the end of the section, counting from the feed opening zone) equalled T = 120°C. The initial temperature of the numerical model was accepted as T_0 = 22°C. The scheme of introducing temperature load into the construction of the grooved section is presented in Figure 6. Additionally, in particular models, systems of cooling with liquid of temperature T_c = 10°C were used. An example of loading the model with temperature of cooling liquid is presented in Fig. 7. In thermal calculations, it was accepted that the time of duration of numerical analysis was equivalent to the time of constant extruder operation equalling t = 18000 seconds.

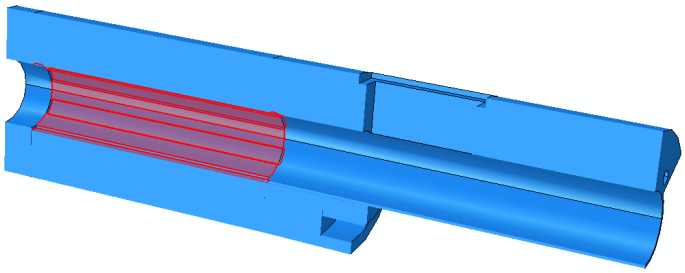

Fig. 6. Loading the grooved section with temperature

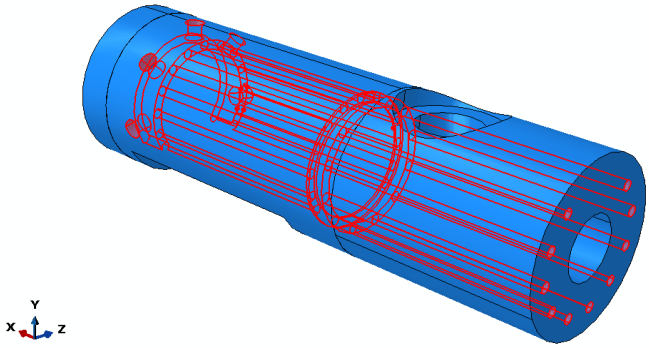

Fig. 7. Loading the cooling liquid with temperature on the example of variant 3

2. Results of numerical calculations

A numerical analysis of the construction of the extruder rotational section was conducted in the range of static calculations, taking into account a geometrically non-linear issue (big displacement and deflection). In order to solve a non-linear system of equations, Newton-Raphson increment-iterative method was used. A strength and stiffness analysis of particular construction elements was conducted on the basis of the distributions of reduced tension, determined in accordance with Huber-Mises-Hencky strength hypothysis in the area of analysed construction and displacement of nodes of its particular elements. The accepted hypothesis is the basic hypothysis used in engineering calculations in relation to elements made of materials of isotropic properties. In thermal calculations, the temperature distribution was determined in the area of analysed constructions, taking into account the cooling of the grooved feed section in the state corresponding to 18 000s (5 hours) of constant operation of the machine.

Distributions of tension, displacements and temperature are presented in the form of colourful contour maps against the background of the deflected model, in which the red colour indicates maximum values, while the blue colour minimum values.

2.1. Variant 1 of the construction of the grooved section

a) Strength calculations

A general view of the distribution of reduced tension against the deflected model is presented in Fig. 8 and Fig. 9. The presented values of tension are expressed in [Pa].

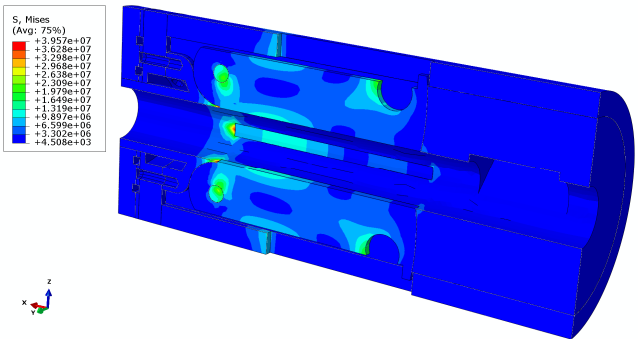

Fig. 8. Distribution of reduced tension H-M-H in elements of the grooved section

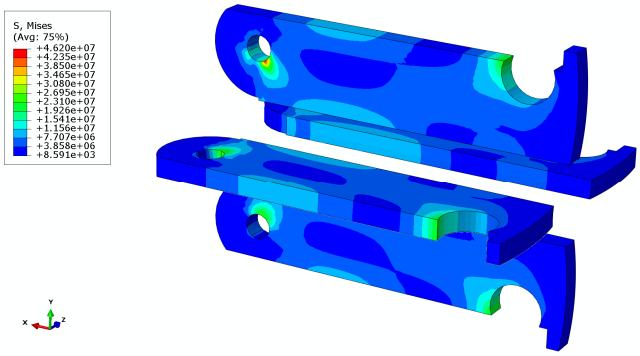

Fig. 9. Distribution of reduced tension H-M-H in the elements of construction under the highest tension

Maximum reduced tension in elements of variant 1 of the grooved section in case of mechanical load equals approximately $\sigma_z \approx 46$ MPa and appears in the material moving segments adjusting the depth of grooves. The value of the obtained tension is not bigger than the value of yield point, which in accordance with the accepted material properties for steel 40HM equals $R_e = 880$ MPa. It means that **the level of reduced tension appearing in the construction for the considered case of loading (loading with pressure of exponential distribution from the inside of the construction) does not threaten the safe operation of the construction.**

In Figure 10 the total displacement of nodes of the numerical model of the grooved feed section expressed in [m] are presented.

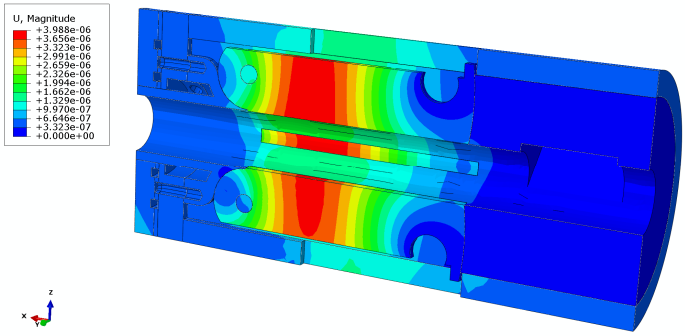

Fig. 10. Map of nodes displacement of the model

Analysing the values of nodes dispalcement, the maximum value of deflection was located in moving segments adjusting the depth of grooves, equalling 0.004 mm, which constitutes a very small value, not threatening the correct operation of the developed construction.

b) Thermal calculations

Figures from Fig. 11 to Fig. 12 present maps of temperature distribution in elements of variant 1 of the grooved feed section, corresponding to 5 hours of constant operation of the plasticizing system of the extruder. The presented values of temperature are expressed in [^{o}C].

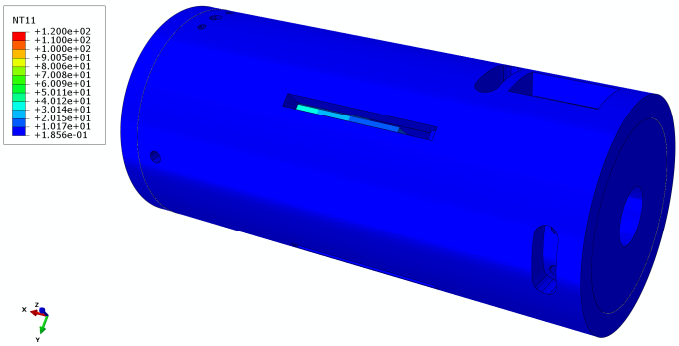

Fig. 11. Temperature distribution in the model of variant 1 of the grooved feed section from the external side

Analysing the obtained temperature distributions in the area of the grooved section it can be stated that the applied cooling system was designed in a correct way. It is confirmed by temperature maps in the material of the inner body (Fig. 13), directly exposed to the temperature action caused by the friction of pellets against

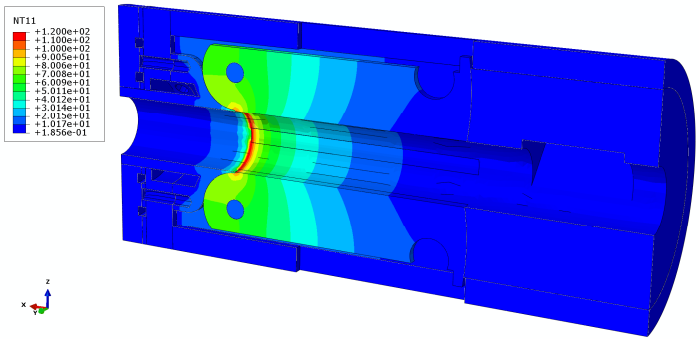

Fig. 12. Temperature distribution in the model of variant 1 of the grooved section from the internal side

the inner walls of the grooved section. The obtained temperature distribution shows that its high values equalling T = 120^{o}C persist only on the inner wall, while in almost whole area of the inner body the temperature level is low (blue colour) of values approx. T = 20 – 30^{0}C. The above temperature distribution in the area of the grooved section ensures a stable operation of the grooved section.

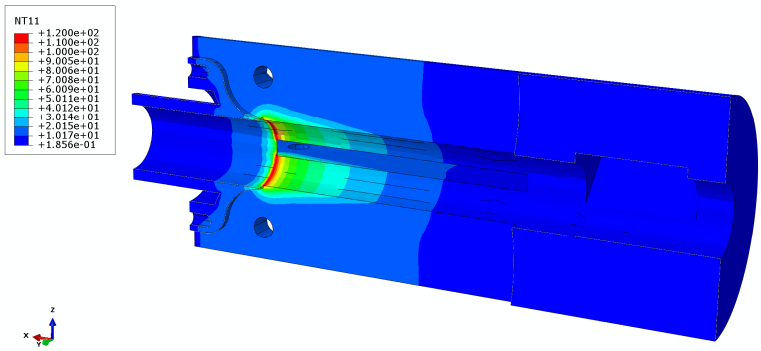

Fig. 13. Temperature distribution in the model of variant 1 of the grooved section – inner body

2.2. Variant 2 of the construction of the grooved section

a) Strength calculations

A general view of reduced tension against the background of the deflected model is presented in Fig. 14 and Fig. 15. The presented values of tension are expressed in [Pa].

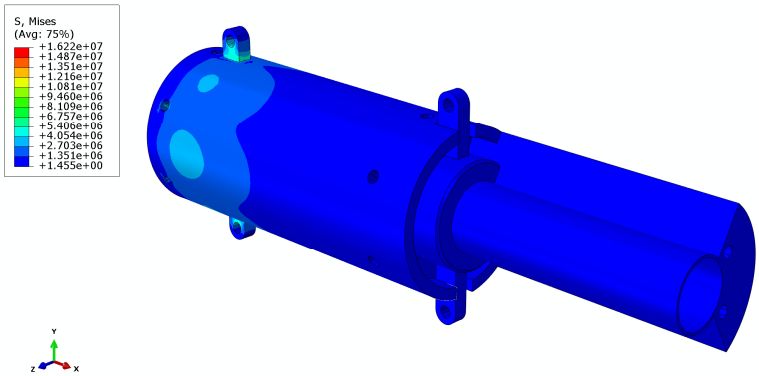

Fig. 14. Distribution of reduced tension H-M-H in the elements of the grooved section

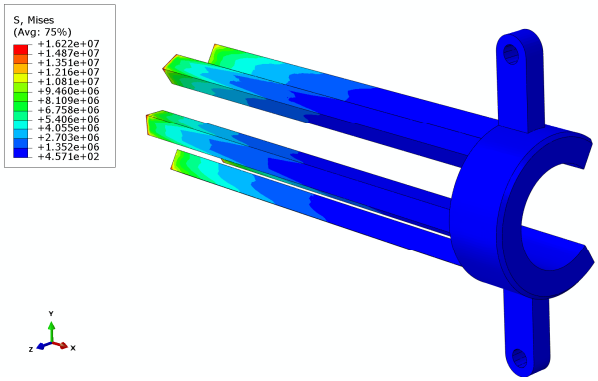

Fig. 15. Distribution of reduced tension H-M-H in the elements of construction under the highest tension

Maximum reduced tension in the elements of variant 2 of the grooved section in the case of mechanical load equal approximately $\sigma_z \approx 16$ MPa and appear in the material of the elements which adjust the length of the grooves. The value of the received tension does not exceed the yield point, which, according to accepted material properties for steel 40HM equals $R_e = 880$ MPa. It means that **the level of reduced tension appearing in the construction for the considered case of load (loading with pressure of exponential distribution from the inside of the construction) does not threaten a safe operation of the construction.**

Figure 16 presents total displacement of nodes of the numerical model closing element with a group of inlets expressed in [m].

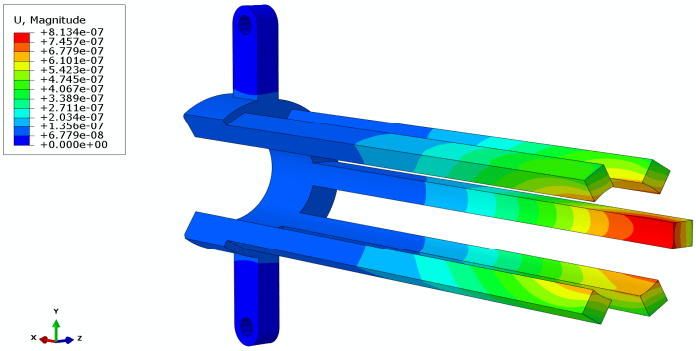

Fig. 16. Map of nodes displacements of the model

Analysing the values of nodes displacement, the maximum values of deflection were located in inlets which adjust the length of grooves. It equals 0.0008 mm, which constitutes a very small value, not threatening the correct operation of the construction.

b) Thermal calculations

Figure 17 and Figure 18 present maps of temperature distribution in the elements of variant 2 of the grooved section, corresponding to 5 hours of constant operation of the plasticizing system of the extruder. The presented temperature values are expressed in [^{o}C].

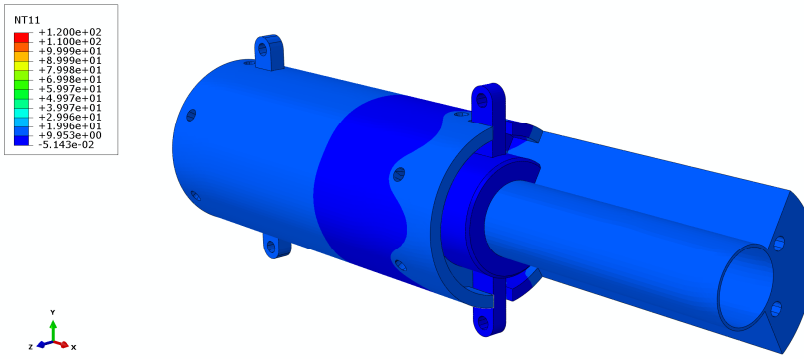

Fig. 17. Temperature distribution in the model of variant 2 of the grooved section from the external side

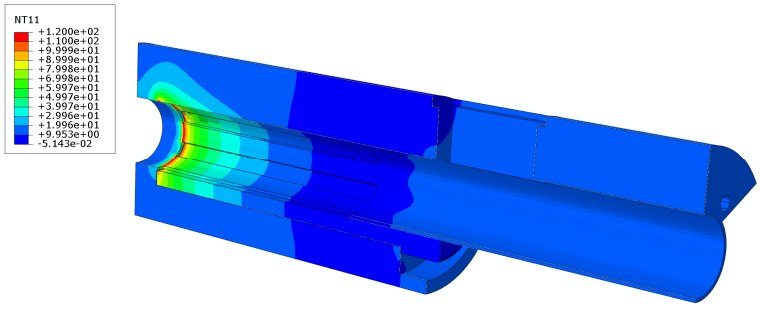

Fig. 18. Temperature distribution in the model of variant 2 of the grooved section from the internal side

Analysing the obtained temperature distributions in the area of the grooved section it can be stated that the applied cooling system was designed in a correct way. This is confirmed by temperature maps in the material of the inner body (Fig. 18), directly exposed to the temperature action caused by the friction of pellets against the inner walls of the grooved section. The received temperature distribution shows that its high values equalling T = 120^{o}C persist only on the inner wall, while almost in the whole area of the inner body the level of temperature is low (light blue and light green colour) of values approximately T = 20 – 40^{o}C. The above temperature distribution in the area of the grooved section ensures a stable operation of the grooved section.

2.3. Variant 3 of the construction of the grooved section

a) Strength calculations

A general view of the distribution of the reduced tension against the background of the deflected model is presented in Figure 19. The presented values of tension are expressed in [Pa].

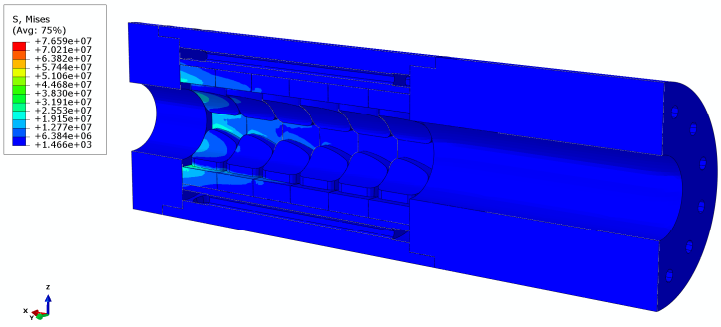

Fig. 19. Distribution of reduced tension H-M-H in the elements of the grooved section

Maximum reduced tension in the elements of variant No 3 of the grooved section in the case of mechanical load equal approximately $\sigma_z \approx 76$ MPa and appear in the material of circular grooved elements. The value of the received tension does not exceed the value of the yield point, which, according to the accepted material properties for steel 40HM equals $R_e = 880$ MPa. It means that the level of reduced tension appearing in the construction for the considered case of loading (loading with pressure of exponential distribution from the inside of the construction) does not threaten a safe operation of the developed construction of the grooved section.

Figure 20 presents the total displacement of nodes of the numerical model in circular grooved elements expressed in [m].

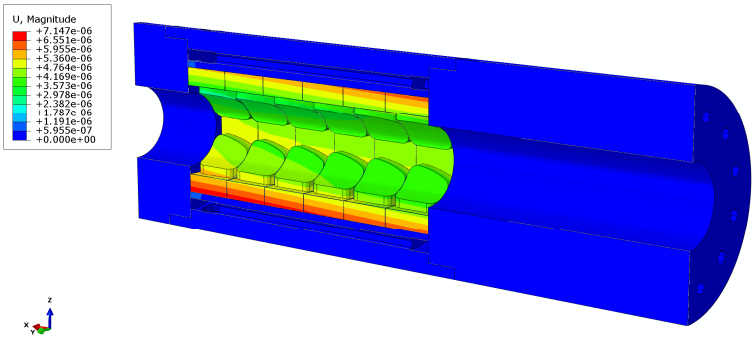

Fig. 20. Map of nodes displacement of the model

Analysing the values of nodes displacement, the maximum value of deflection was located in circular grooved elements which adjust the torsional angle of grooves. It equals 0.007 mm, which is a very small value, not threatening the correct operation of the construction of the grooved section.

b) Thermal calculations

Figure 21 and Figure 22 present maps of temperature distribution in the elements of variant No 3 of the grooved section, corresponding to 5 hours of continuous work of the plasticized system. The presented temperature values are expressed in [^{o}C].

Analysing the obtained temperature distributions in the area of the grooved section it can be stated that the applied cooling system was designed in a correct way. This is confirmed by temperature maps in the material of the inner circular elements (Fig. 22), directly exposed to the temperature action caused by the friction of pellets against the inner walls of the grooved section. The received temperature distribution shows that its high values equalling T = 120^{o}C persist only on the inner wall, while almost in the whole area of the inner body the level of temperature is low (light blue and light green colour) of values approximately T = 20 – 60^{o}C. The above temperature distribution in the area of the grooved section ensures a stable operation of the grooved section.

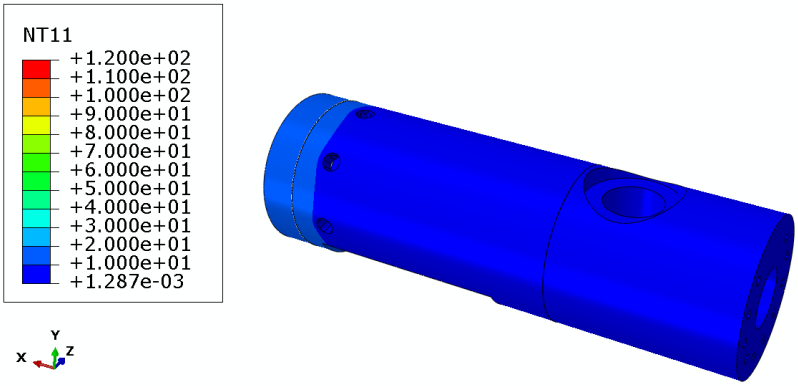

Fig. 21. Temperature distribution in the model of variant 3 of the grooved section from the external side

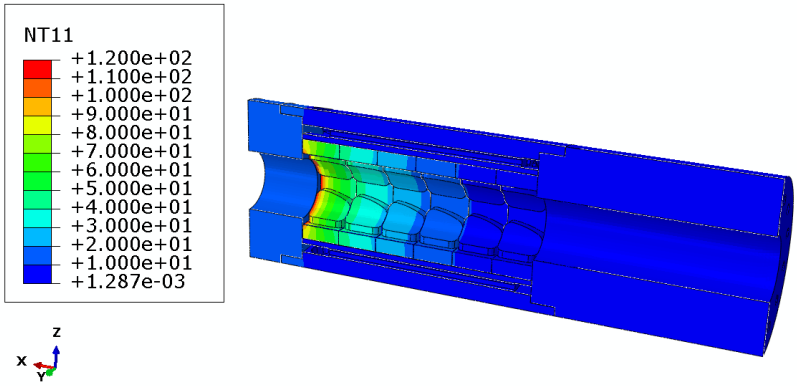

Fig. 22. Temperature distribution in the model of variant 3 of the grooved section from the internal side

3. Conclusions

The conducted numerical analysis using the method of finished elements allows to formulate conclusions concerning the strength and thermal evaluation of the analysed variants of the extruder grooved section. On the basis of the received results of numerical calculations it was stated that for all analysed cases of loading, the designed constructions operate within a safe range. This is confirmed by very low values of tension in the elements of construction, which do not exceed 80 MPa. Additionally, the received temperature distributions in the area of construction, corresponding to 5 hours of continuous work of the machine, confirm the proper cooling of the body of the machine, preventing from the distribution of high temperature values into the material of the grooved section of the extruder.

Łukasz Majewski[1], Karolina Głogowska[1]

MANUFACTURING CHARACTERISTICS OF MACHINE COMPONENTS FOR PLASTICS PROCESSING ON THE EXAMPLE OF THE ACTIVE GROOVED FEED SECTION OF A SINGLE-SCREW EXTRUDER

Abstract: *Extrusion of polymeric materials is a complex technological process that, for the effective manufacturing of qualitatively satisfactory finished products or semi-finished products, requires consideration of many material, machine, technological and interfering factors. What we observe today is the emergence of new design solutions for plasticizing systems that enables the manufacturers both to attain greater control over the extrusion process, and the processing of increasingly demanding modern polymer materials. The present work introduces a design of an unconventional construction solution for a plasticizing system in form of an active grooved feed section of a single-screw extruder, and presents the description of its practical implementation, including the appropriate selection of construction materials and machining techniques*
Keywords: *grooved feed section section, thrust ring, inner support, feeding sleeve, segments, holders, adjustment screws, special nuts, cooling disc.*

1. Introduction

Screw extrusion is a process allowing the manufacture of finished products or semi-finished products in the process of continuous plasticization of a polymer material, and then extruding it through a fixed geometry nozzle. Even with this generally simple description of the entire process the manufacturing practice demonstrates that obtaining full control over it can be challenging. Establishing stable extrusion conditions requires both thorough experience and in-depth knowledge of the manufacturer. The dimensional repeatability of the resulting product is frequently adopted as the measure for extrusion stability, which requires a number of criteria, such as the characteristic moisture content and processability of the material, the viscous and elastic properties of plasticized polymers, the complicated nozzle geometry, the presence of fillers and processing aids, the geometry of the screw, and numerous other factors to be taken into account. Furthermore, the manufacturer frequently has to anticipate the disturbing factors that it is unable to prevent, such as the fluctuations of power supply voltage, air humidity (hindering the processing of biodegradable materials in particular), the autothermal effect resulting from friction, the swelling of the material stream leaving the extrusion nozzle, or the formation of pores. What is also of significance, apart from extrusion stability, is its efficiency, which influence the manufacturing speed of

[1] *Lublin University of Technology, Faculty of Mechanical Engineering, Department of Technology and Polymer Processing, ul. Nadbystrzycka 36, 20-618 Lublin, Poland, l.majewski@pollub.pl, k.glogowska@pollub.pl.*

products or semi-finished products. The plasticizing system has several important functions, which include transporting, plasticizing, mixing, compression and additionally shearing (conversion of the mechanical energy of the screw's rotational movement into heat energy). All these phenomena are interrelated and the change of technological and design factors will have different impact on each of them. We can quote the example of increasing the rotation speed of the screw, which will increase the mass flow rate, i.e. it will improve the extrusion efficiency, but the material will reside shorter in the plasticizing system, which will adversely affect its homogenization and the degree of its plasticization, and the increased shear rate may lead to overheating of the material at the barrel surface. Striving to achieve a stable and efficient extrusion process, technological methods can be applied to adopt the appropriate configuration of technological process parameters, such as temperature distribution and rotational speed of the extruder screw, or design methods that involve the use of new extruder design elements to improve its operation. The options also include application of solutions that combine both of the aforesaid methods, i.e. both the modification of design of the plasticizing system, which increases its processing capabilities, and the introduction of additional technological parameters, which once altered will give completely new opportunities to control the extrusion process. Such solutions include the rotational sleeve of the barrel and the Active Grooved Feed Section (AGFS).

The subject of the present chapter is the demonstration of methodology for manufacturing the active grooved feed section of a single-screw extruder in metal, taking into account the materials applied and the specificity of manufacturing individual components.

2. Material

During the operation of the extruder, extremely aggressive conditions prevail inside the plasticizing system, which can negatively affect not only the processed material, but also the structural elements of the machine itself. These aggressive factors include high temperature and pressure, significant shear stresses, the presence of water vapor and gases (in porous extrusion or thermal decomposition) additives, and fillers, and in particular those of mineral origin, which significantly increase the tribological wear of the operating parts of the extruder. Tribological wear can be divided into two varieties. Abrasive wear, which occurs primarily in the area of feeding sleeve, where the material is still solid, and in the areas located downstream from there, when extruding materials with the addition of solid fillers. The erosive wear occurs in the transformation and feeding zones during the processing of polymer compositions with hard fillers, and is particularly worth considering when using high rotational speeds of the screw because it damages the edges of the screw. The service life of extruder components can also be shortened by the corrosion inside the barrel caused by chemical reactions with water vapor released from the plastic, additional agents and plastic decomposition products. Once exposed to

corrosion the surface layer of the screw and the internal surface of the barrel are more susceptible to tribological wear.

Considering the aforementioned factors affecting the shortening of the life cycle of operating elements of the plasticizing system, it should be stated that the selection of structural materials is therefore crucial from the point of view of extrusion economics. Two types of certified steel were used to manufacture the components of the active grooved feed section. The first is 42CrMo4 (40HM), i.e. tool steel alloy used predominantly for machine and vehicle parts, especially those subjected to significant loads. It is characterized by easy machining and resistance to abrasion, and intended for thermal processing (quenching at 820-860°C, tempering at 540-680°C), and also suitable for nitriding. The exact elemental composition is listed in Table 1. The second type of steel is X46Cr13 (4H13), i.e. martensitic stainless steel alloy that is resistant to corrosive atmospheric agents, diluted acids and alkaline solutions, characterized by its good polishability. It is suitable for machining, nitriding and heat treatment (hardening at 950-1050°C, tempering at 650-700°C). It is frequently used for the production of machine parts in the chemical, petroleum and petrochemical industries. Its detailed elemental composition is presented in Table 1. The comparison of selected characteristics of both steel alloys is presented in Table 2.

Table 1. Elemental composition of 42CrMo4 and X46Cr13 steel alloys

Alloy	**C**	**Mn**	**Si**	**P**	**S**	**Cr**	**Ni**	**Mo**	**W**	**V**	**Cu**
	[%]										
42CrMo4	0.38-0.45	0.4-0.7	0.17-0.37	Max 0.035	Max 0.035	0.9-1.2	Max 0.3	0.15-0.25	Max 0.2	Max 0.05	Max 0.25
X46Cr13	0.45	0.5	0.6	Max 0.04	Max 0.03	13.5	-	0.5	-	0.2	-

Table 2. Summary of selected characteristics of the 42CrMo4 and X46Cr13 alloys

Alloy	**Annealed hardness**	**Improved hardness**	**Tensile strength**	**Yield point**	**Elongation at break**
	HB	**HRC**	**MPa**	**MPa**	**%**
42CrMo4	Max 240	Max 32	1030	880	12
X46Cr13	Max 225	Max 54	780	650	10-12

3. Equipment

What was required for the practical implementation of the active grooved feed section (AGFS) is the use a variety of different machining techniques, including turning, machining, EDM and grinding. Each machining step was carried out on a different machine, and below we will list all the equipment used.

All turning operations were performed with use of a SU-32 lathe, which enables machining of elements with a maximum diameter of 520 mm and a length of up to 1000 m. The permissible spindle speeds are in the range of 14 to 2500 rpm, and they can be set by selecting one of 16 gears. The machine is equipped with a 4kW electric motor with a maximum torque of up to 1000 Nm. The aforedescribed lathe is presented in Figure 1.

Fig. 1. The appearance of the SU-32 lathe

All technological operations involving the milling process were carried out on a MICRON VC Duro 800 CNC milling machine (Fig. 2). The device has a large operating area measuring x-800 mm, y-650 mm and z-500 mm. The milling machine is equipped with Heidenhain system devices enabling its precise positioning including measuring scales, rotary-pulse transducers, angle transducers, digital readings and numerical controls. The tool holder interface is ISO 40 compliant. The machine's rotational power reaches 15 kW, enabling tool speeds of up to 20,000 rpm. The tool holder can handle tools with a diameter of up to 90 mm, and the tool replacement time during machining is 8-9 s.

In Certain stages of the production of AGFS components required the application of EDM technology. Two different devices were used for processing in this technology. The first of these is the CHARMILLES FO 350S EDM (Fig. 3), equipped with a 500x400mm worktop enabling the processing of elements up to 500 kg. The worktop position can be adjusted in the x, y and z axes, by 350, 250 and 300 mm respectively. The resulting surface roughness Ra is 0.1 µm. In addition, the device is equipped with a cooling system that stabilizes the temperature of the process

Fig.2. MICRON VC Duro 800 CNC milling machine

and the workpiece and has a built-in fire protection system. The second EDM machine applied is the AGIE AC CLASSIC V3 (Fig. 3) with a mounted worktop measuring 500x350x426 mm, suitable for machining elements with maximum dimensions of 1050x650x420 mm and a weight of up to 400 kg. It can be equipped with wires with diameters ranging from 0.15 to 0.33 mm. It enables obtaining a roughness of the processed surface of Ra=0.1µm.

Fig. 3. Appearance of the EDM machines: CHARMILLES FO 350S (on the left) and AGIE AC CLASSIC V3 (on the right)

All finishing operations on AGFS components were performed on a GEIBEL HOTZ FS 640 SD CNC surface grinder (Fig. 4). The machine enables grinding of surfaces of elements weighing up to 600 kg and height up to 375 mm using a grinding wheel with a diameter of 600 mm and a width of 400 mm. The 3.7 kW electric motor allows for a maximum grinding wheel speed of 1400 rpm.

Fig. 4. The appearance of the GEIBEL HOTZ FS 640 SD grinder

4. Manufacturing procedure

The active grooved feed section consists of the following elements: thrust ring, inner support, feeding sleeve, segments I and II, holders I and II, N3 adjustment screws N3, M5 N3 special nuts, and the cooling disc. Work on the manufacture of the structural elements of the active grooved feed section of the extruder began with the elaboration of three-dimensional models corresponding to the adopted operating conditions. For this purpose, the Solid Edge computer system was used. It is the industry-leading CAD3D system with unique tools for creating physical prototypes. Using the operations in which the system is equipped, the appropriate shape of the elements of the active grooved feed section of the extruder was modelled and technical drawings executed.

In the subsequent stage of work, based on the previously executed 3D model, and taking into account the necessary technological allowances, a raw model of the active grooved feed section elements of the extruder was manufactured. After completing the two aforedescribed stages, we were able to start planning the technological process.

The paper presents the technological process of manufacturing each of the elements included in the structural construction of the active grooved feed section of the extruder.

Pressure ring

The pressure ring is one of the elements forming part of the structure of the active grooved feed section of the extruder. The element is made of 40HM (1.7225) steel for heat treatment. The technological process for the pressure ring consists of 4 operations. Operations 1 and 2 were performed on the SU-32 universal lathe, operations 4 and 3 were on the MICRON VC DURO 800 CNC milling machine. Figure 5 presents the view of the 3D model of the pressure ring.

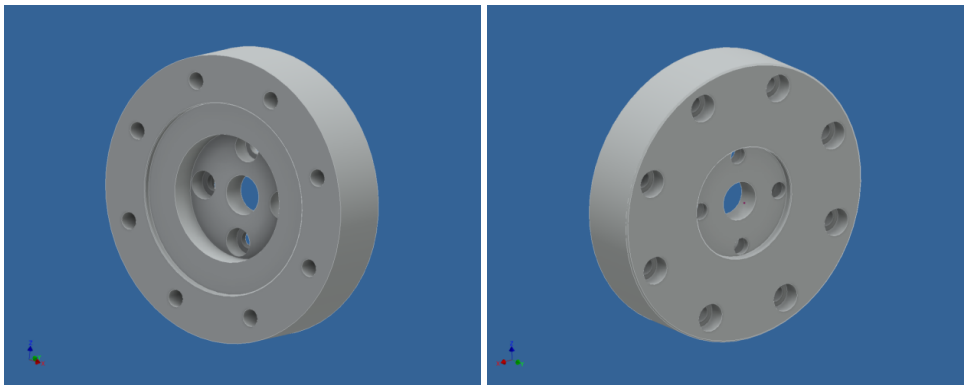

Fig. 5. Pressure ring model

- Operation 1 - clamping the external diameter of the workpiece, turning the front part, drilling ϕthe 120H7 and ϕ80 holes, drilling and boring the central ϕ25H8 hole - universal lathe.
- Operation 2 - clamping the workpiece on the ϕ25H8 centre hole, boring the ϕ72H7 hole diameter, turning the ϕ180 cylindrical, facing, edge chamfering - universal lathe
- Operation 3 - clamping the workpiece on the ϕ25H8 central hole, drilling the ϕ4x11 holes, countersinking the holes to ϕ4x18 - CNC milling machine.
- Operation 4 - clamping the workpiece on the ϕ25H8 central hole, drilling ϕ8x11 holes, countersinking the holes to ϕ8x18 - CNC milling machine. The appearance of the finished pressure ring is presented in Figure 6.

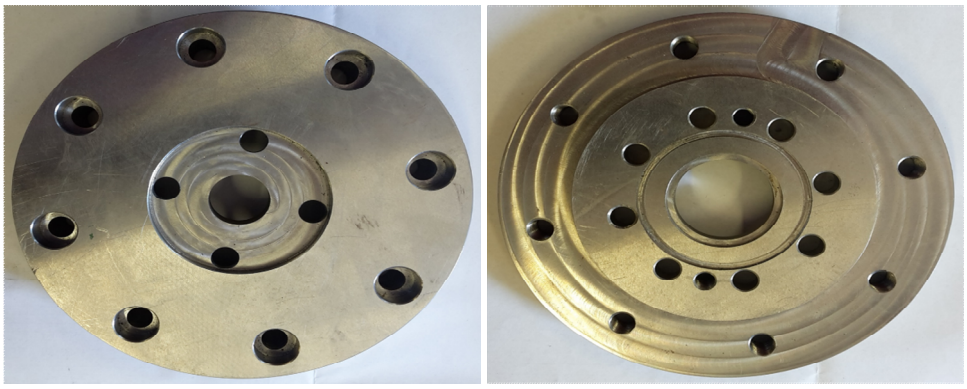

Fig. 6. Appearance of the finished pressure ring

Inner support

The next element forming part of the active grooved feed section of the extruder is the inner support. The element is made of 40HM (1.7225) steel for heat treatment. The technological process for the manufacture of internal support consists of 7 operations. Operation 1 was performed on the SU-32 universal lathe, operations 2 and 5 were performed on the AGIE AC CLASSIC V3 wire cutter, operation 3 was performed on the GEIBEL HOTZ FS 640 SD cylindrical grinder, operations 4 and 6 were performed on the MICRON VC DURO 800 CNS milling machine, and operation 7 was carried out on the CHARMILLES FO 350 S electro-drilling machine. The view of the 3D model of the inner support is presented in Figure 7.

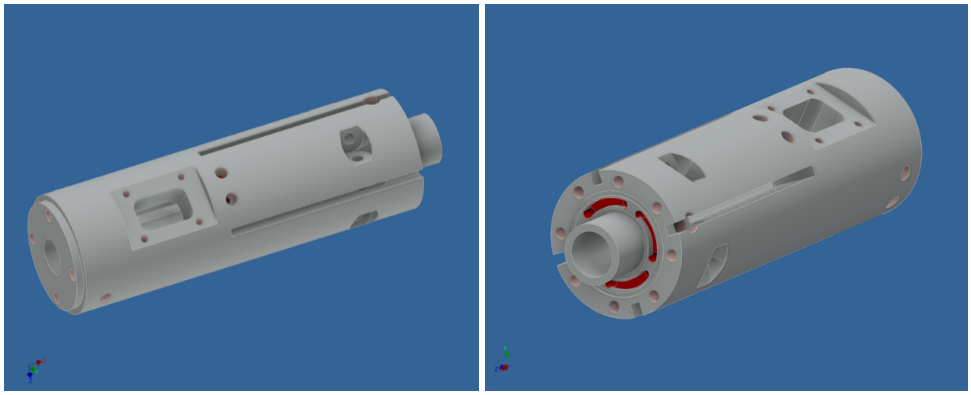

Fig. 7. Model of the inner support

- Operation 1 - clamping the workpiece on its outer diameter, initial turning of the external diameter of the workpiece:ϕ 80, ϕ72, ϕ33, finishing turning with grinding allowances ϕ80h6, ϕ72h6, ϕ33h6, drilling and turning the central ϕ25H8 hole - universal lathe.
- Operation 2- clamping the workpiece on its outer diameter, cutting the ϕ25 H8 central hole - wire cutter.
- Operation 3 - clamping the workpiece on its ϕ25 H8 internal diameter, grinding the surface of the outside diameter: ϕ80 h6, ϕ72 h6, ϕ33 h6 - roller grinder.
- Operation 4 - clamping the workpiece on its ϕ25 H8 internal diameter, boring 6 x ϕ5x233, 2 ϕx5 x 137 holes, drilling and tapping 4 x M10 holes to a depth of 20mm, 4x5mm slot milling, turning ϕ57.5 and ϕ38.4 face grooves, chamfering sharp edges - CNC milling machine.
- Operation 5 - cutting (partial) of channels in the workpiece 4xϕ6 H7 - wire cutting machine.
- Operation 6 - clamping the workpiece on its ϕ25H8 inner diameter, milling sockets 62x6 and 22.5x38 (maintaining the R6 radius), drilling and tapping

4xM6 holes to a depth of 12mm, milling a cylindrical hole to size of 36mm, drilling and reaming 4 x ϕ8H7 holes, drilling and tapping 6 + 2xG1/8” holes, drilling and tapping ½ -20 UNF holes, milling 4x6H7 grooves - CNC milling machine.

- Operation 7 - final finish of internal radii of the sockets (R100, R155, R15) 4x6H7 - electric drilling machine. The appearance of the finished internal support of the active grooved feed section of extruder is presented in Figure 8.

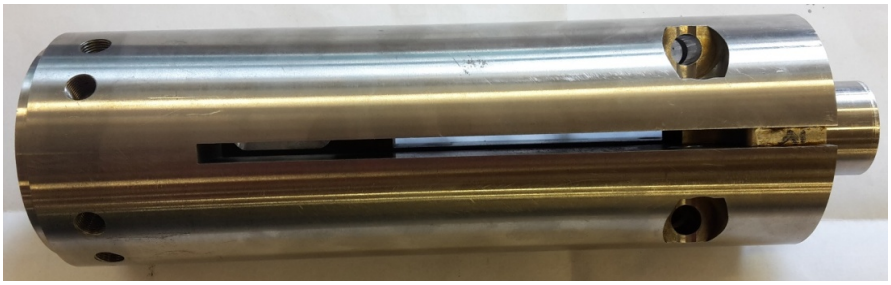

Fig. 8. Appearance of the finished inner support

Feeding sleeve

Another element of the construction of the active grooved feed section of the extruder is its feeding sleeve. This part is made of 40HM (1.7225) steel for heat treatment. The technological process of the feeding sleeve consists of 6 operations. Operation 1 was performed on the SU-32 universal lathe, operation 2 was performed on the GEIBEL HOTZ FS 640 SD cylindrical grinder, operations 3 and 5 were performed on the MICRON VC DURO 800 numerical milling machine, operations 4 and 6 were carried out on the AGIE AC CLASSIC V3 wire cutter. The view of the 3D model of the feeding sleeve is presented in Figure 9.

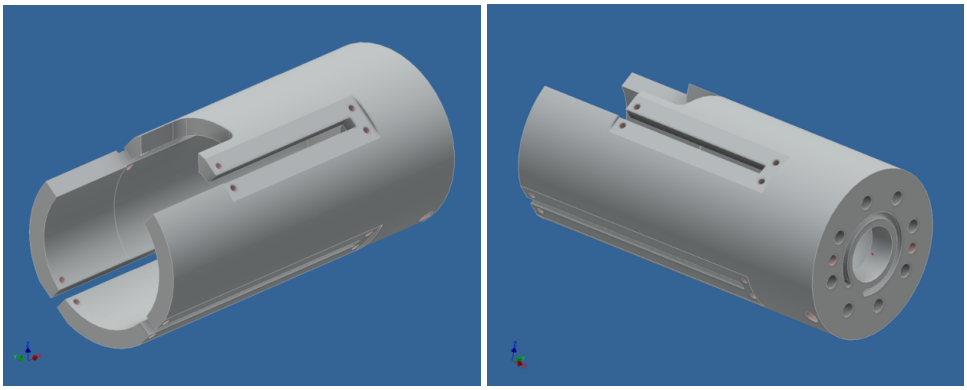

Fig. 9. Model of the feeding sleeve

- Operation 1 - turning external workpiece diameters: ϕ100, ϕ80 H7, ϕ33H7 with allowances - universal lathe.
- Operation 2 - grinding the outside ϕ100 diameter - roller grinder.
- Operation 3 - milling the ϕ41.5x4mm channel in the workpiece (keeping the R2 radius), drilling 8xϕ8.5 holes, drilling and tapping 2xM8 holes, drilling the ϕ4 and ϕ8 diameter holes - CNC milling machine.
- Operation 4 - (initial) cutting of the 4x 6H7 channel in the workpiece - wire cutter.
- Operation 5 - clamping the workpiece on its ϕ33 internal diameter, 4 x L = 115mm face milling, drilling the ϕ13 hole, drilling and tapping the 4x4 M6 holes, drilling and tapping the 2x G1/8" holes - CNC milling machine.
- Operation 6 - cutting the 4xϕ7 channel in the workpiece- wire cutter. The appearance of the finished feeding sleeve of the active grooved feed section of the extruder is presented in Figure 10.

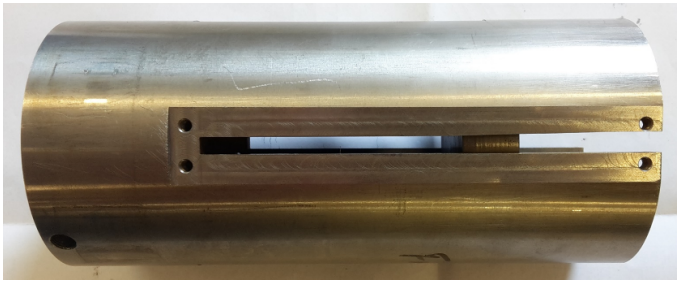

Fig. 10. Appearance of the finished feeding sleeve

Segments I and II

The active grooved feed section of the extruder is made of the following segments: I and II, which are both made of high quality alloy - the stainless chromium 4H13 steel. These segments differ in length. The length of segment I is 115mm, the length of segment II is 170mm. The technological process for segments I and II consists of 4 operations. Operations 1 and 2 are performed on the GEIBEL HOTZ FS 640 SD surface grinder, operations 3 and 4 are performed on the AGIE AC CLASSIC V3 wire cutter. The view of the 3D model of segments I and II is presented in Figure 11.

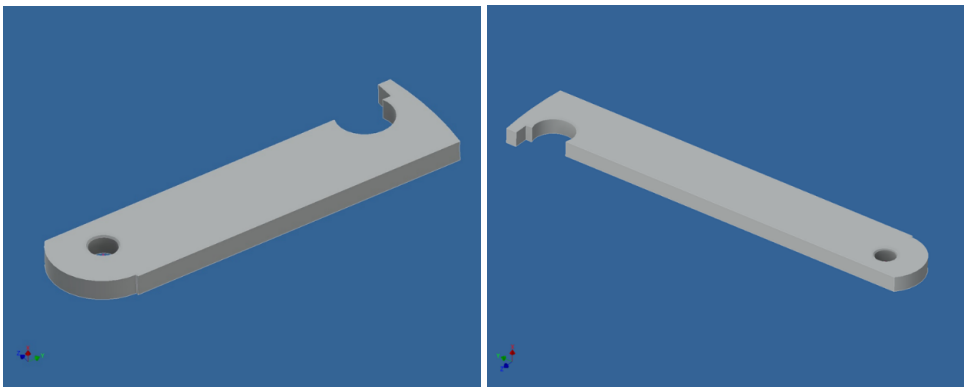

Fig. 11. Model of segments I and II

- Operation 1 - grinding the lower surface of the part - surface grinder.
- Operation 2 - grinding the upper surface of the part - surface grinder.
- Operation 3 - cutting the external profile, cutting the ϕ8H7 hole - wire cutter.
- Operation 4 - cutting the outer edge R12.5 radius - wire cutter. The appearance of the finished segments of the active grooved feed section of the extruder is presented in Figure 12.

Fig. 12. Appearance of the finished segments I and II

Holders I and II

The next elements of the construction of the active grooved feed section of the extruder are holders I and II. These details are made of 40HM (1.7225) steel for heat treatment. The holders differ in their length. The length of holder I is 114mm, the length of holder II is 169mm. The technological process for holders I and II consists of 3 operations. Operations 1 and 2 are performed on the MICRON VC DURO 800 CNC milling machine, operation 3 was carried out on the AGIE AC CLASSIC V3 wire cutter. The view of the 3D model of the holders I and II is presented in Figure 13.

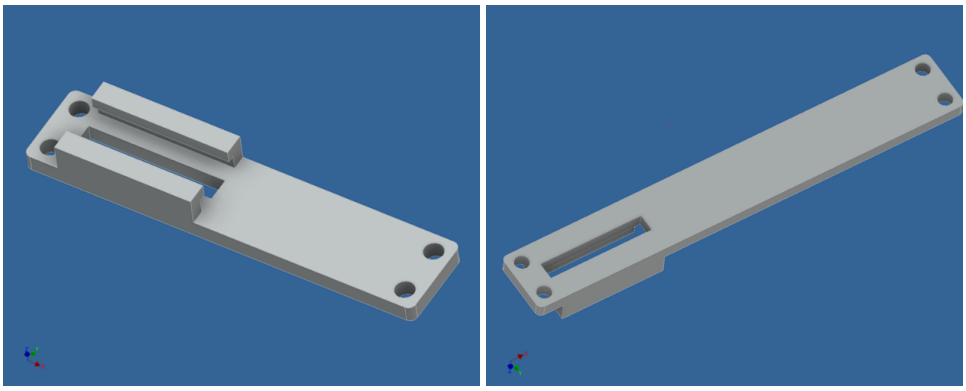

Fig. 13. Model of holders I and II

- Operation 1 - milling the external plane of the workpiece - CNC milling machine.
- Operation 2 - milling the internal plane of the workpiece and drilling 4xϕ5.5 holes - CNC milling machine.
- Operation 3 - cutting the 6.7x40 channel in the workpiece- wire cutter. Appearance of the finished holders is presented in Figure 14.

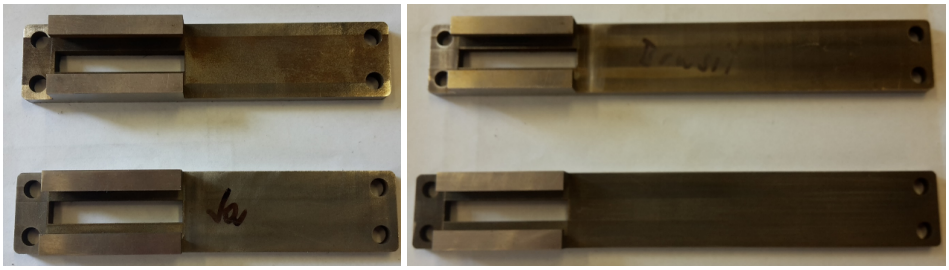

Fig. 14. Appearance of the finished holders I and II

N3 adjustment screw

The N3 adjusting screws included in the design of the active grooved feed section of the extruder are made of 40HM (1.7225) steel for heat treatment. The technological process for the adjustment screws consists of 3 operations. Operation 1 is performed on the SU-32 universal lathe, operation 2 is carried out on the GEIBEL HOTZ FS 640 SD surface grinder, and operation 3 on the AGIE AC CLASSIC V3 wire cutter. The view of the 3D model of the N3 adjustment screw is presented in Figure 15.

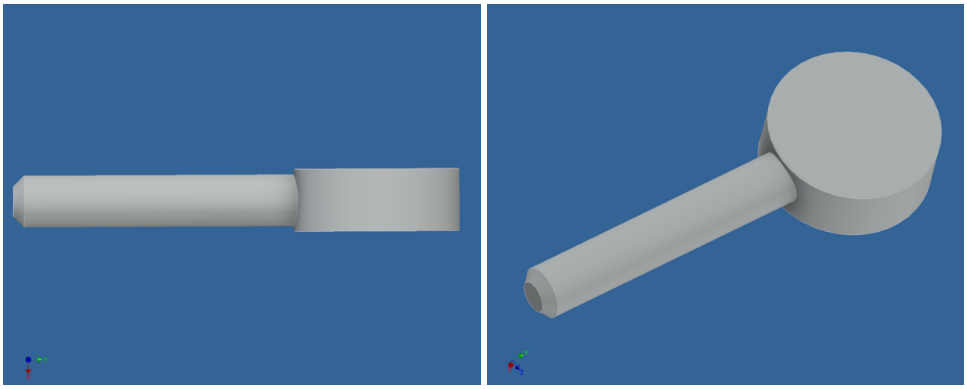

Fig. 15. Model of the N3 adjustment screw

- Operation 1 - turning of the cylindrical part, M5 threading of the 20mm section - universal lathe.
- Operation 2 - precise surface grinding to the thickness of 6h6 - surface grinder.
- Operation 3 - cutting the ϕ16h6 outer diameter of the workpiece - wire cutter. The appearance of the finished N3 adjustment screws is presented in Figure 16.

Fig. 16. The appearance of the finished N3 adjustment screws

M5 N3 special nuts

The M5 N3 special nuts are made of 40HM (1.7225) steel for heat treatment. The technological process for M5 N3 special nuts consists of 2 operations. Operation 1 is performed on the SU-32 universal lathe, operation 2 on the MICRON VC DURO 800 CNC milling machine. The view of the 3D model of M5 N3 special nuts is presented in Figure 17.

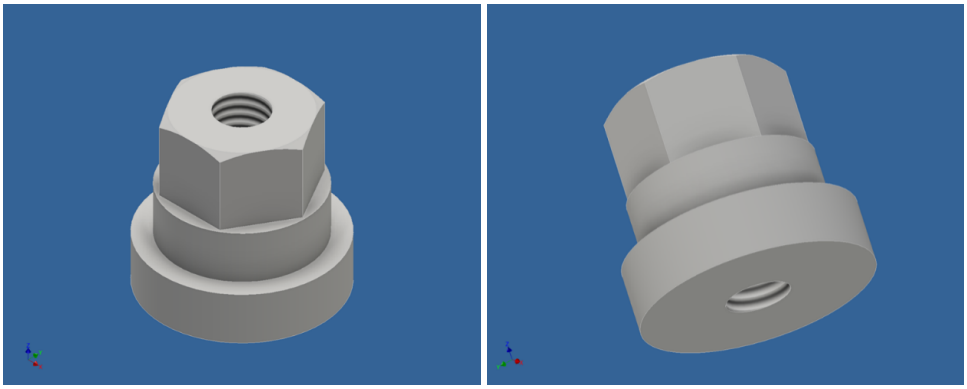

Fig. 17. Model of the M5 N3 special nut

- Operation 1 - facing, turning external shapes, drilling and M5 threading - universal lathe.
- Operation 2 - hexagon head milling, 30^{o} chamfers- CNC milling machine. The appearance of the finished M5 N3 special nuts is presented in Figure 18.

Fig. 18. Appearance of finished M5 N3 special nuts

Cooling disc

The last element of the design of the active grooved feed section of the extruder is its cooling disc. The element is made of 40HM (1.7225) steel for heat treatment. The technological process for the cooling disc consists of 3 operations. Operations 1 and 2 are performed on the SU-32 universal lathe, operation 3 on the MICRON VC DURO 80 CNC milling machine. The view of the 3D model of the cooling disc is presented in Figure 19.

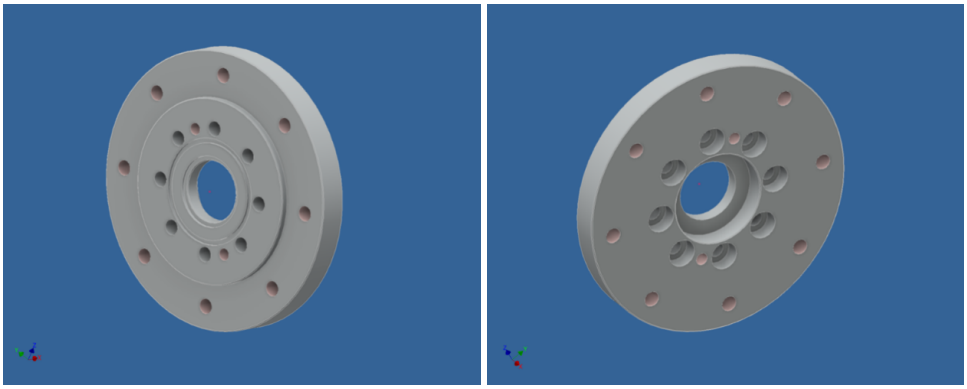

Fig. 19. Cooling disc model

- Operation 1 - facing of the front face of the workpiece, drilling and turning the ϕ33 H7 hole and making the ϕ50H7 crest - universal lathe.
- Operation 2 - clamping on the inside ϕ33H7 diameter of the workpiece, facing the face, turning the ϕ100h6, ϕ38.4H11, ϕ 57.4H11, ϕ150 dimensions, cutting the channel, chamfering - universal lathe.
- Operation 3 - clamping on the ϕ33H7 internal diameter of the workpiece, drilling 8xϕ8.4 holes, countersinking 8xϕ15 holes, drilling and threading 2xM8 and 8xM10 threading - CNC milling machine. The appearance of the finished cooling disc is presented in Figure 20.

Fig. 20. Appearance of the finished cooling disc

Figure 21 presents all the components included in the design of the active grooved feed section of the extruder.

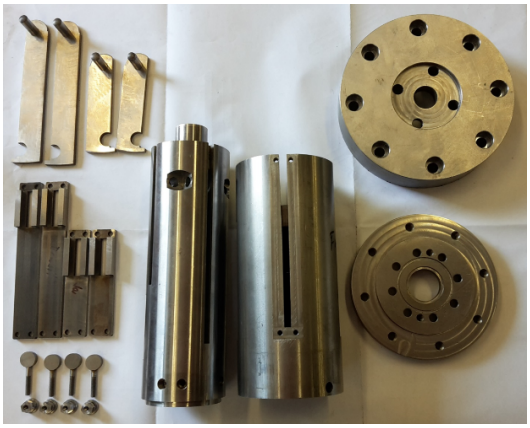

Fig. 21. Elements forming part of the design of the active grooved feed section

5. Conclusion

Single-screw extrusion is a complicated technological process that is only justified in economic terms, when it is applied to mass scale manufacturing. Due to the numerous issues faced by the manufacturers, any improvement of the extrusion process is useful to allow it to be better controlled or to improve the stability of quality and accuracy of the elements that are manufactured faster. The active grooved feed section of the extruder is an example of a solution for improvement of the processing capabilities of the entire extrusion line, introducing additional technological parameters and further control options for the stability and efficiency of the extrusion process. Considering the wear processes occurring during extrusion, as well as the physical and chemical phenomena, it is necessary to properly select materials and technologies for the manufacturing of components to ensure their uninterrupted and long-term operation.

This project has received funding from the European Union's Horizon 2020 research and innovation programme under the Marie Skłodowska-Curie grant agreement No. 734205 – H2020-MSCA-RISE-2017.

Ľudmila Dulebová[1], Ján Varga[1], František Greškovič[1], Anna Rudawska[2]

EVALUATION OF ADHESION WEAR OF CONTACT SURFACES OF MOLDS

Abstract: *Adhesive wear can be found between surfaces during frictional contact and generally refers to unwanted displacement and attachment of wear debris and material compounds from one surface to another. This contribution is focused on dealing adhesive wear of tool steels for production of molds inserts used with polyamide. Experiments were realized by the simulation of adhesive wear using laboratory Amsler equipment, which allows the testing of dry friction pairs. The adhesive wear of the tool steels was evaluated by the weight loss of the steel before and after wear, by changing the friction coefficient of friction pairs and by changing the roughness of the tool steel before and after wear.*
Keywords*: adhesive wear, friction coefficient, tool steel, polyamide*

1. Introduction

Polymer materials present a chemical assembly which is defined by their unusual variability of structures and final matter properties. Due to their properties, these materials are widely used nowadays. Intensive development of new types of polymer materials, the rapid development of their industrial production in recent years and especially their application in various sectors of industrial activity have resulted in rapidly increase of demand for tools to process them. [1,2]. The most expanded plastic processing technology is extrusion and injection molding and products are produced in molds [2,3].

Materials for molds for those technologies must fulfil for example the required operational conditions, temperature, pressure and abrasion resistance. For molds and related parts, the most commonly used structural and tool steels with this properties: surface quality, corrosion resistance, fatigue resistance, wear resistance and etc.[3]. The wear assessment of molds of those materials can be monitored using friction pairs with specific polymer materials. In the experiments, the friction ratios in the production of products are simulated by an adhesive wear test of tool steels [4,5]. The wear intensity of the materials is evaluated by determining the friction coefficient and by determining the magnitude of the relative wear based on the weight losses of the tested materials. At the same time, it is possible to analyze the change in the surface morphology of steels or polymer materials in individual friction pairs after wear [6].

[1)] *Department of Engineering Technologies and Materials, Faculty of Mechanical Engineering, Technical University of Kosice, Masiarska 74, 040 01 Kosice, Slovakia, ludmila.dulebova@tuke.sk, jan.varga@tuke.sk, frantisek.greskovic@tuke.sk*

[2)] *Department of Production Engineering, Lublin University of Technology, 36 Nadbystrzycka St., 20-618 Lublin, Poland, a.rudawska@pollub.pl*

1.1. Adhesive wear

The study of the processes of wear is part of the discipline of tribology. The complex nature of wear has delayed its investigations and resulted in isolated studies towards specific wear mechanisms or processes. Some commonly referred to wear mechanisms (or processes) include:

- adhesive wear,
- abrasive wear,
- surface fatigue,
- fretting wear,
- erosive wear [7].

Adhesive wear occurs between two solids which are in a sliding contact and the atomic bonding forces occurring between the materials on the interface are stronger than the strength of the surrounding area in either of the materials [8]. Adhesive wear is one of the most frequently encountered types of wear.

Adhesive wear involves the contact and interaction of asperities on two surfaces with strong adhesive force. Adhesive wear is promoted by two major factors:

1. The tendency for different materials to form solid solutions or intermetallic compounds with one another. Thus, material combinations of different crystal structure and chemical properties tend to have lower adhesion. Low adhesion may result in low wear rate and friction, provided that other properties and surface geometries are the same.
2. The cleanliness of the surface. Cleaner surfaces are more likely to bond together. Surfaces having a thick and adherent oxide film have low wear. Stainless steels and nickel alloys that do not form thick oxides have poor adhesive wear resistance [1,5].

In adhesive wear, shear starts in the weakest material and the fragment of a surface (wear particle) is detached from one body and transferred to another. Wear particles detach at the areas where a strong junction between contacting asperities is formed between the surfaces sliding relative to one another [7].

Adhesive wear can be found between surfaces during frictional contact and generally refers to unwanted displacement and attachment of wear debris and material compounds from one surface to another [8]. Two separate mechanisms operate between the surfaces:

- adhesive wear is caused by relative motion, "direct contact" and plastic deformation which create wear debris and material transfer from one surface to another
- cohesive adhesive forces, holds two surfaces together even though they are separated by a measurable distance, with or without any actual transfer of material [5,6].

The conditions affecting wear are as follows:

- External conditions include the working environment (temperature, pressure, chemical activity); the working medium (flow rate, particle content, hardness, shape and the numbers of particles, the conditions of impact on surface); the dynamic loading of functional surface.
- Internal conditions include the suitability of form to estimated function, theappropriateness of the material selection; the suitability of production technologies; the occurrence of errors, which distort the proper functioning of components.
- Working conditions include a comparison of real conditions of operation with prescribed conditions; the continuous or intermittent overloading of working conditions; operator's errors in the management of machine or device [5,7].

The aim of experimental works was to analyse the resistance of selected tool steels designed for die parts production against wear in the course of interaction with thermoplastics in adhesive wear conditions.

2. Experimental work

2.1 Test material and experimental tests methods

To determine the adhesive wear of the samples were selected materials, which suitable for producing of die. The test materials tool steels type 1.2842 (90MnCrV8), 1.2714 (56NiCrMoV7), 1.2842 (90MnCrV8), 1.2080 (X210Cr12) and tool steel 1.2343 (X38CrMoV5-1) were used for experiment.

Chemical composition of evaluated tool steels is shown in Table 1.

Table 1. Chemical composition of evaluated tool steels

Tool Steel	Chemical composition, %								
	C	Cr	Mn	P	S	Si	Ni	Mo	V
1.2842 (90MnCrV8)	0.85	0.20	2.00	0.03	0.03	0.10	-	-	0.05
1.2714 (56NiCrMoV7)	0.55	1.10	0.50	0.03	0.03	0.30	1.70	0.40	0.15
1.2842 (90MnCrV8)	0.90	0.35	2.00	0.03	0.03	0.25	-	-	0.10
1.2080 (X210Cr12)	1.95	12.0	0.20	0.03	0.03	0.20	-	-	-
1.2343 (X38CrMoV5-1)	0.37	5.00	0.20	0.03	0.03	1.00	0.35	1.40	-

The specific plastic test material (material of friction pair) was Ravamid B NC, which is a Polyamide 6 product. Polyamide 6 belongs to the group of so-called structural thermoplastics. This material has excellent properties and a wide range of

processing options. The material properties of PA6 are as follows: density 1 140 kg/m^3, yield strength 80 MPa, elongation> 50 %, hardness HB 150 / DIN 53456, coefficient of friction 0.35, and sliding wear 0.23 μm/km.

The evaluation of the adhesive wear of tested materials was performed using the following methods:

- Structural analysis of individual tool steels
- Hardness test of materials according to EN ISO 6507-1
- The valuation of surface roughness according to EN ISO 4287
- The evaluation of adhesive wear - coefficient of friction and weight loss

Structural analysis of the tool steel was performed on metallographic sections at the light microscope type Olympus VANOX AHA-2.

The hardness of materials was determined by Vickers method according to standard STN EN ISO 6507-1 and was measured using hardness tester HPO 250.

The surface roughness was determined using a touch type – profilometer Surftest SJ-301, which works by scanning of the surface using diamond tipped probe with radius of curvature of 5 μm, placed on a suspension arm. Microgeometry of the surfaces of the friction pairs was evaluated by standard STN EN ISO 4287. The method and direction of the roughness measurements of the samples from tool steel was chosen for the width labelled S90 and with the length labelled D0 (Figure.1).

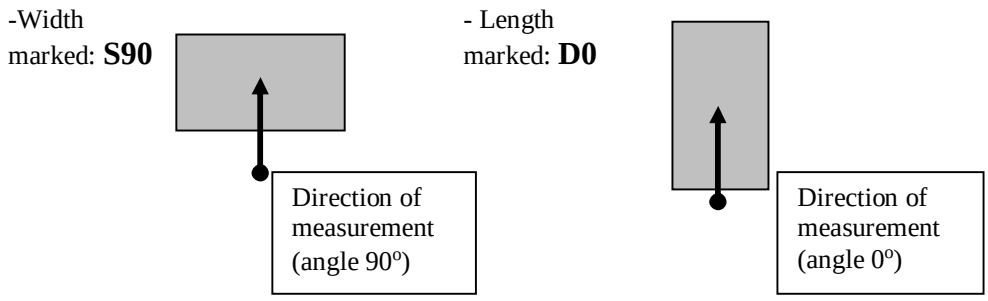

Fig. 1. Method and direction of roughness measurement

Adhesive dry wear test was carried out on Amsler equipment with area contact of tested samples.In friction couple the disk was made of tool steel (diameter φ 36 mm and thickness 10 mm) and friction mates made from polyamide were of square shape (20x15x8 mm). Friction couple materials were held together by spring of normal force F_n = 50 kN, disk speed was 200 min^{-1}, time of friction test 30 min. During thetest, the friction moment μ and tool steel weight loss W_h were observed every 5 minutes. Layout of Amsler equipment and arrangement of friction couple is shown in Figure 2.

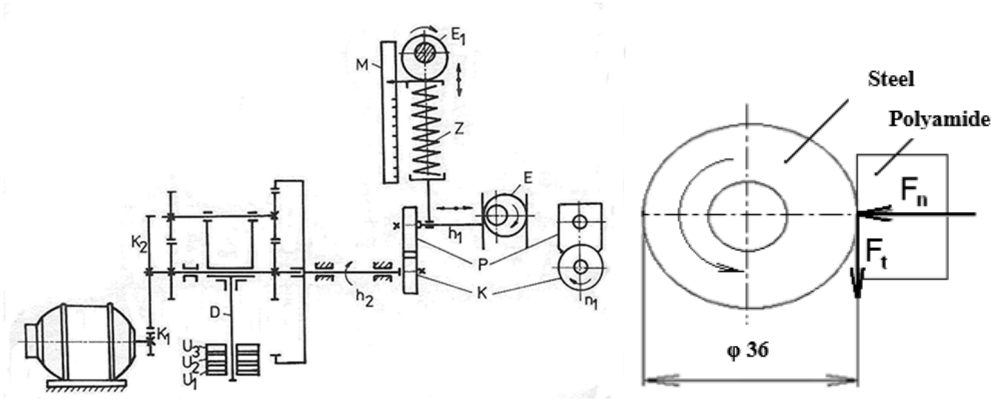

Fig. 2. Layout of Amsler equipment (a), Acting forces in friction couple (b)
K – disc, P – splice plate, Z – pressure spring, E, E_1 – excenters, D - dynamometer

Before adhesion wear test all test samples were degreased. The equipment contains dynamometer by which friction moment M was continuously measured. Friction moment M is given by equation (1):

$$M = r \,.\, F_t \quad [N.mm], \qquad (1)$$

Friction force F_t is given by equation (2) from friction moment M:

$$F_t = M / r \quad [N], \qquad (2)$$

Friction coefficient μ is determined as ratio of friction force and normal force (3):

$$\mu = F_t / F_n \quad [-], \qquad (3)$$

where: M – friction torque [N.m], F_t – friction force [N], r – disk radius [mm], F_n- contact force [N], μ - friction coefficient [-].

2.2 Experimental result and discussion

The structure of the tested tool steels is shown in Fig.3. The evaluated tool steels had a predominantly austenitic structure. The 55NiCrMoV7 tool steel had an austenitic-martensitic structure, and in the X210Cr12 steel, massive primary Cr carbides were visible.

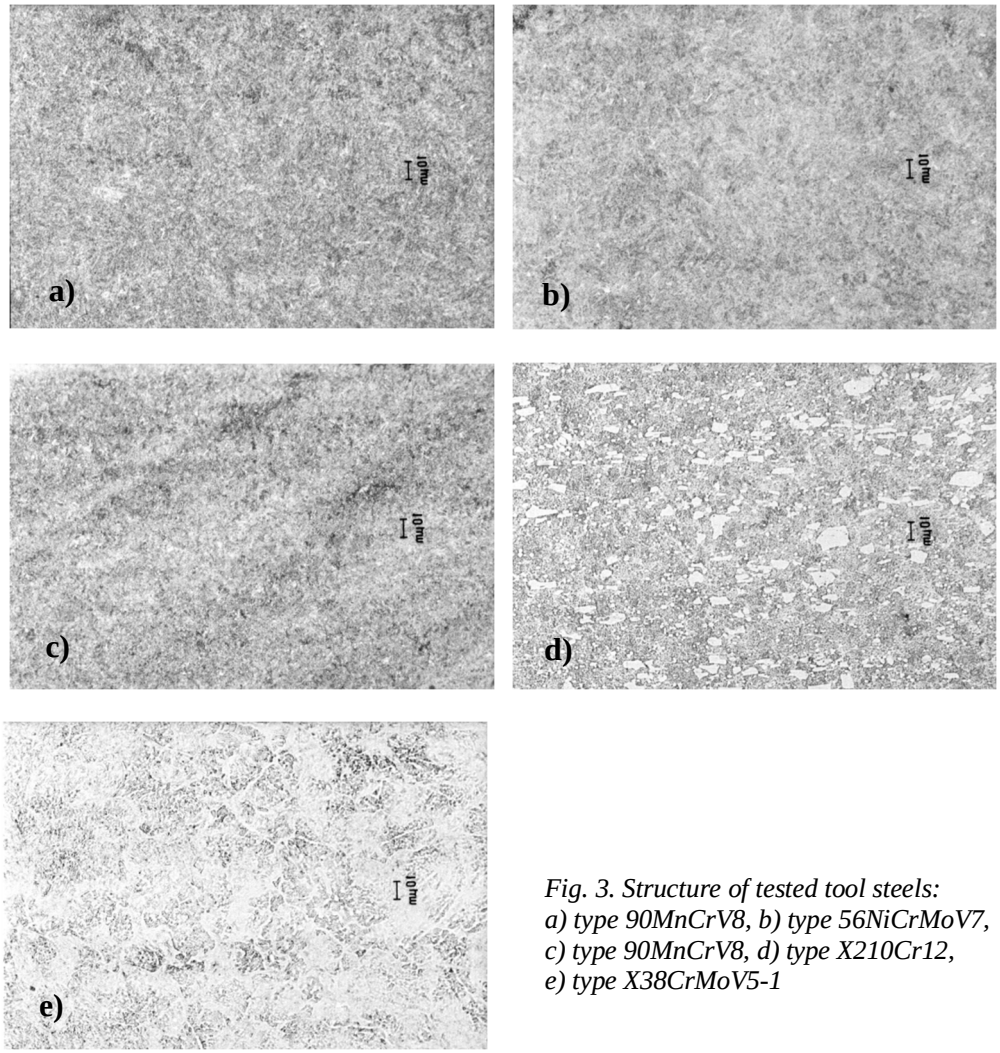

Fig. 3. Structure of tested tool steels:
a) type 90MnCrV8, b) type 56NiCrMoV7,
c) type 90MnCrV8, d) type X210Cr12,
e) type X38CrMoV5-1

Directional hardness values (converted to HRC) of the tested materials are shown in Fig.4. The measured results show that the highest hardness value was achieved by steel X210Cr12 and the lowest by steel X37CrMoV5-1. Other steels had relatively balanced hardness values.

Material X210Cr12 achieved the highest values of hardness (HRC 61) given by the amount of alloying elements and it was therefore possible to assume the highest wear resistance of the material. But during the wear, there was husking of chromium precipitates from the ledeburitic matrix in the form of pitting, which crucially affected the rate of material wear. The best wear resistance to exhibited specimens had material X38CrMoV5-1.

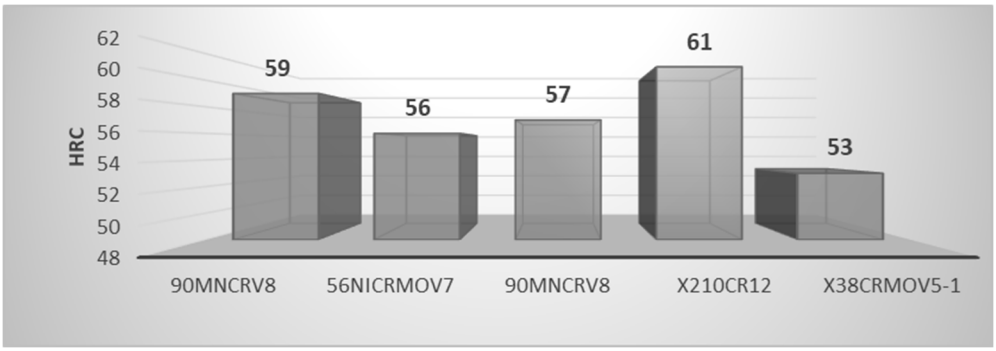

Fig.4. Directional hardness values of tested tool steels

During the adhesive wear test, coefficient of friction, weight loss and roughness change of grinding pairs, (steel - polyamide) were observed. The results of measurements of friction coefficients related to time are presented in Table 2. The course of the friction coefficient „μ" for the specifically evaluated friction pairs is shown in Figure 5.

Table 2. Average values of friction coefficient depending on the measurement time periods

Material	Friction coefficient μ in time periods						
	μ [-] 0min	μ [-] 5min	μ [-] 10min	μ [-] 15min	μ [-] 20min	μ [-] 25min	μ [-] 30min
90MnCrV8	0.085	0.115	0.122	0.152	0.148	0.152	0.152
56NiCrMoV7	0.085	0.115	0.126	0.141	0.152	0.152	0.163
90MnCrV8	0.082	0.126	0.133	0.145	0.167	0.167	0.163
X210Cr12	0.074	0.104	0.115	0.126	0.130	0.141	0.148
X38CrMoV5-1	0.074	0.096	0.107	0.107	0.115	0.119	0.122

The comparison of the measured friction coefficients shows that the lowest measured value of the friction coefficient was reached in the friction pair X38CrMoV5-1 – PA6.

The size of the adhesive wear was evaluated by a quantitative method, i. by changing the weight of the test specimens. The weight losses of tool steels are shown in Table 3 and in Figure 6.

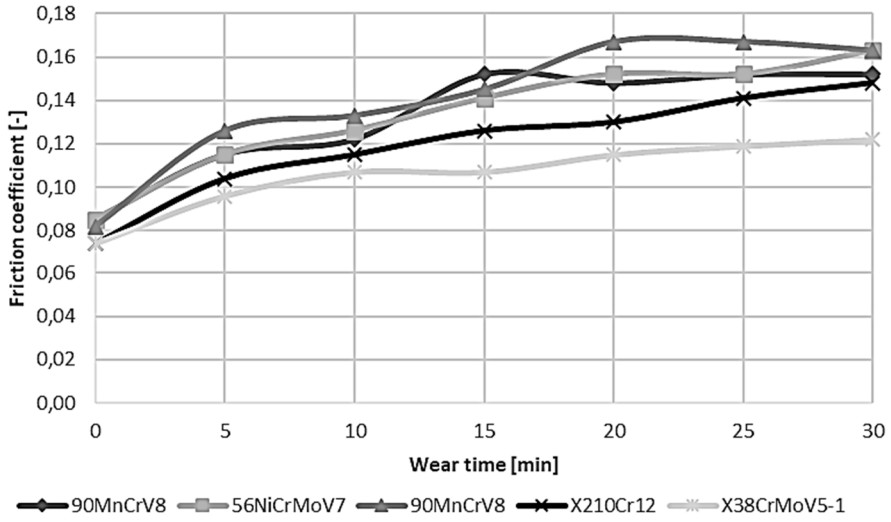

Fig.5. Friction coefficient of tool steels in friction pair with PA

Table 3. Measured weights of samples before and after adhesive wear

Material	Weight of material before test, g	Weight of material after test, g	Weight-difference, g
90MnCrV8	23.4651	23.4351	0.0300
56NiCrMoV7	23.6400	23.5941	0.0459
90MnCrV8	23.4843	23.4733	0.0110
X210Cr12	23.2788	23.2635	0.0153
X38CrMoV5-1	23.3606	23.3600	0.0006

The largest mass removal of material was for 56NiCrMoV7 steel. The lowest mass removal of the material was for X38CrMoV5-1 steel.

Based on the experimentally obtained results in the simulation of adhesive wear of steel materials in combination with PA6, it can be stated that all steels showed low wear intensity. Relatively low wear values of all steels were achieved by the ratio of the hardness of the friction pairs and the material characteristics of PA6.

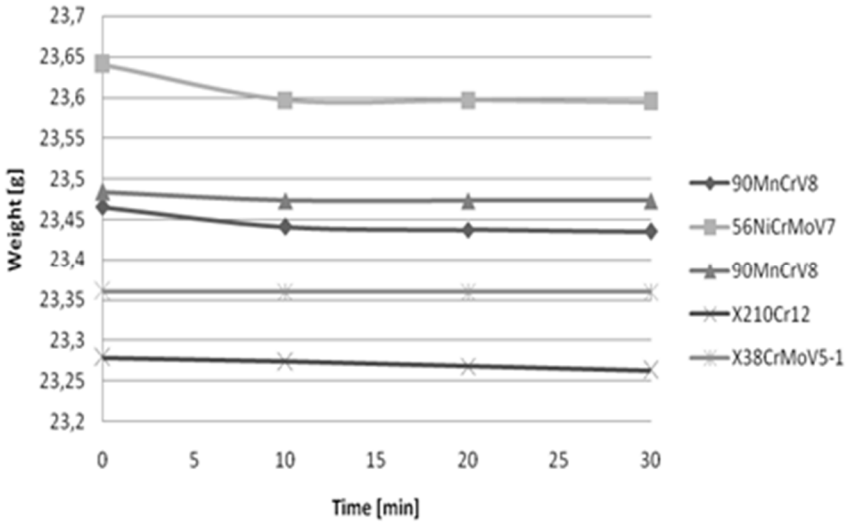

Fig. 6. Weight loss of tool steels by friction process with PA6 material

Another important factor influencing the size of wear of the evaluated materials is the relief of macro and micro irregularities of the contact surfaces of the pairs. The results of the measurements of the surface roughness of materials are listed in Table 4 and showed in Figures 6 and 7.

Table 4. Measured values Ra, Rz of tested materials

Direction of measurement	Material	Average Ra,μm		Average Rz,μm	
		Before wear	After wear	Before wear	After wear
S90	90MnCrV8	0.26	0.30	1.96	2.11
D0		0.10	0.49	0.65	2.44
S90	56NiCrMoV7	0.32	0.37	2.30	3.02
D0		0.12	0.41	0.83	2.56
S90	90MnCrV8	0.32	0.32	2.43	2.23
D0		0.10	0.21	0.64	1.16
S90	X210Cr12	0.28	0.27	2.15	1.71
D0		0.14	0.10	0.89	0.72
S90	X38CrMoV5-1	0.34	0.29	2.57	1.95
D0		0.13	0.16	0.90	0.99

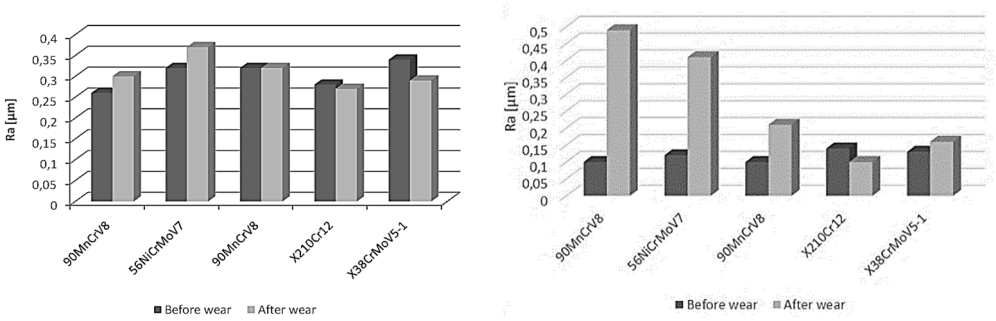

a) *b)*

Fig. 6. Average Ra in direction S90 (a) and in direction D0 (b) of tested materials

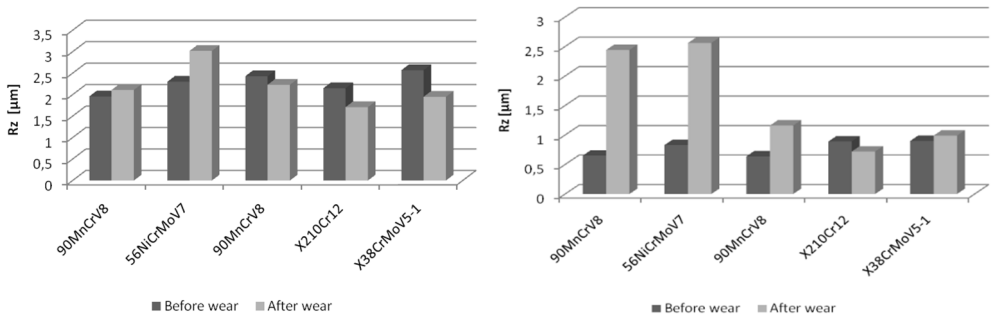

a) *b)*

Fig. 6. Average Rz in direction S90 (a) and in direction D0 (b) of tested materials

Frictional contact of materials leads to elastic and plastic deformation of jog peaks of the functional surfaces. During the plastic deformation the surface layers in contact may break. Subsequently, the formation of micro-joints and the accompanying surface firming of surface layers is observed. At the same time, there is a transfer of material particulate to the contact surface, depending on the material characteristics of the grinding pairs. The amount and size of the grooves was proportional to the hardness of the evaluated materials. Knurling intensity also depends on the phase separation tendency in the interphase of the interface in the polymer material and on the adhesion size of the contact phases.

The greatest change of material roughness Ra and Rz in the direction D0 was showed for 90MnCrV8 steel and the smallest change roughness was measured for X38CrMoV5-1 steel. In direction S90, the changes in roughness values showed a smaller displacement. The smallest deviations were measured for 90MnCrV8 steel.

The profilographs of the X38CrMoV5-1 steel surface before and after wear, made perpendicular to the direction of friction, are shown in Figure 7. The nature of

wear was also demonstrated spatially using Matlab software. When comparing the surface reliefs before and after wear, it can be stated that the character of the surface after contact with PA6 did not change significantly. However, based on the change in the evaluated roughness characteristic there was a slight smoothing of the surface during wear.

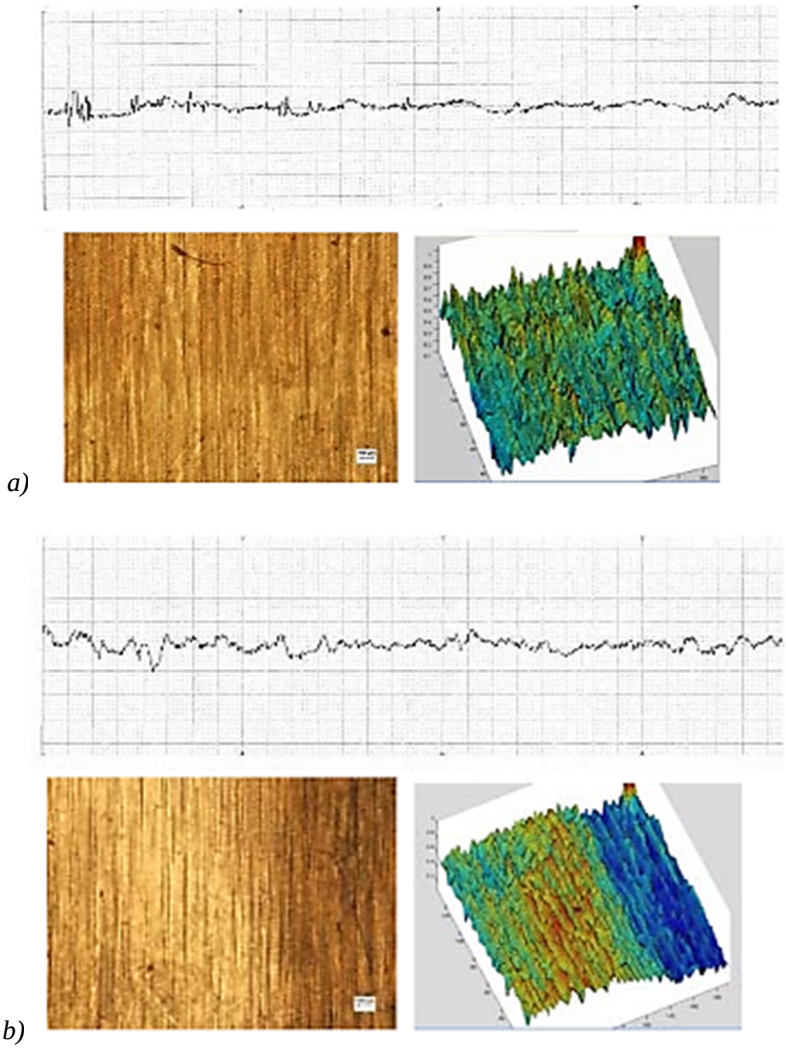

Fig.7. Profilographs (hor. mag. 50x, vert.mag. 10000x), macroimagines (mag.100x) and 3D presentationof steel surface X38CrMoV5-1 before (a) and after (b) wear

3. Conclusion

This paper presents the results of the tribological properties of selected types of tool steels. The materials were chosen on hardness, chemical composition and structural bases. Experiments were realised by the simulation of adhesive wear using laboratory equipment (Amsler), which allows the testing of dry friction pairs. Rated friction pairs consisted of tool steel and a PA6 material.

Based on the results of experiments on five types of tool steels with polymer counterparts of PA6, we can conclude the following:

- After the evaluation of hardness tests, we can conclude that the tested tool steels are suitable for use in the manufacturing of molds.
- The largest mass removal of material was for 56NiCrMoV7 steel. The lowest mass removal of the material was for X38CrMoV5-1 steel.
- The highest friction coefficient was recorded for 56NiCrMoV7 and the lowest friction coefficient was recorded for X38CrMoV5-1.
- The largest change in surface roughening at evaluated parameters Ra, Rz was found in tool steels 90MnCrV8, 56NiCrMoV7 by friction PA6 plastic. Smaller changes at measured parameters Ra, Rz were evaluated in direction of S90 as in direction D0.

Based on the measured values, we can conclude, which tool steel is more suitable for the production of molds in combination with tested PA6 plastic. The most suitable was X38CrMoV5-1 tool steel.

From obtained results it can be stated that the decisive factor is the type, distribution and mutual bond of the structural constituent of materials and then the hardness of materials. The size of wear also is affected by the microroughness of contact surfaces and material combinations of friction pairs.

Acknowledgement

This project has received funding from the European Union's Horizon 2020 research and innovation programme under the Marie Skłodowska-Curie grant agreement No 734205-H2020-MSCA-RISE-2016.

References

[1] Stachowiak, S., Batchelor, A., Engineering Tribology (Third Edition), Elsevier Inc., Oxford, UK, 2006, ISBN 0-7506-7836-4

[2] Greškovič, F., Spišák, E., Materiály foriem na spracovanie plastov: Acta Metallurgica Slovaca. 2003, 9, 41-48.

[3] Greškovič, F., Dulebová, Ľ. and Varga, J., The applications of tool steels for different technologies of plastics processing. Materials Engineering. 2007, 14, (2), 77-80.
[4] Greškovič, F., Brezinová, J. and Guzanová, A., Tribological characteristics of selected materials of injection moulds shape filling blocks, PRO-TECH-MA '07. - Rzeszow: Politechnika Rzeszowska, 2007, p.20-25. ISBN 9788371994432
[5] Yamamoto T, Buckley, D.H., Wear Mechanism Based on Adhesion, NASA Technical Paper 2037. Cleveland: NASA; 1982.
[6] Hutchings, Ian M., Tribology, friction and wear of engineering materials. London: Edward Arnold. 1992. ISBN 034056184X 9780340561843.
[7] Rabinowicz, E., Friction and Wear of Materials. New York, 1995, 336 p., ISBN 978-0471830849
[8] Franklin, S.E., Wear experiments with selected engineering polymers and polymer composites under dry reciprocating sliding conditions. Wear. 2001, 251, 1591–1598.

Ján Varga[1], Ľudmila Dulebová[1], Janusz W. Sikora [2]

THE APPLICATION OF CAM SYSTEM AS A TOOL IN THE PRODUCTION OF EXTRUDER PART

Abstract: *Polymer extrusion is usually a complex process, particularly due to the process parameters. The paper deals with selection of appropriate strategies, available in CAM systems and applicable for extruder parts are produced. One of the most important factors for surface quality is milling strategy. A method to obtain required quality of the surface is proposed machined by proper strategies. As CAM system SolidCAM and CATIA were used, where lathe and milling operations were programmed. For production of extruder parts DMG machines were used. The aim was to apply this CAM system to the manufacturing process in the production of individual parts for the extruder.*
Keywords*: CAM system, tool path, CNC programming, milling strategies*

1. Introduction

Polymer extrusion is usually involved in the final production of many polymer products such as pipes, films, sheets, tubes, rods, etc. It is also an intermediate processing stage in injection moulded, blown film, thermoformed, and blow moulded products. An extruder is a machine which processes material by conveying it along a screw and forcing it through a die at a certain pressure [1].

The design of complex geometry products, as well as new technology challenges, has accelerated the rapid development of powerful computer aided design (CAD) software [2]. However the milling technology is not a primary manufacturing technology of parts, because use of sheet metal, plastic and casted and forged parts, the production of manufacturing equipments, like die and moulds etc., are required the milling technology [3].

The usage of CAD/CAM is the most effective solution for the implementation of technological preparation of production of complex shaped parts. In general, this sequence of creation of CNC programs is realized by the following steps [4, 5].

[1)] *Department of Engineering Technologies and Materials, Faculty of Mechanical Engineering, Technical University of Kosice, Masiarska 74, 040 01 Kosice, Slovakia, jan.varga@tuke.sk, ludmila.dulebova@tuke.sk*

[3)] *Department of Technology and Polymer Processing Lublin University of Technology, ul. Nadbystrzycka 36, 20-618 Lublin, Poland, j.sikora@pollub.pl*

For practical application of CAD/CAM systems is characteristic constructing of virtual 3D models, as it can see in the authors research [6], of parts which are designed in CAD (Computer Aided Design) system.

Today's trend component is machining in one setup, with minimal clamping. This is achieved by the time reduction of the final machining, while eliminating inaccuracies caused by manual switching of the part [7]. Universal application of computer aided systems brings significant benefits. CAM is most closely associated with functions in manufacturing engineering, such as process planning and numerical control (CNC) part programming [8, 9].

CAD/CAM systems permit significant improvements in milling and tuning operations, which can be reflected in reduced machining time and minor finishing operations. However, CAD/CAM operators must be very skilled professionals and the milling process depends strongly on the ability of these professionals. On the appropriate manipulation of a CAD/CAM system relies much of the success of the machining procedure [10].

Milling is a versatile cutting process used extensively in the machining of complex geometrical workpieces. It has become key technology in the manufacturing of dies and molds as well as in aerospace and automotive components. Therefore, a precise knowledge of the cutting process is required for the efficient definition of the machining operation [11]. A machining strategy establishes the working mode for a cutting tool in a machining operation and basically fixes the width and depth of cut, and the cutting trajectories. An in-depth knowledge of the cutting tool performance is applied in each individual case. Owing to this, it is the tool manufacturers who propose the use of machining strategies for an efficient use of their cutting tools.

Some papers refer to machining strategies in milling but only from the point of view of the definition of tool path strategies in order to improve the quality of the machined surface. Zhang [12], Ramos [11] and Toh [13] are some examples of research in this area.

The study of milling strategies is an important aspect when there is a necessity to identify the adequate machining strategy for a surface that has inherent geometry characteristics. This topic is even more important when the objectives are to lower surface roughness and minimise machining costs. A suitable machining strategy can lower significantly man labour as well as time and costs.

Polymer extrusion is usually involved in the final production of many polymer products such as pipes, films, sheets, tubes, rods, etc. It is also an intermediate processing stage in injection moulded, blown film, thermoformed, and blow moulded products. An extruder is a machine which processes material by conveying it along a screw and forcing it through a die at a certain pressure.

3. Parts production

This article describes the manufacture process of the four parts chain weel, barrel and body segment that are part of the extruder. Some simple shapes of parts were programmed directly on the machine in control system Sinumerik, but for complex shapes CAM system SolidCAM, or CATIA were used. The machining of parts was carried out on the following's machines:

- DMG MORI ECOMILL 50: 5 axis CNC milling machine (Fig.1) with control system Siemens 840D, working range X, Y, Z: 500 x 450 x 400 mm, working axis B: 5 / + 110 °, working axis C: 360 °, workpiece weight 200 kg.

Fig. 1. 5 axis CNC milling machine

- DMG MORI ECOTURN 510 CNC turning milling center (Fig.2) with control system Siemens 840D, max. workpiece diameter: ø465 mm, max. workpiece length : 1050 mm, max. workpiece weight : 1200 kg, positioning accuracy X / Z: 8/8 µm, number of driven tools: 6.

Fig. 2. CNC turning milling center

- Wire cutting machine Accutech AU 500l (Fig.3) with program Accutex 500, table travel in X and Y axes: 750 x 450mm, Z axis travel: 300 mm, max. cutting angle : 22.5 °, max. workpiece size: 990 x 560 x 265 mm, max. workpiece weight: 400 kg.

Fig. 3. Wire cutting machine Accutech AU 500l

3.1 Production of the Barrel part

The material of this part was 18 G2A (1.0562) It is a high strength alloy steel, which is good weldable and its used mostly for building structures, bridges, nets and bars to reinforce concrete, for pressurized tanks and pipes. 3D CAD model in Solidworks of the segment Barrel is shown in Fig.4.

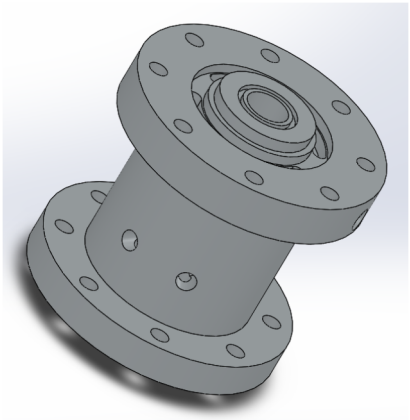

Fig. 4. CAD model of Barrel in Solidworks

To produce of the segment of Barrel three clamping positions were used. For the programming the CAM system SolidCAM was used.

- The first clamping - turning milling center

The manufacturing process of the Barrel part is nearly describing in following steps:

1. Face turning finishing Fig.5a., tool Sandvik DCLNL 2525M 12
2. Turning cylindrical face
3. Grooving tool Fig.5b, TGSU 35 6 IQ ISCAR, tool width 6,3 mm
4. Central hole Fig.5c, drilling tool diameter 20 mm

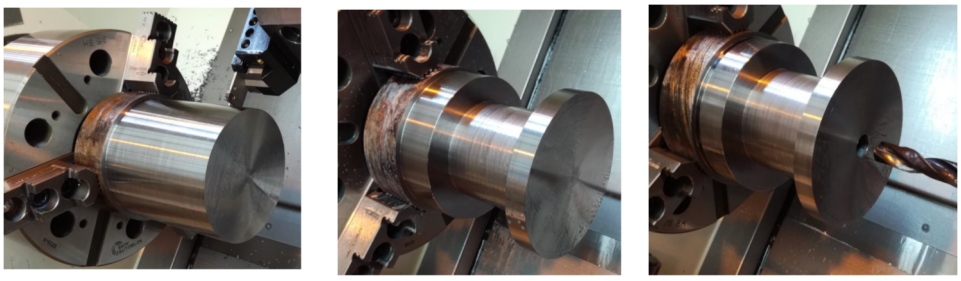

a) *b)* *c)*

Fig. 5. Part after turning cylindrical face (a), Grooving operation (b), Central hole (c)

After drilling of central hole followed holes drilling 8 x diameter 8 mm on the first face surface (Fig.6a) and the holes with diameter 8,5 mm on the second face surface Fig.6c. Guide holes (Fig.6b) from the previous operation were used to drill the second holes.

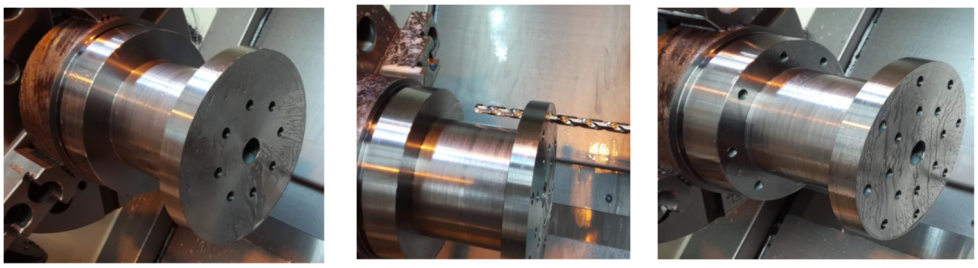

a) *b)* *c)*

Fig. 6. Guide holes drilling (a), Drilling through guide holes (b), Final holes (c)

After holes circle groove milling (Fig.7a) was created and then followed the milling of three pockets Fig.7b. At the end threads M10 (Fig.7c) were created.

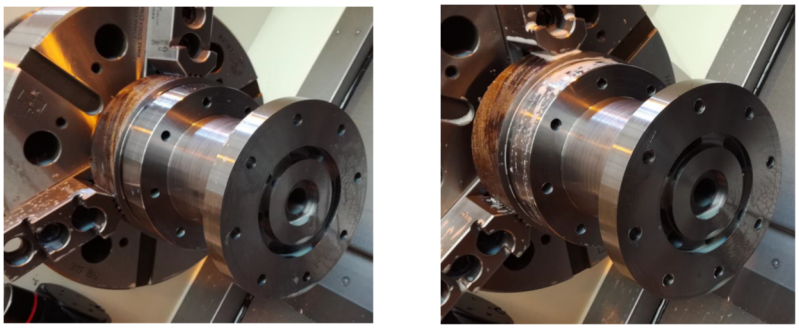

a) *b)*

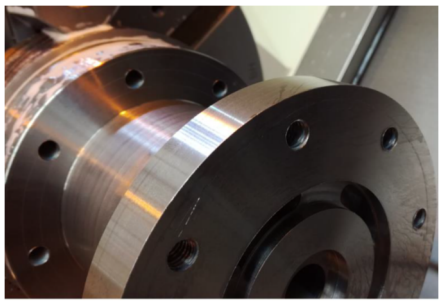

c)

Fig.7. Circle groove milling (a), Pockets milling (b), Threads M10 (c)

In this first clamping on the turning milling center was created the last operations as radial holes drilling (Fig.8a) and threads 2 x G ¼ and radial hole drilling (Fig.8b) with thread M 12x1.

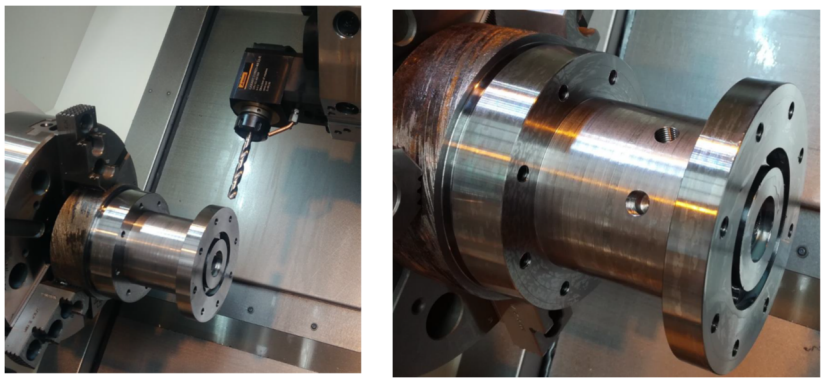

a) *b)*

Fig. 8. Radial holes drilling (a), Threads creation (b)

- The second clamping – 5 axis CNC milling machine

For this clamping (Fig.9a) the rotate table was used. The manufacturing process from the second clamping describe following steps:

1. Face milling (Fig.9a), tool diameter 63 mm
2. Slot roughing, tool diameter 20 mm
3. Face finishing , tool monolit diameter 16 mm
4. Drilling holes (Fig.9b), diameter 11 mm
5. Circular groove (Fig.10a), to 6 mm depth, tool monolit diameter 5 mm
6. Groove width 3 mm milling, tool monolit diameter 5 mm

a) *b)*

Fig. 9. Part clamping (a), Face milling (b)

After pockets milling (Fig.10a) were holes drilling 8 x Ø 8mm. Followed the rotation to required angle radial holes drilling (Fig.10b) and thread ½ 20 UNF.

a) *b)*

Fig. 10. Part after circular groove (a), pockets milling (b)

- The third clamping – 5 axis CNC milling machine

We had to use a wire cutting machine to get a hole with the required size. A method of clamping the part (Fig.11a) and hole cutting process is shown in Fig.11b.

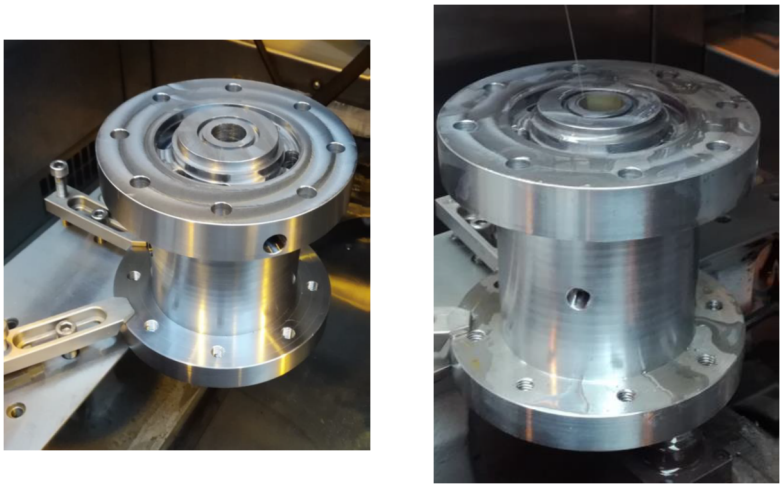

a) *b)*

Fig. 11. Part clamping on wire machine (a), Hole cutting (b)

The final shape of the part with the required dimension after third clamping is shown in Fig.12.

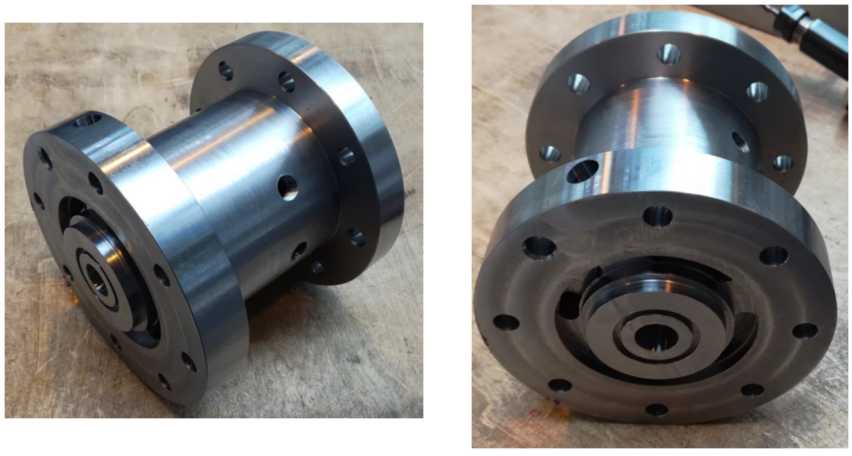

Fig. 12. Final shape of the part of Barrel

3.2 Production of the Body part

The material of this part was 40HM (1.7225). It is CrMo-alloyed steel, engineering steel supplied in hardened and tempered conditions with a good machinability. Its used for components with high requirements on toughness, e.g. gear wheels, pinions, connecting rods, and parts for mechanical engineering. The first side of CAD model in Solidworks (Fig.13a) and the second side of the Body segment is shown in Fig.13b.

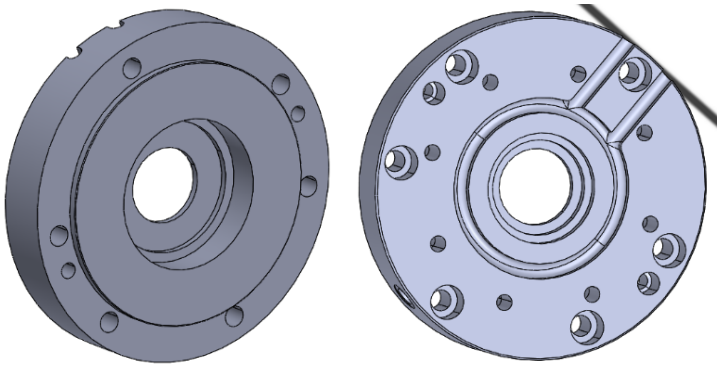

a) *b)*

Fig. 13. First side of CAD model (a), Second side of CAD model (b)

For produce of this segment CAM system CATIA and 5-axis CNC milling machine was used. We used two clamping positions on different machines. Clamping method is shown in Fig.14.

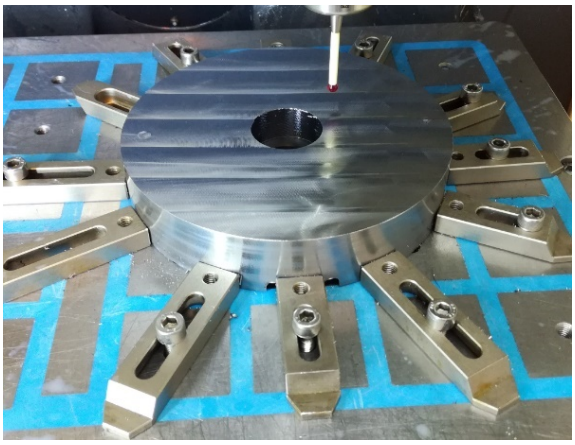

Fig. 14. Clamping method of the part

Tool path of the tool was generated in CAM system CATIA. At the top of the surface zero point was define and were selected necessary of the tools for the milling of the part. Milling of the outside contour (Fig.15a) and the inside circle pocket shows Fig.15b.

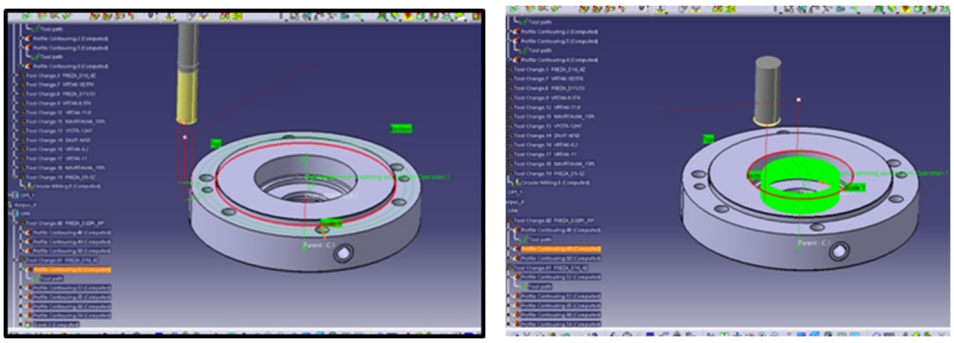

a) *b)*

Fig. 15. Outside milling contour (a), Inside circle pocket milling (b)

The manufacturing process of the part named Body is nearly describing in following steps:

1. Slot roughing, Tool monolit diameter Ø 5mm
2. Slot semifinish, Tool monolit diameter Ø 4mm
3. Slot finish, Tool ball nose monolit diameter Ø 4mm
4. Pockets milling, Tool monolit diameter Ø 16mm
5. Chamfers of pockets
6. Holes drilling, Tool drill diameter Ø 8,5 mm
7. Chamfers
8. Threads M10
9. Holes drilling, Tool drill diameter Ø 6,8 mm
10. Chamfers
11. Threads 5 x M8
12. Radial hole and thread M12 x 1

Obtained shape of the part after milling from the first side (Fig.16) and the final shape form the second side is shown in Fig.17.

Fig. 16. The shape of the Body after milling from the first side

Fig. 17. The final shape of the body part

3.3 Production of the Chain weel part

The material of this part was 18 G2A (1.0562). It is a high strength alloy steel, which is good weldable and its used mostly for building structures, bridges, nets and bars to reinforce concrete, for pressurized tanks and pipes. 3D CAD model in Solidworks of the chain weel is shown in Fig.18.

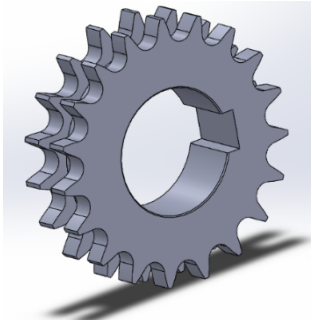

Fig. 18. CAD model of chain weel product

The manufacturing process of a chain weel consists of two clamping position on different machines. In the first position turning milling center and for the second position wire cutting machine was used.

- The first clamping - turning milling center

Sides milling on CNC turning milling center (Fig.19a) for better clamping to other operation on wire cutting machine is shown in Fig.19b.

a) b)

Fig. 19. Three jaws clamping (a), part ready for the clamping to next operation (b)

- The second clamping - Wire cutting machine

Wire cutting machine includes a program Accutex 500 and for cutting was used wire thickness 0,25 mm. During production were left on the sides a little bridge to secure the position of the part. For a start the first half of the part was made and then the 2nd half. The bridges were removed at the end of the process. The internal dimension diameter 50 mm was produced gradually. We used three sections to define the required dimension - 1st diameter 49,90 mm. We left allowance 0,1 mm, 2nd section - dimension diameter 50 mm and the last - diameter 50,02 mm. Followings pictures describes nearly a manufacturing process. Part clamping (Fig.20a) and the production of the inside shape on wire cutting machine describes Fig.20b.

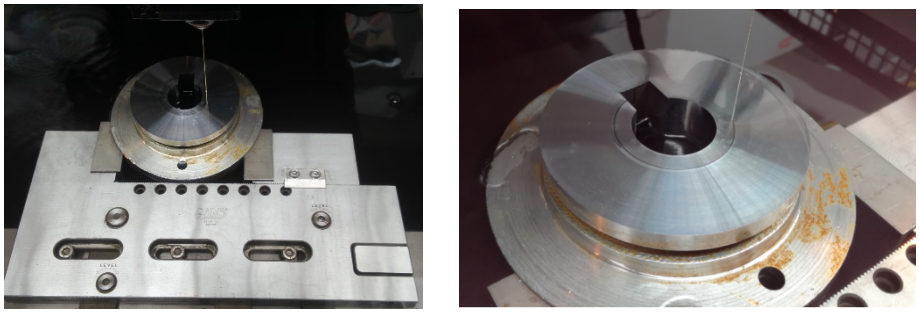

a) b)

Fig. 20. Chain weel clamping (a), shape cutting (b)

Gearing shape production – The first half of gearing shape production (Fig.21a) and the toolpath of cutting wire in cutting process is shown in Fig. 21b.

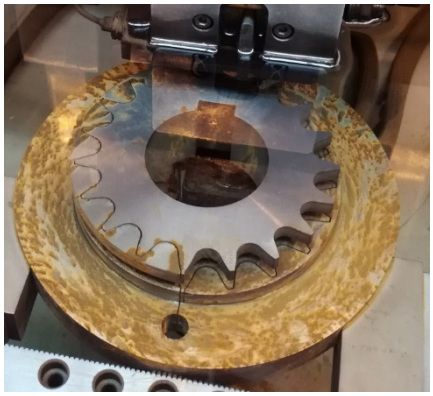

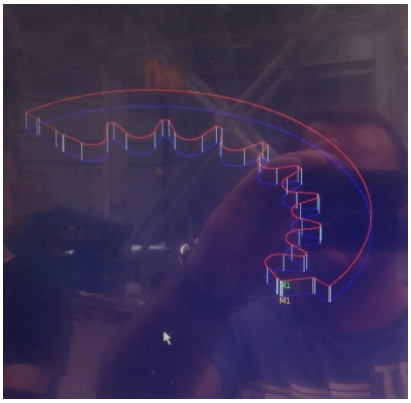

a) *b)*

Fig. 21. Gearing shape production - first half (a), Toolpath of cutting wire (b)

After the first half of the gearing shape, the second half production (Fig.22a) was cut out. The final shape after cutting is shown in Fig.22b.

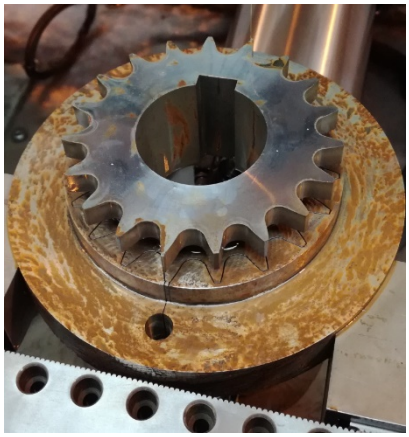

a) *b)*

Fig. 22. Gearing shape production – second half (a), Final shape of chain weel (b)

3.4 Production of the Top and bottom plate part

The material of this parts was 40HM (1.7225). It is CrMo alloyed steel, engineering steel supplied in hardened and tempered conditions. Components from this material have high requirements on toughness, e.g. gear wheels, connecting rods and parts for mechanical engineering. 3D CAD model in Solidworks of the top plate (Fig.23a) and bottom plate is shown in Fig.23b.

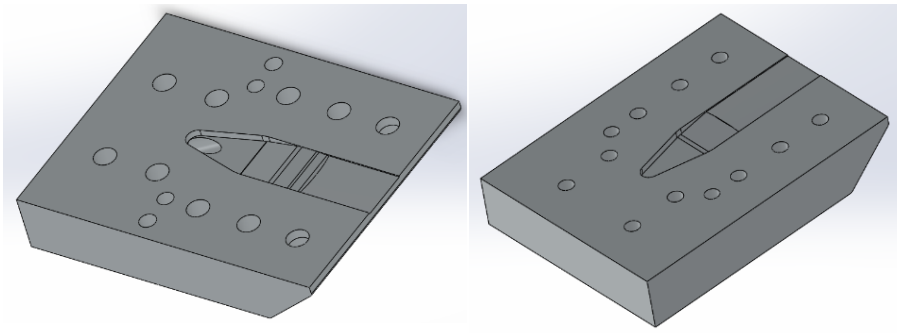

a) *b)*

Fig. 23. 3D model of top plate (a), 3D model of bottom plate (b)

Top and bottom plate were made by 5 axis milling machine. The manufacturing process of the parts is describing in following steps:

1. Milling outside contour, wall allowance 0,2 mm
2. Holes and threads 4x M6, 2x M10, M12x1
3. Process of hardening HRC 32
4. Flat surface grinding
5. Finishing outside contour on finally dimensions
6. Shape milling Ø 8 mm
7. Finishing flatness surfaces Ø 2 mm
8. Finishing edges and rest surfaces, ball nose Ø 1 mm
9. Rotation to required angle 30° - milling D 5 mm and holes drilling
10. Finishing holes - Ø 8H7

Before produce of the parts some simulations in CAM system CATIA were made. Some pictures from simulations is shown in Fig. 24.

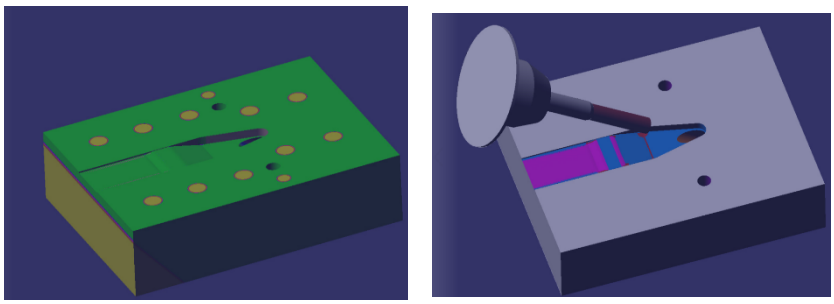

Fig. 24. Simulation of the parts

The same technological process was made also for the bottom plate, where is not angle defined hole and shaped surface. The final shapes of the plates show Fig. 25.

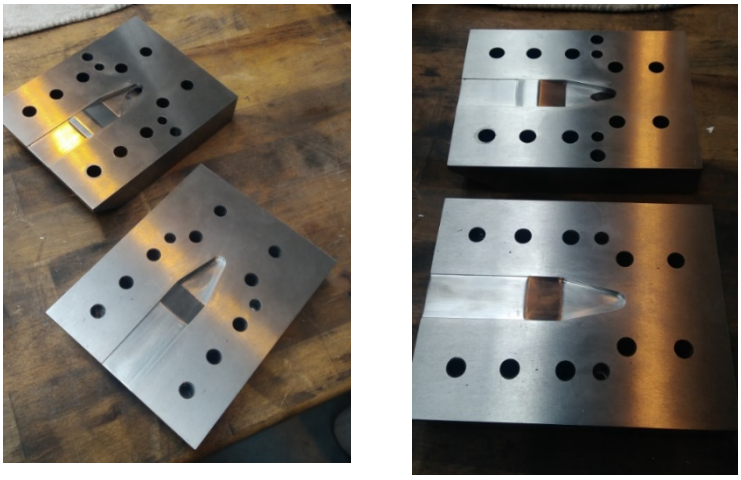

Fig. 25. Final shapes of the plates

4. Conclusion

The paper deals with the application of CAD/CAM systems in the production of four parts, which are part of the extruder. The main objective of the authors of this publication was practically implement CAD/CAM systems and optimize the production process of three parts from the beginning to their production. Various CNC machines were used in the production of these parts. In the production process, it was

necessary to consider the method of clamping individual parts, the choice of suitable strategies for milling, turning, the choice of suitable tools and cutting conditions the required material and shape. The programs creation was based on drawing documentation and CAD models. Some operations were programmed on the machine in control system Sinumerik and complex shaped surfaces in CAM systems CATIA and SolidCAM.

CAM systems are used for preparing data and creating CNC programs for manufacturing components. The result was finished parts that are part of the equipment, the extruder.

Acknowledgement

This project has received funding from the European Union's Horizon 2020 research and innovation programme under the Marie Skłodowska-Curie grant agreement No 734205-H2020-MSCA-RISE-2016.

References

[1] Parnaby, J., Kochhar, A.K., Wood, B., Development of computer control strategies for plastic extruders, 1975,15 (8), 594-605.
[2] Ramos, A.M., Relvas, C., Simoes, J.A., The influence of finishing milling strategies on texture, roughness and dimensional deviations on the machining of complex surfaces, Journal of Materials Processing Technology, 2003,136 (1-3), 209-216.
[3] Balázs, M., Study of z-level finishing milling strategy; Development in machining technology – Scientific research research, 2012, 2, 1-8.
[4] Dubovska, R., The quality control of machining process with CAD/CAM systems support, Industrial Engineering, Tallin, Estonia, 2012, 27-32.
[5] Jambor, J. Majerik, J., Hard Die & Mould Milling Process with CAD/CAM System CATIA V5R18 Support, in: Annals of DAAAM for 2009 & Proceedings of the 20th International DAAAM Symposium, 2009, 20, 1465-1467.
[6] Yu, T., Zhang, X., Liang, W., W. Wang, W., A web based virtual system for turn milling center, International Journal of Advanced manufacturing Technology, 2013, 67, 2395-2407.
[7] Altintas, Y, Kersting, P., Biermann, D., Budak, E., Denkena, B., Lazoglu, I., Virtual process systems for part machining operations, in: CIRP Annals – Manufacturing Technology, 2014, 63, 585-605.
[8] Afazov, S.M., Modeling and simulation of manufacturing process chains, in: CIRP Journal of Manufacturing Science and Technology, 2013, 6, 70-77.

[9] Dubovska, R., Kvasnica, P., Kvasnica, I., Perspective of parallel simulation in mechatronic system – metal cutting, in: Advanced Materials Research, 2013, 705, 295-300.
[10] Ramos, A.M., Relvas, C., Simoes, J. A., The influence of finishing milling strategies on texture, roughness and dimensional deviations on the machining of complex surfaces. Journal of Materials Processing Technologies, 2003, 136, 209-216.
[11] Perez, H., Diez, E., Perez, J., Vizan, A., Analysis of machining strategies for peripheral milling, Procedia Engineering, 2013, 63, 573-581.
[12] Dang, J.W., Zhang, W.H., Yang, Y., Wan, M., Cutting force modelling for flat end milling including botton edge cutting effect. International Journal of Machine Tools and Manufacture, 2010, 50, 986-997.
[13] Toh, C.K., A study of the effects of cutter path strategies and orientations in milling. Journal of Materials Processing Technologies, 2004, 152, 346-356.

Ivan Gajdoš[1], Janusz Sikora[2], Emil Spišák[3] ,Karolina Glogowska[2]

MIXING PERFORMANCE ANALYSIS OF SINGLE SCREW EXTRUDER WITH ROTATIONAL BARREL SEGMENT

Abstract: Since the introduction of first single screw extruder (SSE) for thermoplastic polymer in 30thies of 20th-century basic motion kinematics remained the same. Newly introduced SSE construction element called rotational barrel segment (RBS), changes the kinematic of motion in SSE. Due to complexity of phenomena occurring in the melt flow during passing RBS area, a strong demand exists to evaluate the flow and mixing characteristic of RBS with means of full 3D CAE analysis. To evaluate the mixing performance of RBS, complex numerical techniques and approach must be applied. Presented paper describes techniques and modules involved in the ANSYS POLYFLOW® software that allows to evaluate the flow in the RBS including mixing performance.

1. INTRODUCTION

Since their massive development during 20th century, single screw extruders have undergone a continuous growth in all industrial fields, and they have become indispensable in plastic industry. Redesigning of the rotary working element (screw), new techniques for heating and cooling the plasticizing system were the main construction approaches of innovation and development. In 1998 R. Sikora and J.W. Sikora introduced, a completely new concept of the design of a single screw extruder (SSE). This new design was based on kinematic activation of the barrel itself, which meant it could rotate in the direction identical or opposite to the direction of rotation of the screw (fig.1). In this design concept, the barrel of plasticizing system consists of two fixed (stationary) parts and a movable part placed between them, adjoining the fixed parts with its end faces and placed inside an outer housing attached to both fixed parts. The movable part can rotate in accordance with or opposite to the motion of the screw; it is driven by an external motor and performs rotary motion independently of the motion of the screw. The rotary barrel segment (RBS) is preferably located in the central part of the plasticizing system.

Due to construction complexity of RBS and problems related to it, no practical application of RBS in SSE is currently available. To evaluate the

[1] *Technical University of Košice, Department of CAx Technologies, Mäsiarska 74, 040-01, Košice, Slovak Republic, e-mail: ivan.gajdos@tuke.sk*

[2] *Katedra Procesów Polimerowych, Wydział Mechaniczny, Politechnika Lubelska, ul. Nadbystrzycka 36, 20-618 Lublin.*

[3]*Technical University of Košice, Department of Technologies and Materials, Mäsiarska 74, 040-01, Košice, Slovak Republic*

functionality of the RBS concept a 3D FEM simulation of polymer melt flow was performed, as a part of tasks solved within NewEX project. Further investigation of mixing performance of RBS extruder are necessary and in this chapter concepts and models for evaluation of mixing are presented.

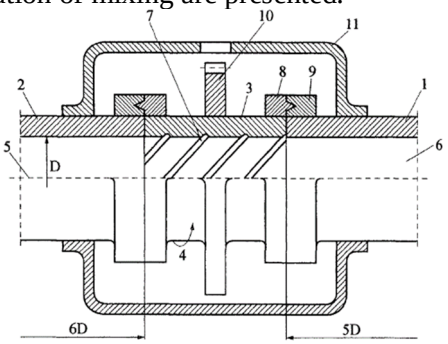

Fig.1 Rotary sleeve of the plasticizing system's barrel: 1, 2 - fixed parts of the barrel, 3 - rotary element, 4 - direction of rotation of the movable part of the barrel, 5 - screw axis, 6 - inner surface of the fixed part of the barrel, 7 - grooves, 8.9 - bearings, 10 - gear drive, 11 -external housing

2. CHARACTERIZATION OF MIXING PROCESS

First attempts to define the process of mixing were by Dankwertz in the 1950s. Dankwertz analyzed the mixing as a homogenization process of a concentration field. If initially, two different fluids are separated in adjacent zones by a barrier and the barrier is then removed, as time passes, the local concentration of each fluid disperses everywhere within the fluid. With perfect mixing, the concentration tends to the same value everywhere in the fluid domain. Dankwertz defined two values to evaluate homogenization process, the segregation scale and the intensity of segregation. In the 1980s, Ottino defined other parameters based on the Continuum Mechanics Theory. He defined the mixing process as a action that increases the interface that exists between fluids. To quantify the mixing process Ottino proposed to measure the local increase of infinitesimal surfaces distributed everywhere in the flow domain.

This approach is not applicable when analyzing the distribution of small amounts of pigments, tracers, and so on, in the flow domain (small percentage of the volume of the total flow domain). Manas-Zloczower, defined a new parameter **δ**, in order to quantify the mixing process. Initial idea starts with placing a set of particles in a small zone of the flow domain and with time these particles move in the flow and distribute throughout the flow domain. With the parameter **δ**, is possible to measure the deviation of the actual distribution with respect to a ideal distribution of particles in the flow domain. Another technique divides flow domain into a set of adjacent (and non-overlapping) zones. At the start of the calculation, a set of particles is placed in a small volume in the flow domain and

they are moving in flow domain over the time. At defined time-steps, the number of points in each volume are counted. If each volume contains a number of points proportional to its surface/volume, then there is good distributive mixing. Last option to estimate distributive mixing, is to calculate the local points concentration in various locations of the flow domain and compare these concentrations with a perfect points concentration. Parameter $\boldsymbol{\delta_p}$, quantifies the deviation in points concentration.

Dispersive mixing is another important phenomenon occurring in the mixing process, and is very important that dispersive mixing occurs in SSE during processing of composites. Dispersive mixing is characterized by the break-up of drops into small droplets or the disagglomeration of solid particles in a matrix. The stress acting on the drops or on the solid particles by the matrix is the mechanism that can lead to dispersion. If the stresses are high enough to compete with the surface tension of drops or with internal mechanical resistance of solid particles, dispersion occurs. Dispersion is mainly possible in the elongational flow.

In the process of composites processing in SSE, a minor component is generally called as filler (drops) in a continuous phase of matrix (major component). Mixing is a process of deformation and break-up of the drops and simultaneously distribution of those drops in matrix. Good mixing is process that results in small and identical drops distributed evenly throughout volume of matrix. In general, mixing begins with a distributive step (drops are deformed passively), followed by a dispersive step (drops break up into droplets), and finally by the distribution of the droplets in the flow.

In general, mixing begins with a distributive step (drops are relocated within the flow domain and eventually stretched), followed by a dispersive step (drops break up into droplets), and finally by the distribution of the droplets in the matrix.

2.1 Kinematic parameters of mixing

One solution to quantify mixing is to specify the capacity of the flow to deform matter and to generate interface. Let's assume that interfacial forces are neglected and no break-up into droplets can occur. For 2D flows, the interface between fluids is a line. Instead of calculating the evolution of this interface (a very complex and impossible task to perform because of the exponential growth of the interface), the stretching of infinitesimal vectors attached to a large number of material points distributed in all the flow domain is calculated. As the points move in the flow domain, the vectors are stretched. The stretching and the rate of stretching of these vectors are properties that vary by time and location in the polymer melt matrix. Statistical evaluation of the data enables a global overview of the mixing process. Using this method, you have an objective and quantitative

evaluation of the mixing of melted composites. It is possible, find areas of insufficient mixing in the domain (low stretching instead of exponential increase). For 3D flows, the interface is a surface and the stretching of infinitesimal surfaces attached to material points is calculated.

If flow domain of homogenous fluid is marked as $\boldsymbol{\Omega_0}$ and $\boldsymbol{\Omega}$ at time $\mathbf{t_0}$=0 and time **t**, we can describe the motion of the fluid by the function:

$$\boldsymbol{x} = x(\boldsymbol{X}, t) \tag{1}$$

where **X** is the position of the material point **P** in $\boldsymbol{\Omega_0}$ and **x** in $\boldsymbol{\Omega}$. The symbols **F** and **C** denote the deformation gradient and the right Cauchy Green strain tensor between both configurations.

In case of calculating mixing in 3D flow, we can define the local stretching of infinitesimal surfaces utilizing $\boldsymbol{\eta}$ – area stretch. In the initial state $\boldsymbol{\Omega_0}$ time $\mathbf{t_0}$=0, consider an infinitesimal surface **dA** with a normal direction $\widehat{\mathbf{N}}$ deforming over the time. At the time **t**, the surface is noted **da**, with vector of normal direction $\hat{\mathbf{n}}$. The area stretch $\boldsymbol{\eta}$ is then defined as the ration of the deformed surface **da** at time **t** over the initial surface **dA**:

$$\eta = \eta\left(\boldsymbol{X}, \widehat{\mathbf{N}}, \mathrm{t}\right) = \frac{da}{dA} \tag{2}$$

A good mining quality (considering incompressible fluid) requires high values of $\boldsymbol{\eta}$ throughout time and space. A local evaluation of the efficiency of mixing is determined by ratio:

$$e_\eta\left(\boldsymbol{X}, \widehat{\mathbf{N}}, \mathrm{t}\right) = \frac{\dot{\eta}/\eta}{D} \tag{3}$$

2.2 Distribution index

At the beginning we start with cluster of particles concentrated in a small box (fig.2). It is assumed that the particles do not affect the flow field and that there is no interaction between them. Particles are distributed over the flow domain as a function of time. Distribution index $\boldsymbol{\delta}$ defined by Manas-Zloczower enables to quantify the process of particles distribution.

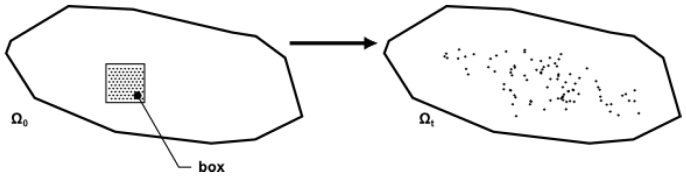

Fig.2 Distributing particles over the flow domain

To determine the distribution index $\boldsymbol{\delta}$ we start with assumption of **N** points distributed over the flow domain at time **t**, with know position **x**. We can evaluate for each pair of points $\mathbf{x_i}$ and $\mathbf{x_j}$ their mutual distance $\mathbf{d_{ij}} = \|\mathbf{x_i}\text{-}\mathbf{x_j}\|$. In the flow domain, there are **N(N-1)/2** pairs of points. Maximum observed distance is the diameter of the flow domain.

Another option is to evaluate distance $\mathbf{d_{ij}} = ||\mathbf{x_i}-\mathbf{x_j}||$ between each point $\mathbf{x_i}$ and his closest neighbor $\mathbf{x_j}$, so totally we have **N** values of distance. This option of distance calculation helps to better discriminate distributive capacities of similar mixing sections.

When the amount of distances in known, it is possible to calculate the density of probability function on the distance **f**(d): the probability to find two randomly selected points with mutual distance in range [**d**,**d**+**Δd**] at time **t** is: **f**(d)Δd (fig.3).

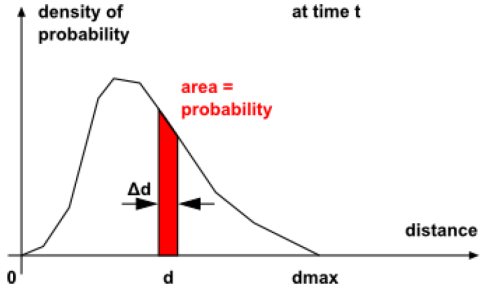

Fig.3 Density function probability over distance

Ideal distribution of the points over the flow domain is determined by the optimal distribution function $\mathbf{f_{opt}}$(d) (fig.4), calculated in the same way as **f**(d). The distribution index **δ** is defined as the deviation of the function **f**(d) (real distribution) from the optimal distribution $\mathbf{f_{opt}}$(d):

$$\delta(t) = \frac{1}{2}\int_0^{+\infty} |f(l) - f_{opt}(l)| dl\,, \quad \delta \in [0,1] \tag{4}$$

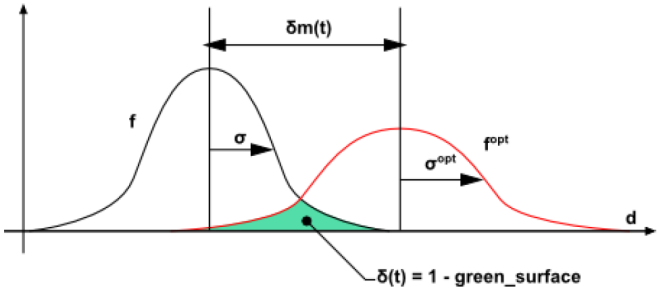

Fig.4 Comparison of density function probability for real and optimal distribution.

As the distribution improves, the index **δ** decreases. This index is dimensionless, that means it is independent of the size of the flow domain. The evolution of **δ** depends on the initial position of the box and the number or material points to distribute. When evaluating the mixing capabilities of mixer, analysis must be done to measure its influence. The difference of the means for real and optimal distribution $\boldsymbol{\delta_m(t)}$is defined:

$$\delta_m(t) = \bar{d} - \bar{d}^{opt} \quad where\ \bar{d} = \int_0^{\infty} df(l)dl \tag{5}$$

2.3 Particle distribution in zones

The distribution index is used to quantify distributive mixing. Applying this approach, it is possible to detect zones in the flow domain where material points are missing, and where there is an excess of points. As for the distribution index, there is a cluster of particles initially concentrated in a small box (fig.2). It is assumed that the particles do not affect the flow field and that there is no interaction between them.

Over the time, polymer flow distributes the set of points across the domain and the domain is split into coherent zones (fig.5).

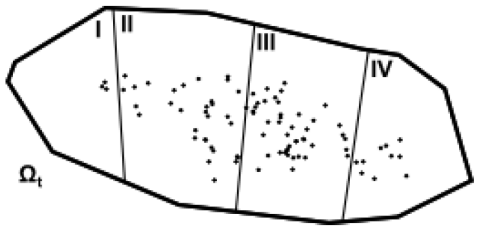

Fig.5 Flow domain divided into four coherent zones.

The same number of points **N** is then optimally placed throughout the flow domain. Then the number of points in each zone is determined, for both distributions at time. Then the relative error of distribution **Z** for each zone is defined by:

$$\varepsilon(Z) = \frac{nbr(Z) - nbo(Z)}{N} \tag{6}$$

where **nbr** number of points of the real distribution appearing in zone **Z**, at time **t**, and **nbo** is the number of points in zone **Z** in case of the optimal distribution in the same zone.

If **ε** is zero for a zone, the optimal number of points are in that zone.

If **ε** is negative for a zone, there is a lack of points in that zone as compared to the optimum.

If **ε** is positive for a zone, there are too many points in that zone as compared to the optimum.

A global index based on all the zones is defined as:

$$\varepsilon_g = \frac{1}{2}\sum_{z=1}^{\#\,zones} |\varepsilon(z)| \tag{7}$$

The number of generated points and the number of zones influences the final result for ε_g calculation. When comparing two SSE, it is recommended that to keep the ratio number of points and zones constant. In order to have relevant results, this ratio should be higher than 100.

2.4 Points concentration deviation

When evaluating distributive mixing by calculating distribution index, the computation of perfect points distribution is necessary. To eliminate this calculation of deviation for points concertation is another available method. As in the case when calculating distribution index or relative error of distribution, there is are particles placed in box at time t=0 (fig.6). The points are over the time distributed in the flow domain.

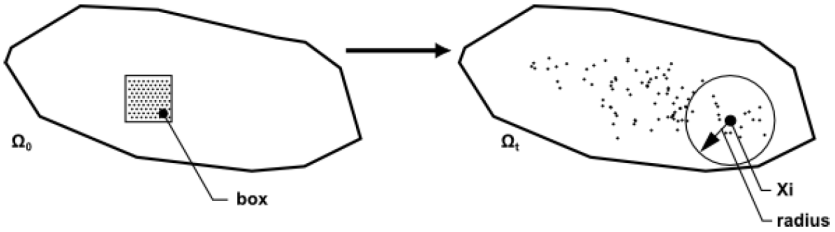

Fig.6 Initial placement of the point in box and detection zone in perimeter of point x_i

For each point $\mathbf{x_i}$, the number of neighbors $\mathbf{x_j}$, within a sample radius **r** is determined. When calculating the mixing in 3D flow domain the local points concertation is $\mathbf{\Phi(x_i)}$ is defined as:

$$\Phi(x_i) = N_x / \left(\frac{4}{3}\,\pi.r^3\right) \tag{8}$$

where $\mathbf{N_x}$ is the number of points of the cluster around xi at a distance smaller than the radius **r**. With a perfect distribution of the points, the points are equally distributed throughout the entire flow domain. That is, there are the same number of points per unit volume found everywhere in the domain. The perfect points concentration $\mathbf{\Phi_p}$, corresponds to the number of points divided by the volume of the flow domain.

Points concertation deviation $\mathbf{\delta_p}$ at time **t** is defined as:

$$\delta_p(t) = \sqrt{\frac{\sum_{i=1}^{N}\left[\Phi(x_i)-\Phi_p\right]^2}{N}} \tag{9}$$

Where **N** is the number of points in the cluster at time **t**. $\mathbf{x_i}$ correspond to the location of point **i** at time **t** and $\mathbf{\Phi_p}$ is the perfect points concentration.

The points concentration is only evaluated at positions where there are points. There is no points concentration evaluation in zones of the mixer that do not contain material points. If distributive mixing improves, the points concentration deviation should decrease. At perfect distribution, the same points concentration is found at any location in the cluster, and the deviation $\mathbf{\delta}$ equals zero.

2.6 Drops disagglomeration

Study of the dispersive mixing of solid particles in a fluid matrix was done by Alsteens, by studying the evolution of the size of the agglomerates. A set of agglomerates of different sizes is placed at the start of mixing in flow domain. If the volume of the flow domain smaller representative volumes $\mathbf{V_x}$, each representative volume contains agglomerates of different sizes (fig.7 left).

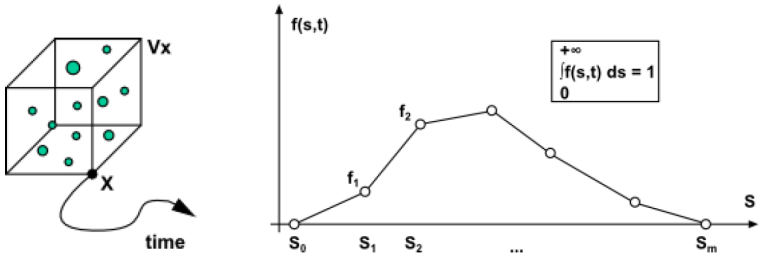

Fig.7 Representative volume with agglomerates and discretized mass density function

If the number of agglomerates is large enough in volume $\mathbf{V_x}$, this distribution of agglomerates sizes can be summarized in a mass density function **f(s,t)**, where **t** is the time and **s** is the size (mean diameter) of the agglomerate μm^{-1}. The mas fraction of agglomerates of size in interval $[S_a,S_b]$ is: $\int_{S_b}^{S_a} f(s)ds$.

This mass fraction distribution changes with time, as the volume $\mathbf{V_x}$ attached to the point **X** moves in the mixer, because of erosion and rupture taking place during mixing. It is assumed that there is no transfer of agglomerates between adjacent volumes, due to the high viscosity of the matrix.

Erosion is a slow and continuous process observed for all admissible sizes of agglomerates (fig.8). This process generates a lot of small particles. Rupture occurs when a critical stress is reached and is observed for large particles. This process generates two or more agglomerates.

Erosion and rupture depend on the size of agglomerates, the shear rate and the shear stress. We can distinguish between the two types of solid particles: the aggregates and the agglomerates. Aggregates are the smallest particles that cannot be eroded or broken anymore. Agglomerates are larger particles formed of several aggregates linked together by cohesive forces.

rupture process erosion process

Fig. 8 Types of processes during disagglomeration

2.6.1 Erosion

Presented model of erosion is based on the work of Collin and Peuvrel-Disdier, where dispersive mixing of carbon black agglomerates in SBR matrix was described.

During erosion, small particles are removed continuously from the agglomerates, which diminish in size. This removal can occur if the shear stress **σ** is above a given threshold $\boldsymbol{\sigma_{critE}}$. In this case, is assumed that the agglomerates are spherical shaped and the variation of size **Δs** , of the agglomerate after **Δt** seconds can be defined:

$$\frac{\Delta s}{\Delta t} = -\frac{8\alpha(\sigma-\sigma_{critE})\dot{\gamma}}{3S^2} \tag{10}$$

Where α is a coefficient of proportionality, $\dot{\gamma}$ is the local shear rate, **S** is the size of the agglomerate at time **t**, and **S+ΔS** is the new size of agglomerate at time **t+Δt**. Based on the assumption of the mass conservation, the mass distribution function is:

$$f(s+\Delta s, t+\Delta t) = \frac{(s+\Delta s)^3}{s^3} f(s,t) \tag{11}$$

As the total mass of solid particles is constant in the control volume $\mathbf{V_x}$, when the mass fraction of agglomerates decreases, the mass fraction of aggregates increases. Effect of erosion on the mass distribution of agglomerates is presented in figure 9. Initial size of agglomerates was between 15 and 25 microns. They were mixed in a matrix with a viscosity of 11000 [Pa.s] at a constant shear rate of 10 s^{-1}. The mass distribution function is plotted for the initial, state then after 25 and 50 seconds.

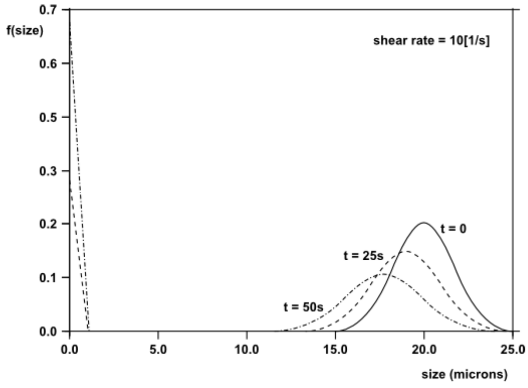

Fig. 9 Graph for agglomerates mass distribution affected by erosion over time

The shift to left and the widening and flattening of the Gaussian curve centered initially at 20 microns demonstrates erosion of agglomerates and at the same time the increasing peak at the extreme left of the graph, in the small sizes, which corresponds to the generation of aggregates.

2.6.2 Rupture

Model of rupture presented by Collin and Peuvrel-Disdier, assumes that an agglomerate breaks-up into segments if a shear stress higher than a critical shear stress $\boldsymbol{\sigma_{critR}}$ is acting on the agglomerate. Moreover, the sear stress should act on the agglomerate over a given time period (rupture time). The critical shear stress for the rupture as a function of agglomerate size **S**, can be defined:

$$\sigma_{critR}(S) = \sigma_{min} + \frac{\beta}{S} \tag{12}$$

The function (12) in the inverse form allows to calculate critical size of agglomerates $\mathbf{S_c}$ that will break at a given shear stress $\boldsymbol{\sigma}$:

$$S_c = \frac{\beta}{(\sigma - \sigma_{min})} \tag{13}$$

This model assumes that the rupture time is a constant, and that only a fraction of all particles of a given size will break if rupture criteria are met. It is clear that not all particles of a given size have the same internal cohesion and the model allows to specify the rupture rate (the fraction of particles that break when rupture criteria are met) during calculation.

To calculate and present how a set of agglomerates of size **S** will break in numerous fragments of various sizes, it is assumed that the volumes of the fragments follow a Gaussian distribution between 0 and the parent agglomerate volume. On average, the parent agglomerates (of size **S**) are cut into two fragments of equal volume, leading to a mean size of 0.8. The transfer function for rupture is shown in the following figure 10, with a rupture rate of 1.

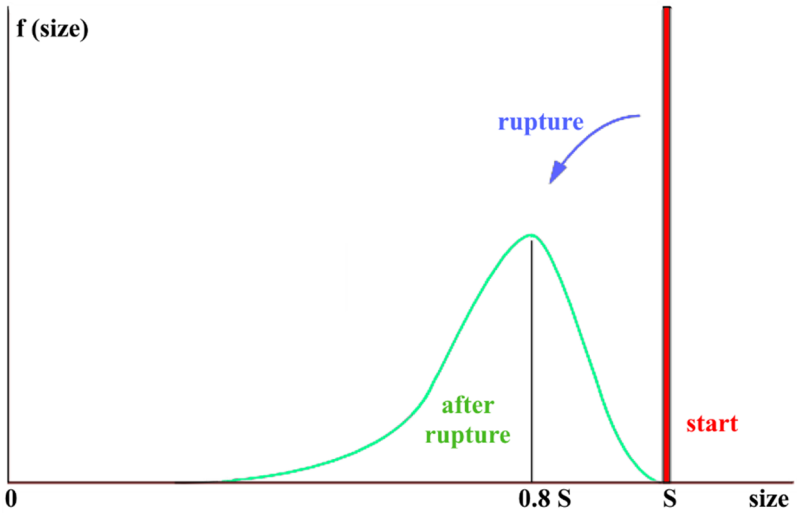

Fig. 10 Transfer function for rupture

3. Mixing task in POLYFLOW

Calculation of mixing task in POLYFLOW consist generally from three major steps: calculating the flow, calculating a set of the trajectories and statistical analysis of the results. This is a general approach, but is also applicable to perform mixing analysis in SSE on 3D model (mesh).

3.1 Flow simulation

Flow simulation of SSE with RBS has been calculated by Gajdoš, utilizing Mesh Superposition Technique (MST). Calculating of polymer melt flow starts either with appropriate CAD model of flow domain and SSE elements or the model of flow domain and SSE element is created in mesh pre-processing tools like ICEM, GAMBIT etc. These models are subsequently meshed, following the general rules for preparing mesh for CFD simulation, taking into account the solution of the problem by the MST method. Next for prepared mesh an F.E.M. task is defined in POLYDATA with desired boundary conditions. Based on the prepared data file the task is calculated in POLYFLOW. Result stored in files contain data necessary to calculate the mixing task. General procedure for flow calculation is shown in figure 11.

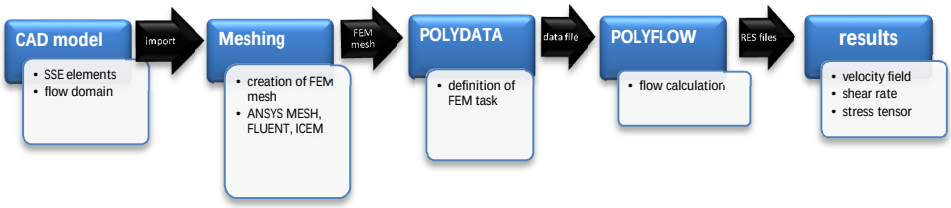

Fig.11 Workflow of flow simulation

3.2 Mixing simulation

Mixing task calculation is set in Polydata as a new simulation (preferably in the same Polyflow project). Results from flow simulation are referred in Polydata while defining mixing task. Mesh model used in mixing task calculation is the same as the mesh used during flow calculation. Boundary properties, the initial position of the material points and other properties are defined to evaluate along the trajectories. After finished pre-processing, mixing calculation is performed in Polyflow with prepared data file. Polyflow randomly generates the initial position of a set of material points and calculates their trajectory in the flow domain. Polyflow also calculates the evolution of some properties and kinematic parameters (temperature, viscosity, stretching, rate of stretching, rate of dissipation, and so on) along these trajectories, and generates a results file. General procedure for flow calculation is shown in figure 12.

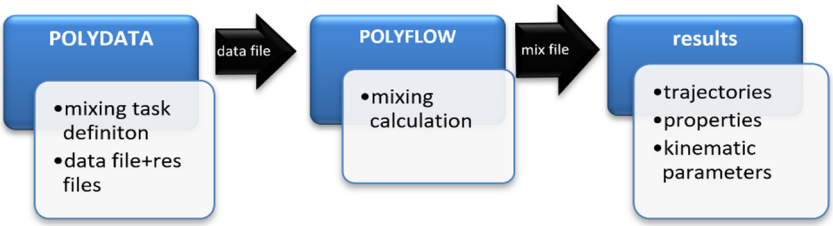

Fig.12 Workflow of mixing simulation

3.3 Statistical evaluation

To obtain relevant statistical data that quantifies the calculated mixing process, like mass distribution, distribution index **δ** ,points concertation deviation $\boldsymbol{\delta_p}$ etc. a statistical analysis in Polystat has to be performed. Results from mixing calculation are imported into Polystat postprocessor and trajectories of all points are analyzed. Calculation of basic mixing parameters like the time evolution of global mixing parameters such as the segregation scale or the evolution of the mean stretching or other parameters, can be extend by defining own function. It is also possible to visualize the spatial distribution of a kinematic parameter at a given time, or in a cutting plane, or along a given trajectory. Visualization of the statistical functions of these parameters using Polystat, Excel, or another similar postprocessor is possible. General procedure for flow calculation is shown in figure 13.

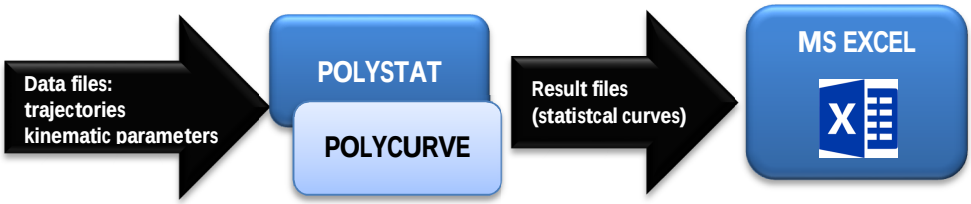

Fig.12 Workflow of statistical postprocessing

4. CFD evaluation of RBS

The evaluated conception of the rotational barrel segment is presented in figure 13. This conception concerns the plasticizing system with the screw without flights or with slight irregularities of the surface on the length of cooperation with the rotational barrel segment. The segment has flights on its inner surface, the same as on the screw. Due to the efficiency of the plasticizing system, the rotational barrel segment can rotate with different speeds in the direction compatible with the direction of screw rotation. The difference in the speeds of barrel segment and the screw influences the degree of polymer mixing and the efficiency of the system.

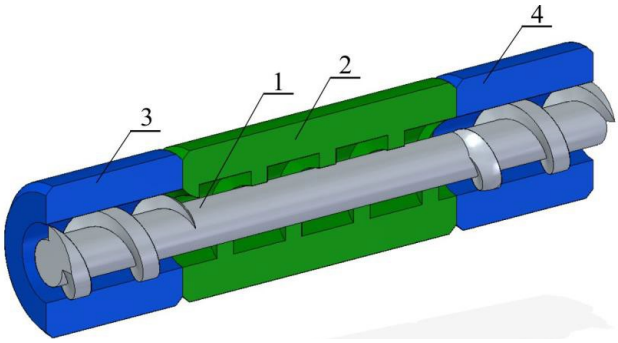

Fig.13 Longitudinal section of the plasticizing system with RBS and a screw without a flight on the length of the segment: 1 – screw, 2 – rotational barrel segment with a flight on the inner surface, 3 and 4 – immovable parts of the barrel

Total length of the model is 180mm, with RBS section length is 100 mm. Screw with diameter of 25 mm is placed inside barrel with diameter 25,5 mm. Segment 4 (fig.13) at the inflow side is 45mm long, and the segment 3 is 35mm long.

4.1 Simulation pre-processing

Based on the shape of the screw and RBS a CAD model of the flow domain was created. Flights from the screw, pins from RBS were eliminated and the Boolean operation was used to obtain the CAD model of flow domain (fig.14). The flow domain and moving elements was meshed in ANSYS Meshing ® to obtain hexahedral element mesh. To capture accurately the polymer flow in the area between barrel - screw flight and RBS-screw an inflation technique was used ensuring at least five mesh elements through thickness. Screw and RBS were meshed with ANSYS Fluent Meshing® resulting in the tetrahedral mesh. Subsequently, the mesh of the flow domain and the mesh of solid parts were joined and exported into ANSYS Polyflow. The final mesh consisted of totally 388 697 elements of which 71760 elements devolved to flow domain.

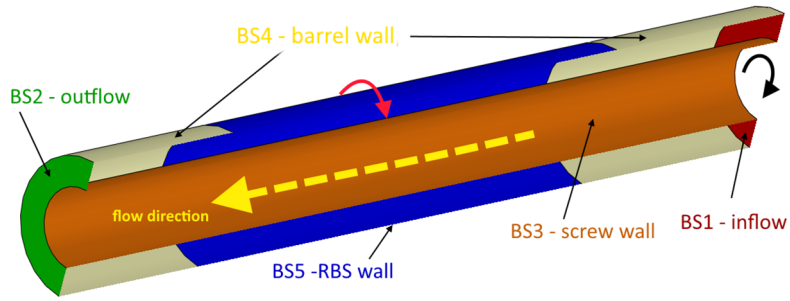

Fig.14 Longitudinal cross section through flow domain and labeling of boundary surfaces

General settings for the flow calculation were set as follows: Final scheme of the computational problem is shown in figure14. Flow boundary conditions on the mesh at selected boundaries (BS) were applied:

- BS1 – inflow (Q = 6.0 kg/h), mass flow rate across a boundary section surrounded by other boundary sections with well-defined adhesion conditions
- BS2 – normal forces and tangential velocities vanish (fn & vs) = (0, 0), typical use of this condition is for an exit section where the normal force is zero and the tangential velocity is constrained.
- BS3 – cartesian velocities imposed (vx & vy & vz) = 10.472 $rad.s^{-1}$ (100 rpm, direction see fig.14). While the stick condition is applied, polymer melt from flow domain touching the BS3, reach the speed of rotating screw
- BS4 – normal and tangential velocities imposed (vn & vs) = (0, 0). While the stick condition is applied, polymer melt from flow domain touching the BS4, has zero velocity.
- BS5- cartesian velocities imposed (vx & vy & vz) = 20.944 $rad.s^{-1}$ (200 rpm) according to scenario). While the stick condition is applied, polymer melt from flow domain touching the BS5, reach the speed of RBS.

The flow simulation was performed as F.E.M. transient task with initial time step of 0,5 seconds and final time 20 seconds. In this analysis is presented models of rupture of solid particles in a fluid matrix in a simple shear flow. We will follow the evolution of the size of numerous carbon black agglomerates N234 in HPDE matrix; submitted to shear stress, those particles erode or break into smaller fragments. Large number of particles introduced into flow domain at start of the mixing analysis causes that we do not follow the destiny of each individual particle, but we summarize information in a mass density function f(s,d), function of the size and the distance.

For the model of rupture, we assume that the rupture into a few fragments occurs if an agglomerate of size **S** is submitted to a shear stress higher than a critical shear stress $\sigma_{\mathbf{critR}}$ during a given amount of time (called rupture time). For the rupture of N234 carbon black pellets, the following experimental law and data are available in Polyflow (12) : $\boldsymbol{\sigma_{min}}$= 23227 [Pa] and $\boldsymbol{\beta}$ = 6628460 [Pa/μm]. The initial size distribution is a Gaussian function ranged between 15 and 25 [μm].

General settings for the mixing calculation were set as follows: Final scheme of the computational problem is shown in figure14. Flow boundary conditions on the mesh at selected boundaries (BS) were applied:

- BS1 – inflow. surface with start box with tracking points.
- BS2 – outflow
- BS3, BS4, BS5 – non penetrable

5. RESULTS AND DISCUSSION

Evolution of mass density function over the distance from the inflow boundary was observed (fig.15). First slice placed at inflow (d=0mm), shows a Gaussian distribution of particle size at the start. At the distance of d= 45mm, entry zone to RBS a second slice is placed. On this slice a mass density function for particle size shows, that light rupture of particles occurs in first section of analyzed SSE to mean size of 18,5µm. Further , during passing the RBS sections rupture of particles occurs, to size of 6,5 [µm] where further dissagglomeration can not occur, because not all conditions for rupture of particles are fulfilled.

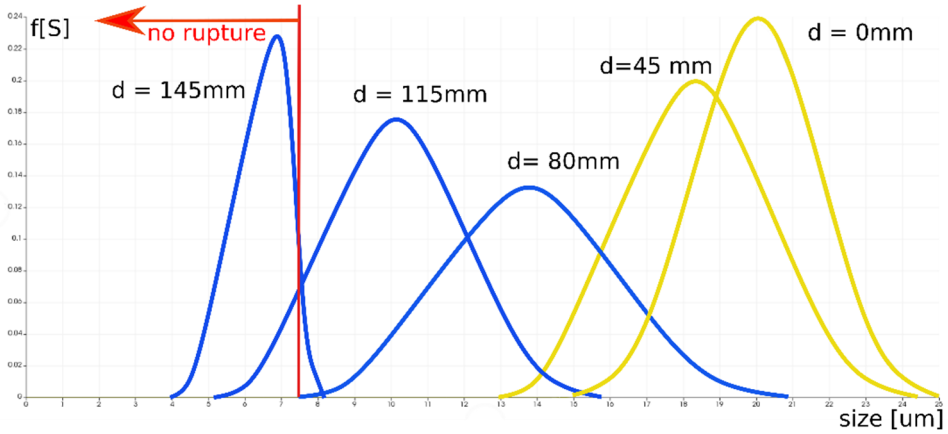

Fig.15 Distance evolution of mass density function for rupture of particles.

Presented results of CAE analysis of SSE in Polyflow shows, that the selected approach is fully applicable to evaluate complex problematic of polymer melt flow inside of SSE extruder barrel. Evaluation of flow through the whole flow domain is possible in full 3D space, and mixing performance is characterized with statistical methods. The process can be adopted to design optimal geometry and processing conditions for SSE with RBS, without need to build physical model for several iterations.

Acknowledgements

The project leading to this application has received funding from the European Union's Horizon 2020 research and innovation program under the Marie Skłodowska-Curie grant agreement No734205".

References

1. B. Alsteens: Mathematical Modelling and Simulation of Dispersive Mixing, PhD thesis. Université Catholique de Louvain, Louvain-le-Neuve, Belgium, 2005.
2. B. Alsteens, V. Legat: A Model for the Disagglomeration of Carbon Black in Rubber Matrix, Proceedings of the 6th Conference Eurheo, Erlangen, Germany, September 2002.
3. V. Collin, E. Peuvrel-Disdier: Dispersion Mechanisms of Carbon Black in Elastomers, Conference on European Rubber Research, Practical Improvement of the Mixing Process, Paderborn Germany. 2005.
4. P.V.Dankwertz: The Definition and Measurement of some Characteristics of Mixtures, Applied Science Research, 3. 279–296, 1952.
5. Tadmor,Gogos: Principles of Polymer Processing, John Wiley and Sons. 1979.
6. T. H. Wong and I. Manas-Zloczower: Two-Dimensional Dynamic Study of the Distributive Mixing in an Internal Mixer, Intern. Polymer Proc. IX. 1. 3–10, 1994.
7. H-H. Yang, I. Manas-Zloczower: Analysis of Mixing Performance in a VIC Mixer, Intern.Polymer Proc., IX. 4. 291–302, 1994.
8. ANSYS Polystat 2019 R2® online help - http://ansyshelp.ansys.com
9. I. Gajdoš [et al.]: 3D Finite Elements Simulation of the Single Screw Extruder with Rotational Barrel Segment, In: EUROGEN 2019: Extended Abstracts

Ana Maria A. C. Rocha[1], Marina A. Matos[2], M. Fernanda P. Costa[3],
A. Gaspar-Cunha[4], and Edite M. G. P. Fernandes[5]

POLYMER SINGLE SCREW EXTRUDER OPTIMIZATION USING TCHEBYCHEFF SCALARIZATION METHOD AND SIMULATED ANNEALING ALGORITHM

Abstract. *The single screw extrusion optimal design involves the optimization of six criteria that can be efficiently handled by a weighted Tchebycheff scalarization method. The performance of the method has been analyzed for three different methods to generate weight vectors.*
The experimental results show that the tested strategies provide similar and reasonable solutions and supply a valuable procedure to identify good trade-offs between conflicting objectives.
Keywords: *Single screw extrusion, Multi-objective optimization, Tchebycheff scalarization, Simulated annealing method*

1. Introduction

The single screw extrusion (SSE) design is concerned with the definition of the optimal screw operating conditions and geometry in such a way that some selected criteria achieve their best values. The screw operating conditions and geometry can be established using empirical knowledge, combined with a trial-and-error approach until the desirable criteria values are attained. However, a more efficient approach is to handle the SSE design as an optimization problem. The optimization of the SSE design is a very difficult task since it deals with the optimization of several criteria that are conflicting [1,2,3,4], which means that the improvement of one criterion leads to another criterion degradation.

The SSE design has been addressed in the past and the resulting multi-objective optimization problem has been solved by a multi-objective evolutionary algorithm (MOEA) named reduced Pareto set genetic algorithm (RPSGA) [2,3,5]. Most MOEA treat the multi-objective optimization problem as a whole and find the entire set of promising and desirable solutions in a single run of the algorithm. They are, in general, stochastic methods that generate, handle and mutate a population of solutions at each

1 *ALGORITMI Center, University of Minho, 4710-057 Braga, Portugal, arocha@dps.uminho.pt*
2 ALGORITMI Center, University of Minho, 4710-057 Braga, Portugal, aniram@live.com.pt
3 Centre of Mathematics, University of Minho, 4710-057 Braga, Portugal, mfc@math.uminho.pt
4 Institute for Polymer and Composites, University of Minho, 4800-058 Guimarães, Portugal, agc@dep.uminho.pt
5 ALGORITMI Center, University of Minho, 4710-057 Braga, Portugal, emgpf@dps.uminho.pt

iteration, like for example, the genetic algorithm, particle swarm optimization, differential evolution, ant colony optimization [6,7,8,9,10,11,12].

This paper aims to contribute to the research area of the SSE optimal design throughout a weighted Tchebycheff scalarization approach. The selected criteria of the SSE design problem are optimized using a scalarization function. A vector of weights has to be provided to construct the weighted Tchebycheff scalarization function and converge to a single solution. It is expected that with different weight vectors, the weighted Tchebycheff approach will converge to the trade-off solutions of the multi-objective optimization problem. Therefore, the success of the weighted Tchebycheff approach depends on an even distribution of the weight vectors. To analyze the performance and the effectiveness of the Tchebycheff approach, this paper tests three different methods to generate weight vectors. Although the differences are not significant, it is possible to identify the goodness of one relative to the others.

This paper is organized as follows. Section 2 describes the SSE problem exhibiting the six criteria to be optimized and the decision variables of the problem. Section 3 presents the basic concepts and a summary of some approaches to multi-objective optimization, Section 4 describes the proposed methodology to solve the SSE optimization problem and Section 5 contains a discussion of the obtained numerical results. Finally, Section 6 contains the conclusions of this study.

2. Single Screw Extrusion Problem

The most relevant criteria in the SSE design are the mass output (Q), the length of the screw required for melting the polymer (Z_t), the melt temperature at die entrance (T_{melt}), the mechanical power consumption (*Power*), the weighted average total strain (*WATS*) and the viscosity (*Visco*). These criteria, also called objective functions, depend on the values of two sets of parameters: the geometrical and the operating parameters. Given a set of parameter values, the corresponding objective function values are obtained using numerical modelling routines that describe the plasticizing SSE process [1]. Usually, the best design is attained by maximizing the objectives Q and *WATS*, and minimizing Z_t, T_{melt}, *Power* and *Visco*.

The geometrical parameters are related with the internal screw diameter of the feed zone (D_1) and metering zone (D_3), the axial lengths of the feed (L_1), compression (L_2) and metering (L_3) zones, the flight thickness (e) and the screw pitch (p). The parameter L_3 can be obtained from the equation $L_3 = L - L_1 - L_2$, since L is the total length of the screw (corresponding to the Z_t objective function, which is to be minimized).

The operating parameters that correspond to the operating conditions of the extruder are: the screw speed (N) and the temperature profile of the heater bands in the barrel (Tb_1, Tb_2, Tb_3). The range of variation of the screw speed depends on the characteristics of the extruder's motor and the reduction gear. The lower and upper bounds for the range of temperatures of the heater bands are the polymer melting temperature and the polymer onset of degradation, respectively. Thus, taking into consideration the extruder size range and layout, and assuming the processing of a

typical thermoplastic polyolefin (High Density Poyethylene-HDPE), the lower and upper bound vectors for these operating parameters are (10,150,150,150) and (60,210,210,210), respectively.

The study in this paper assumes that the geometrical parameters are previously fixed. The aim is to find the optimal values for the operating parameters - herein also denoted as decision variables of the problem - represented generically by the vector $x = (N,Tb_1,Tb_2,Tb_3)$, in such a way that the objectives Q and $WATS$ are maximized and Z_t, T_{melt}, $Power$ and $Visco$ are minimized. The multi-objective optimization formulation of the SSE problem is:

$$\text{Find a set of values for the vector } (N,Tb_1,Tb_2,Tb_3) \in \Omega \subset \mathrm{R}^4 \quad (1)$$
$$\text{such that the vector } (Q,Z_t,T_{melt},Power,WATS,Visco) \text{ is optimized,}$$

where the set Ω of feasible solutions is defined as $\Omega = \{(N,Tb_1,Tb_2,Tb_3) : 10 \leq N \leq 60, 150 \leq Tb_i \leq 210, i = 1,2,3\}$.

3. Multi-objective Optimization

Many problems emanating from industrial applications require the optimization of two or more objectives that are frequently conflicting. They are recognized as multi-objective optimization (MOO) problems and their solutions have been tackled by many researchers using a variety of methods. Assuming the minimization, the MOO problem can be formally defined as:

$$\text{Find } x^* \in \Omega \subseteq \mathrm{R}^n \text{ that minimizes the functions vector } (f_1(x),...,f_m(x)), \quad (2)$$

where $x \in \mathrm{R}^n$ is the vector of the decision variables, n is the number of decision variables, Ω is the feasible search region and the components of the vector $f : \mathrm{R}^n \rightarrow \mathrm{R}^m$ are the m objective functions to be optimized. The space R^n is called the decision space and R^m is called the objective space. When the objective functions are not conflicting, it is possible to find a solution where every objective function attains its minimum [12]. However, if the objectives are conflicting, i.e, the improvement of one objective leads to another objective deterioration, it does not exist one single optimal solution, but a set of alternatives - the non-dominated solutions - further ahead called Pareto optimal set. The decision-maker then selects one (or more than one) compromise solution, among the alternatives, that better satisfies his/her preferences.

3.1. Basic Concepts in MOO

The basic concepts in MOO are the following.

Definition 1. *A vector $f = (f_1,...,f_m)$ is said to dominate $\bar{f} = (\bar{f}_1,...,\bar{f}_m)$ if and only if*

$$\forall i \in \{1,...,m\}\ f_i \leq \bar{f}_i \text{ and } \exists i \in \{1,...,m\} \text{ such that } f_i < \bar{f}_i. \quad (3)$$

Thus, when two solutions $f^1 = f(x^1)$ and $f^2 = f(x^2)$, $x^1, x^2 \in \Omega \subseteq R^n$ are compared, one of these three cases holds: i) f^1 dominates f^2, ii) f^1 is dominated by f^2, iii) f^1 and f^2 are non-dominated.

Definition 2. *Let $f \in R^m$ be the objective functions vector. A solution $x^1 \in \Omega$ is said to be Pareto optimal if and only if there is no other solution $x^2 \in \Omega$ for which $f(x^2)$ dominates $f(x^1)$.*

Definition 2 says that x^1 is Pareto optimal if there is no other feasible solution x^2 which would decrease some objective f_i without causing a simultaneous increase in at least one other objective. Thus, it does not exist a single solution, but a set of solutions called Pareto optimal set (in the space of the decision variables) and the corresponding function vectors are said to be non-dominated.

Definition 3. *Given a MOO problem with objective function vector $f \in R^m$ and the Pareto optimal set X^*, the Pareto optimal front (PF^*) is defined as:*

$$PF^* = \{f = (f_1(x),...,f_m(x)) \text{ such that } x \in X^*\}.$$

The algorithms for MOO aim to find a good and balanced approximation to the Pareto optimal set (and Pareto optimal front PF^*). The goals are:

i) to find a manageable number of Pareto function vectors;
ii) to find Pareto function vectors that are evenly distributed along PF^*;
iii) to support the decision-maker to formulate his/her preferences and identify the compromise solutions.

3.2. General Approaches to MOO

Taking into consideration the point in time when the preferences of the decision-maker participate in the optimization process, methods for MOO can be classified as [6,7,12]:

- No preference participation: the preferences of the decision-maker are not taken into consideration. The solution obtained by a simple method will be accepted or rejected by the decision-maker.
- *A priori* participation: the preferences of the decision-maker are taken into consideration before the optimization process. These methods require that the decision-maker knows beforehand the priority of each objective.

- *A posteriori* participation: no preferences of the decision-maker are considered before the process. However, the decision-maker chooses a solution from the set of alternatives provided by the Pareto optimal front.
- Interactive participation: the decision-maker preferences are continuously used and adjusted during the optimization process.

MOO methods with *a priori* and *a posteriori* decision-maker participation are the most known and popular. The easiest ones are *a priori* methods that combine the multi-objective functions into a weighted scalar aggregation function, converting the MOO problem into a single objective optimization (SOO) problem. Simple and well-known SOO algorithms can then be used to find one optimal solution [6,7]. To obtain an approximation to the PF^*, the SOO method must be run as many times as the desired number of points using different weight vectors [13]. The most popular scalar aggregation function is the weighted sum. To solve problem (2) by the weighted sum method involves selecting a weight vector $w = (w_1,w_2,...,w_m)$ and minimizing the aggregation function

$$W_{sum}(x;w) = \sum_{i=1}^{m} w_i f_i(x).$$

If all weights are positive, minimizing W_{sum} provides a sufficient condition for Pareto optimality that is the minimum of W_{sum} is Pareto optimal. However, if $w_i \geq 0$ and $w_1 + \cdots + w_m = 1$ are the assumed conditions, and any of the w_i is zero, the solution may be only weakly Pareto optimal [14,15]. It has been reported the inability of the weighted sum method to capture Pareto optimal points that lie on non-convex portions of the Pareto optimal front. This weighted sum method has been extensively used not only to compute a single solution that may reflect the decision-maker preference, but also multiple solutions that provide approximations to the Pareto optimal front, using different sets of weights.

It is expected that different weight vectors will produce different trade-off points on the Pareto front. However, different sets of weights can lead to the same point or points very close to each other. Thus, choosing the sets of weights is an important issue since the solutions depend on the weights. Ideally, they must be an evenly distributed set of weights in a simplex. Nevertheless, it has been observed that the weighted sum method may fail to produce solutions evenly distributed on the Pareto front.

It can also be the case that the relative value of the weights reflects the relative importance of the objectives representing the decision-maker preferences. Frequently, judgments of the decision-makers are vague and their preferences cannot be translated to numerical values. While setting exact weights to objectives may be difficult, it is

expectable that rank ordering the importance of objectives be easier. Thus, rank order weight methods aim to convert the list of ranks into numerical weights. Each rank, r_i, is inversely related to the weight, e.g., $r_i = 1$ denotes the highest weight, $r_i = m$ means the lowest weight [16]. The rank exponent weight method produces the weights

$$w_i = \frac{(m - r_i + 1)^t}{\sum_{j=1}^{m}(m - r_j + 1)^t} \tag{4}$$

where r_i denotes the rank of the ith objective $i = 1,...,m$ and t is a parameter that can be estimated by the decision-maker. The value $t = 0$ assigns equal weights to the objectives, and as t increases, the weights distribution becomes steeper [16].

Classical uniform design methods for generating evenly distributed set of weights in a simplex include the popular simplex-lattice design and simplex centroid design [17]. In [18], a constructive method for the creation of a $\{m,q\}$-simplex lattice is presented and used to obtain the uniformly distributed weight vectors, in a MOEA context. For a weights vector of m components and assuming that q is a positive constant, representing the number of points equally distributed on each axis, the simplex consists of all valid mixture combinations - i.e., sum 1 - that can be created for the m components from the $q + 1$ levels $0,1/q,2/q,...,(q - 1)/q,1$. In general, it consists of $\binom{m+q-1}{q}$ design points [19].

Another scalarization method based on weights to model preferences is the weighted Tchebycheff method [20]. As opposed to the linear aggregation of the weighted sum method, the weighted Tchebycheff method relies on a nonlinear weighted aggregation of the functions f_i, as follows:

$$\begin{aligned} &\text{Minimize } W_{\max}(x;w) \equiv \max \{w_1 \,|\, f_1(x) - z_1^* \,|\, ,..., w_m \,|\, f_m(x) - z_m^* \,|\} \\ &\text{subject to } x \in \Omega \end{aligned} \tag{5}$$

where $z^* = (z_1^*,..., z_m^*)$ is the ideal point in the objective space, i.e., $z_i^* = \min\{f_i(x)$ such that $x \in \Omega\}$ for $i = 1,...,m$. Each term can be view as a distance function that minimizes the distance between the solution point and the ideal point in the objective space.

Minimizing $W_{\max}(x;w)$ can provide approximations to the complete Pareto optimal front by varying the set of weights [6,13]. Under some mild conditions, for each Pareto optimal $x^* \in X^*$ there exists a weight vector w such that x^* is the optimal solution of problem (5), and each optimal solution of problem (5) (associated with a weights vector w) is a Pareto optimal solution to problem (2) [6]. The weighted Tchebycheff method guarantees finding all Pareto optimal solutions with ideal solution z^*. One disadvantage of solving problem (5) is that $W_{\max}(x;w)$ is not smooth at some points, although this is easily overcame by implementing a derivative-free optimization method.

Methods from the class of *a posteriori* decision-maker participation compute a set of solutions to approximate the PF^* in a single run. They are, in general, stochastic population-based search techniques and are denoted by MOEA. These population-based meta-heuristics work reasonably well on difficult problems and are naturally prepared to produce many solutions from which the set of Pareto optimal solutions can be emanated. Known examples with industry applications are NSGA-II [8], SPEA-2 [21] and RPSGA [3]. The reader is referred to [6,7,22,23,24] for more details.

4. Weighted Tchebycheff Scalarization Algorithm

This section aims to present the herein implemented weighted Tchebycheff scalarization algorithm that is used to solve the MOO problem (2) throughout the minimization of the Tchebycheff function $W_{\max}(x;w)$, as shown in (5). To scale the objective values so that they are approximately of the same magnitude, the objectives must be normalized. Thus, each f_i is replaced by:

$$F_i(x) = \frac{f_i(x) - z_i^*}{z_i^{nad} - z_i^*}, \tag{6}$$

where z^* is the ideal objective vector and z^{nad} is the nadir objective vector. This way, the range of the normalized function is [0,1]. The vector z^{nad} is constructed with the worst objective function values in the complete Pareto optimal set X^*, i.e., $z_i^{nad} = \max\{f_i(x) \text{ such that } x \in X^*\}$ for $i = 1,...,m$, which is a difficult task [25]. For normalized objectives, the maximization of $F_i(x)$ can be reformulated as a minimization objective as follows:

$$\max F_i(x) = \min\left(1 - \frac{f_i(x) - z_i^*}{z_i^{nad} - z_i^*}\right).$$

To solve the MOO problem in (1), the approximations to z_i^*, $i = 1,...,m$ (see (6)) are found from empirical knowledge of the SSE equipment and the polymer material, which lead to the $f_i^{\min}$ values presented in Table 1. The table also displays the specific objectives of the function vector f and the estimator for the vector z^{nad}, the vector $f^{\max}$, obtained by empirical knowledge of the equipment and the polymer material.

Table 1. Objectives of the function vector f, $f^{\min}$ and $f^{\max}$

	Q	Z_t	T_{melt}	$Power$	$WATS$	$Visc$
$f^{\min}$	1.0	0.2	150.0	0.0	0.0	0.9
$f^{\max}$	20.0	0.9	220.0	9200.0	1300.0	1.2

Let $\{w^1, \ldots, w^{N_{weight}}\}$ be a set of N_{weight} weight vectors. According to the above stated, for each weights vector w^i, the minimizer of $W_{\max}(x;w^i)$ is an approximation to a Pareto optimal solution of the problem (2). Thus, our methodology to obtain an approximation to the PF^* is as follows. For each weights vector w^i, an approximation to $x^*(w^i)$ and the corresponding functions vector (approximation to $f(x^*(w^i))$) are computed by a SOO solver. The solution $x(w^i)$ obtained for the weights vector w^i is used as the initial approximation to the SOO solver for the next problem constructed with the next vector w^{i+1}. This process is repeated N_{runs} independent times. From the N_{runs} sets of function vectors (approximations to the Pareto optimal front), the non-dominated function vectors are selected to better represent the trade-off between the objectives. From there on the decision-maker may identify a set of compromise solutions. Algorithm 1 describes the main steps of the methodology.

Algorithm 1 Weighted Tchebycheff algorithm

Require: m (number of objectives), $N_{weights}$ (number of weight vectors), N_{runs} (number of runs)

1: Generate a set of N_{weight} weight vectors, w^i_j, $i = 1, \ldots, N_{weights}$, $j = 1, \ldots, m$
2: **for** $N = 1$ to N_{runs} **do**
3: Randomly generate $y \in \Omega$
4: **for** $i = 1$ to $N_{weights}$ **do**
5: Given y as initial approximation, compute $x(w^i)$ (approximation to $x^*(w^i)$)
6: Set $PF^{N,i} = f(x(w^i))$
7: Set $y = x(w^i)$
8: **end for**
9: **end for**
10: Select the non-dominated function vectors among the vectors $PF^{N,i}$, $i = 1, \ldots, N_{weights}$, $N = 1, \ldots, N_{runs}$.

In this study, the simulated annealing (SA) method is used to compute $x(w^i)$, in line 5 of the Algorithm 1. SA is a single solution-based meta-heuristic with origins in statistical mechanics. Meta-heuristics are approximate methods that can solve any complex optimization problem. As opposed to the exact methods, meta-heuristics do not require information about the properties of the mathematical functions involved in

the problem formulation. They are not problem-dependent methods. They search the feasible region for a reasonable good solution to the problem although they do not guarantee to find an optimal solution [26].

The SA method models the physical process of heating a material and controls the reduction of the temperature - the cooling process - in order to minimize the system energy and reduce defects [27]. This process is known as annealing. At each iteration of the SA algorithm, a new point is randomly generated using a generating probability function that depends on the temperature. The algorithm accepts a new point if it improves the objective function, but also accepts, with a certain probability, a new point that deteriorates the objective. See [26,27,28] for details. The temperature is used to control the search for the global solution, e.g., a higher temperature allows more new points to be accepted which lead to the exploration of different regions of the search space. On the other hand, a lower temperature favors the acceptance of improving new points which result in the local exploitation of a promising region. Along the iterative process, the temperature is systematically decreased through a cooling schedule. Algorithm 2 presents the main steps of the SA algorithm.

Algorithm 2 SA algorithm

Require: T_0 (initial temperature), $It_{\max} = 50$ (maximum number of iterations), w (the weights vector), x (initial approximation), $0 < \kappa < 1$ (cooling rate), N_t (number of trials per temperature)

Evaluate $W_{\max}(x; w)$
Set $T = T_0$, $It = 0$
repeat
  for $j = 1$ to N_t **do**
    Generate a new point $\bar{x}$ in the neighborhood of x using a generating probability, and evaluate $W_{\max}(\bar{x}; w)$
    if $\bar{x}$ is accepted according to the probability $P(x, \bar{x}; T)$ **then**
      Set $x = \bar{x}$
    end if
  end for
  Set $T = \kappa T$, $It = It + 1$
until $It \geq It_{\max}$

5. Experimental Results

The weighted Tchebycheff algorithm was coded in MATLAB® (MATLAB is a registered trademark of the MathWorks, Inc.). For each weights vector, the function $W_{\max}(x;w)$ is minimized using the SA solver from the Global Optimization Toolbox of MATLAB - the *simulannealbnd* function. On the other hand, the solver *simulannealbnd* invokes the *computerized simulator of the SSE process* that provides the objective function values *Q*, Z_t, T_{melt}, *Power*, *WATS* and *Visco* (output) given a set of values of the decision variables (input) [1].

For the experimental results the parameter values are set as follows: $It_{\max} = 50$ (adopted stopping criterion for *simulannealbnd*), $T_0 = 100$ (default value), $\kappa = 0.95$ (default value) and $N_{runs} = 5$ with $N_{weights} = 21$. We note that the use of a high number of weight vectors increases the computational complexity of MOO methods and, in some applications, they become impractical. The fixed values assigned to the geometrical parameters are: $L_1 = 300$, $L_2 = 300$, $D_1 = 20.0$, $D_3 = 26.0$, $p = 30.0$ and $e = 3.60$.

This study aims to analyze the performance of the Algorithm 1 when three different methods are used to generate the set of $N_{weights}$ weight vectors, to solve the MOO problem throughout the minimization of $W_{\max}(x;w)$. Setting weights is an approach to articulate preferences and may be applied to different methods [14].

The first implemented technique applies the rank exponent weight method, see (4), with $t = 1$ and the sequence of ranks $r = (1,2,3,4,5,6)$. When $t = 1$ is set the method reduces to the *rank sum weight method*. With the generated weights vector, the technique constructs all permutations (without replacement), a total of 6! vectors, and randomly selects 21 vectors. With the six objectives optimized simultaneously, the weighted Tchebycheff algorithm produces a set of six-dimensional non-dominated solutions, the Pareto front.

Since the most relevant objective is the mass output *Q*, to visualize the trade-offs between *Q* and the others, five two-dimensional projections of the Pareto front are drawn and shown in Figure 1. The (blue) small full circles represent the solutions obtained for all the sets of weight vectors, over 5 runs, and the (red) large circles are the non-dominated solutions among the whole set. Figures 1(a) and 1(c) show that as *Q* decreases, the lower are Z_t and *Power* respectively. It is observed from Figure 1(d) that as *Q* decreases, the greater is *WATS*. The tendency shown by the cloud of non-dominated solutions in Figure 1(b) indicates that for lower *Q* values there are several solutions with lower T_{melt} values but there are also solutions with larger T_{melt} values. From Figure 1(e) we can also see a considerable number of solutions with lower *Q* values but with moderate *Visco* values. The solution with the lowest value of *Visco* has a reasonable large value of *Q*.

Table 2 shows the values of the decision variables and the corresponding objective values for the six identified and selected solutions from the Pareto front. They are the extremes of the Pareto front. Point A corresponds to the solution with the highest *Q* value, B, C, D and F are the Pareto solutions where Z_t, T_{melt}, *Power* and *Visco* attain their lowest values respectively, and point E corresponds to the Pareto solution with the highest value of *WATS*.

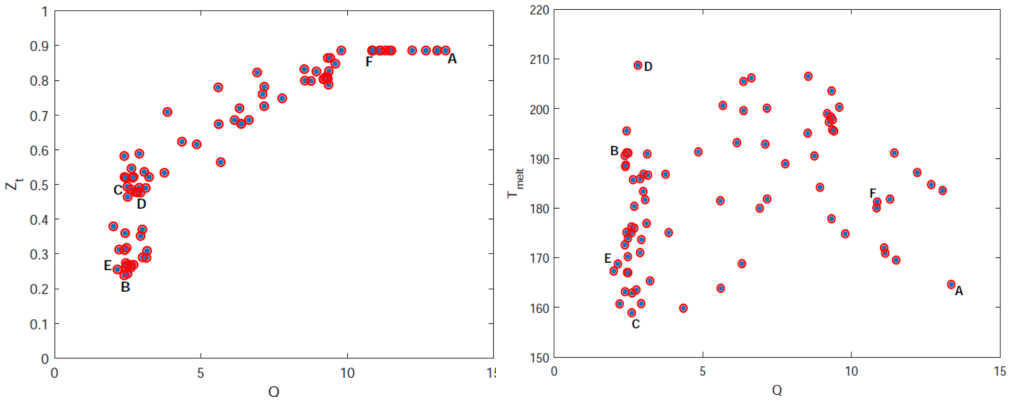

(a) *Q vs. Z_t*

(b) *Q vs. T_{melt}*

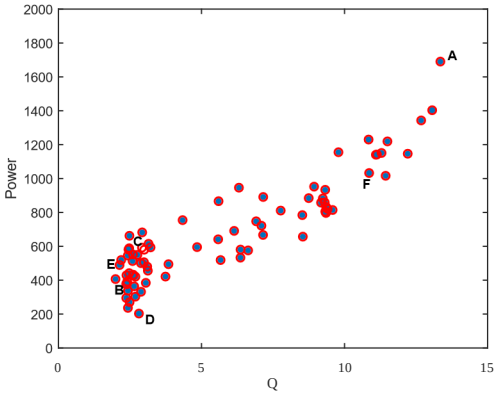

(c) *Q vs. Power*

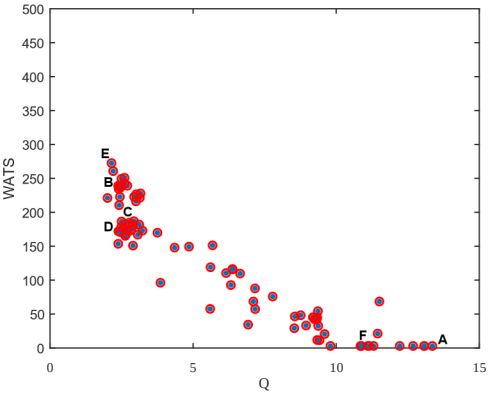

(d) *Q vs. WATS*

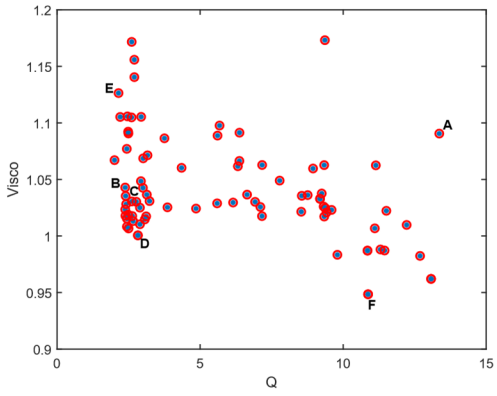

(e) *Q vs. Visco*

Fig.1. Two-dimensional projections of the Pareto front, when *rank sum weight method* and random selection are used

Table 2. Solutions with the best values of the objectives, when *rank sum weight method* and random selection are used

	operating parameters				optimized objectives					
	N	Tb_1	Tb_2	Tb_3	Q	Z_t	T_{melt}	$Power$	$WATS$	$Visco$
A	59.9	179	150	151	**13.36**	0.886	165	1689	3	1.09
B	10.1	205	176	202	2.38	**0.238**	191	377	239	1.04
C	12.9	187	153	159	2.62	0.486	**159**	550	183	1.03
D	10.0	157	208	210	2.82	0.478	209	**201**	174	1.00
E	10.3	208	151	174	2.15	0.255	169	488	**273**	1.13
F	46.5	187	168	191	10.87	0.886	181	1031	3	**0.95**

Another technique to generate the weight vectors is based on the *rank exponential weight method*, and uses the formula in (4) with the sequence of ranks r = (1,2,3,3,2,3) and the 21 values of t starting at 0, ending at 10, with a step of 0.5. The five two-dimensional projections of the Pareto front are shown in Figure 2.

Similar conclusions can be withdrawn relative to the behavior of the solutions, although with this weight generating method, the concentration of solutions is more expressive for large values of Q. Table 3 shows the values of the decision variables and the corresponding objective function values from the six extreme points of the Pareto front.

Table 3. Solutions with the best values of the objectives for the *rank exponential weight method*

	operating parameters				optimized objectives					
	N	Tb_1	Tb_2	Tb_3	Q	Z_t	T_{melt}	$Power$	$WATS$	$Visco$
A	59.9	177	210	210	**15.23**	0.886	209	1274	3	1.00
B	17.9	210	172	162	3.78	**0.526**	173	594	173	1.06
C	20.0	210	158	156	4.12	0.562	**163**	761	164	1.05
D	15.3	165	207	201	4.06	0.571	205	**334**	151	1.02
E	17.9	210	172	162	3.78	0.526	173	594	**173**	1.06
F	59.7	165	168	199	14.29	0.886	185	1580	3	**0.95**

The third technique, to generate the weight vectors, is based on the *simplex lattice design*. It starts by creating a $\{m,q\}$-simplex lattice, as presented in [18], where m = 6 and q = 8. Since the great majority of the created design points contain null components, we only select the design points that have all components positive to compose a set of 21 weight vectors.

The five two-dimensional projections of the Pareto front are shown in Figure 3. We note that the concentration of solutions is more expressive for lower values of Q, as was reported with the experiments based on the *rank sum weight method*. The other conclusions also apply here. The objective Q variation relative to the other objectives are similar to the previously described.

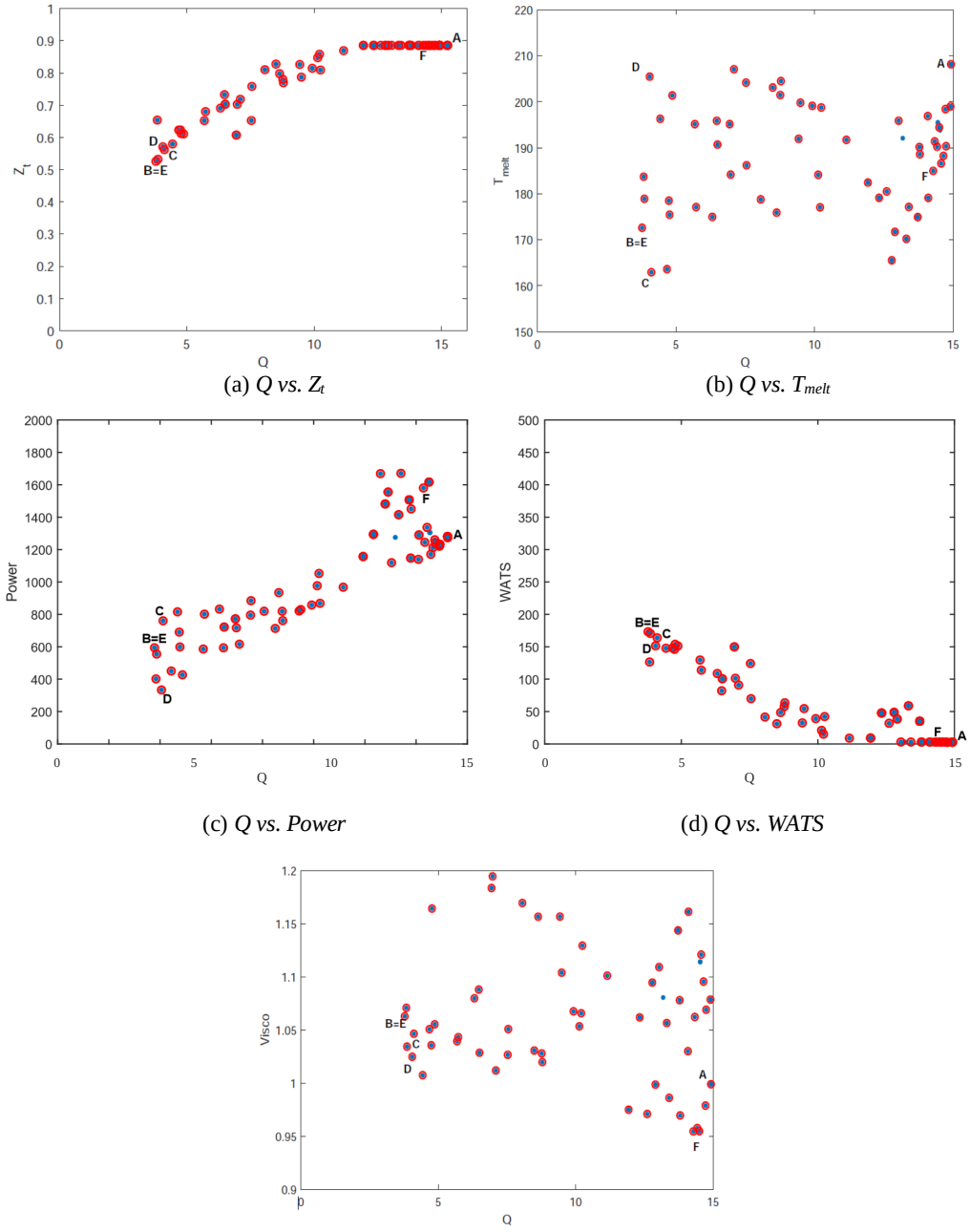

(a) *Q vs. Z_t*

(b) *Q vs. T_{melt}*

(c) *Q vs. Power*

(d) *Q vs. WATS*

(e) *Q vs. Visco*

Fig.2. Two-dimensional projections of the Pareto front for the *rank exponential weight method*

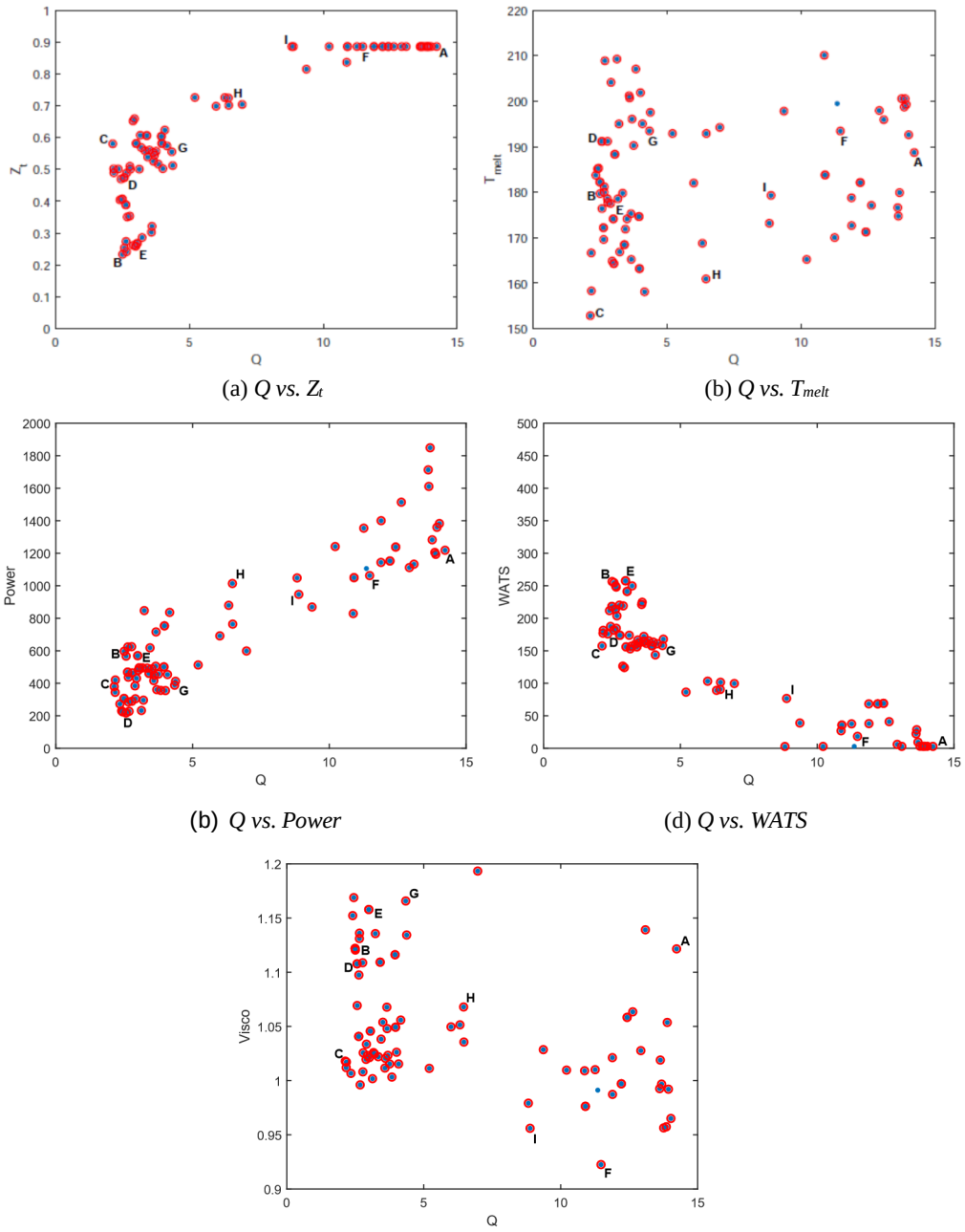

(a) *Q vs. Z_t*

(b) *Q vs. T_{melt}*

(b) *Q vs. Power*

(d) *Q vs. WATS*

(e) *Q vs. Visco*

Fig.3. Two-dimensional projections of the Pareto front, when the *simplex lattice design* is used

The six extreme solutions, A, B, C, D, E and F from the Pareto front are reported in Table 4 and correspond to the higher value of Q, lower value of Z_t, lower value of T_{melt}, lower value of *Power*, higher value of *WATS* and lower value of *Visco*, respectively. Operating parameter values and objective values from other three solutions, marked with G, H and I in Figure 3, are displayed in last rows of Table 4.

Table 4. Best objective values and other representative solutions using the *simplex lattice design*

	operating parameters				optimized objectives					
	N	Tb_1	Tb_2	Tb_3	Q	Z_t	T_{melt}	$Power$	$WATS$	$Visco$
A	58.4	201	193	168	**14.23**	0.886	189	1219	3	1.12
B	11.8	207	151	200	2.50	**0.233**	180	597	257	1.12
C	10.1	150	150	150	2.13	0.581	**153**	380	157	1.02
D	10.0	160	203	173	2.57	0.474	191	**218**	182	1.11
E	14.8	209	182	150	2.99	0.259	174	570	**258**	1.16
F	48.1	162	187	210	11.47	0.886	193	1063	18	**0.92**
G	17.2	178	208	166	4.34	0.555	193	388	158	1.17
H	30.4	208	150	151	6.46	0.725	161	1014	91	1.07
I	37.8	156	160	203	8.88	0.886	179	947	77	0.96

Analyzing the best values of the objective functions obtained from the three weight generating methods, we may conclude that the *simplex lattice design* technique provides in general slightly better objective values. To assist the decision-maker in his/her decision process, a widely used visualization strategy, known as value path graph, is depicted in Figure 4 in order to give more understanding and insights about the problem. This gives a parallel coordinate plot visualization for the Pareto solutions A, B, C, D, E, F, G, H, I reported in Table 4. The horizontal lines of different colors represent the values of the objectives for different trade-off solutions, i.e., each line is associated with one of the selected solutions. Objective values are normalized to facilitate interpretation and the comparison [29,30,31].

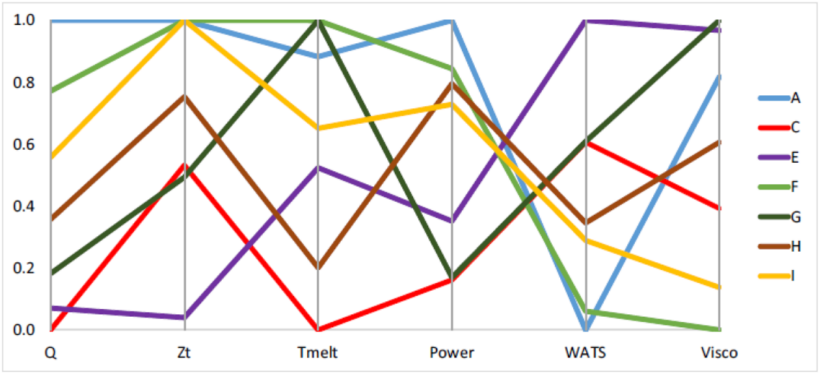

Fig.4. Value path of solutions produced by the *simplex lattice design* weight method

Solutions corresponding to points B and D are not included in the graph because they behave similarly to solutions E and G respectively. The graph highlights the trade-offs and also the similarity of solutions in terms of the objectives. For instance, solutions F and I are very similar. Solution F is better in terms of *Q* and *Visco*, but slightly worse in terms of T_{melt}, *Power* and *WATS*. Solution H is a balanced compromise between all objectives.

A pairwise coordinate plot (with correlation coefficient values) is depicted in Figure 5, which is useful to reveal (positive/negative) correlation or no (linear) correlation between pairs of objectives [32]. Due to its simplicity and completeness, this plot provides relevant information to the decision-maker. The numeric information inside each subplot contains:

"correlation coefficient"[*prob-value*]number of points in the subplot.

A value of *prob-value* less than 0.05 indicates that the correlation between the pair of objectives is considered statistically significant (positive if "correlation coefficient"> 0, negative if "correlation coefficient"< 0).

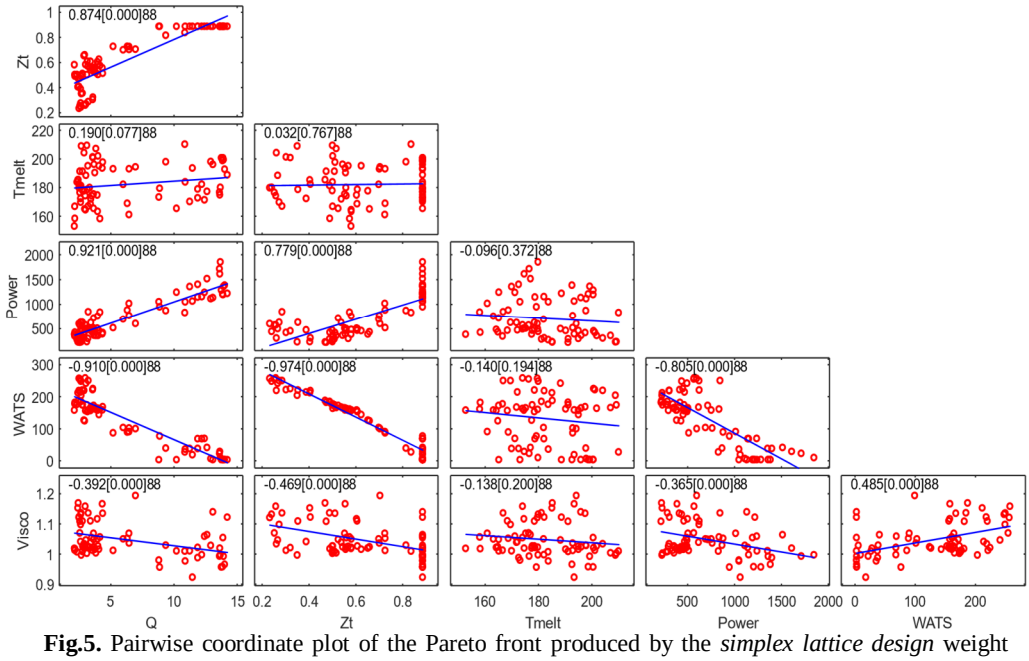

Fig.5. Pairwise coordinate plot of the Pareto front produced by the *simplex lattice design* weight method

6. Conclusions

In this paper, the MOO problem that emanates from the optimal operating conditions of a single screw extrusion is efficiently solved by the weighted Tchebycheff scalarization function and the SA method. Emphasis was given to the weight vectors generating process. Preferences relative to the importance of the objective functions have been also incorporated into the weight process. Experiments were conducted to compare the behavior of the non-dominated solutions provided by the three methods to generate weight vectors. To assist the decision-maker trade-off solutions have been identified from the two-dimensional projections of the Pareto front. The results were analyzed using a path value graph and a pairwise coordinate plot, in terms of the objectives, and show the viability of the weighted Tchebycheff method when solving the MOO single screw extrusion problem.

Acknowledgments. This project has received funding from the European Union's Horizon 2020 research and innovation programme under the Marie Skłodowska-Curie grant agreement No. 734205-H2020-MSCA-RISE-2017. The work has also been supported by FCT – Fundação para a Ciência e Tecnologia within the R&D Units Project Scope: UIDB/00319/2020, UIDB/00013/2020 and UIDP/00013/2020 of CMAT-UM.

References

1 Covas, J. A., Gaspar-Cunha, A., Oliveira, P, An optimization approach to practical problems in plasticating single screw extrusion, Polym. Eng. Sci. 39, 443–456, 1999.

2 Covas, J. A., Gaspar-Cunha, A., Optimisation-based design of extruders, Plast. Rubber Compos. 33, 9–10, 416–425, 2004.

3 Gaspar-Cunha, A., Covas J. A., RPSGAe - A multiobjective genetic algorithm with elitism: application to polymer extrusion, In: Gandibleux, X., Sevaux, M., Sörensen, K., T'kindt, V. (Eds.), Metaheuristics for Multiobjective Optimisation,´ Lecture Notes in Economics and Mathematical Systems vol. 535, Springer-Verlag, Berlin, pp. 221–249, 2004.

4 Covas, J. A., Gaspar-Cunha, A., Polymer Extrusion - Setting the Operating Conditions and Defining the Screw Geometry, In: Gaspar-Cunha, A., Covas, J. A. (Eds.), Optimization in Polymer Processing, Nova Science Publishers, pp 87–113, 2011.

5 Gaspar-Cunha, A., Covas, J. A., Costa, M. F. P., Costa, L., Optimization of single screw extrusion, In: Sikora, J. W., Dulebová, L. (Eds.), Technological and Design Aspects of the Processing of Composites and Nanocomposites, vol. I, Scientific-Practical International Workshop (NewEX H2020-MSCA-RISE-2017) Technical University of Kŏsice, 2018.

6 Miettinen, K. M.: A posteriori methods. In: Nonlinear Multiobjective Optimization. International Series in Operations Research & Management Science, vol 12. Springer, Boston, MA, pp. 77–113, 1998.

7 Emmerich, M. T. M., Deutz, A. H., A tutorial on multiobjective optimization: fundamentals and evolutionary methods, Nat. Computing 17, 585–609, 2018.

8 Deb, K., Pratap, A., Agarwal, S., Meyarivan, T., A fast and elitist multiobjective genetic algorithm: NSGA-II, IEEE T. Evolut. Comput. 6: 2, 182–197, 2002.

9 Coello, C. A. C., Lechuga, M. S., MOPSO: a proposal for multiple objective particle swarm optimization, In Proceedings of the Congress on Evolutionary Computation (CEC '02) pp. 1051–1056, 2002.
10 Branke, J., Deb, K., Miettinen, K., Slowinski, R. (Eds.), Multiobjective Optimization: Interactive and Evolutionary Approaches. Berlin, Germany, Springer-Verlag, 2008.
11 Santana-Quintero, L. V., Coello, C. A. C.: An algorithm based on differential evolution for multi-objective problems, Int. J. Comput. Intell. Res. 1: 2, 151–169, 2005.
12 Angelo, J. S., Barbosa, H. J. C., On ant colony optimization algorithms for multiobjective problems, In: Ostfeld, A. (Ed.), Ant Colony Optimization - Methods and Application, InTech Europe pp. 53–74, 2011.
13 Feng, Z., Zhang, Q., Zhang, Q., Tang, Q., Yang, T., Ma, Y., A multiobjective optimization based framework to balance the global and local exploitation in expensive optimization, J. Glob. Optim. 61, 677–694, 2015.
14 Marler, R. T., Arora, J. S., The weighted sum method for multi-objective optimization: new insights, Struct. Multidiscip. Optim. 41: 6, 853–862, 2010.
15 Ghaznavi-ghosoni, B. A., Khorram, E., On approximating weakly/properly efficient solutions in multi-objective programming, Mathe. Comput. Model. 54, 3172– 3181, 2011.
16 Roszkowska, E., Rank ordering criteria weighting methods - a comparative overview, Optimum. Studia Ekonomiczne, 5: 65, 14–33, 2013.
17 Ma, X., Qi, Y., Li, L., Liu, F., Jiao, L., Wu, J., MOEA/D with uniform decomposition measurement for many-objective problems, Soft. Comput. 18, 2541–2564, 2014.
18 Das, I., Dennis, J. Normal-boundary intersection: An alternative method for generating Pareto optimal points in multicriteria optimization problems, Institute for Computer Application in Science an Engineering, NASA Langley Research Center - Hampton, VA 23681-0001, Tech. Rep., 1996.
19 Meneghini, I. R., Guimarães, F. G., Evolutionary method for weight vector generation in multi-objective evolutionary algorithms based on decomposition and aggregation, 2017 IEEE Congress on Evolutionary Computation (CEC), San Sebastian, pp. 1900–1907, 2017.
20 Steuer, R. E., Choo, E. U., An interactive weighted Tchebycheff procedure for multiple objective programming, Math. Program. 26, 326–344, 1983.
21 Zitzler, E., Laumanns, M., Thiele, L., SPEA2: Improving the strength Pareto evolutionary algorithm, TIK-Report 103, Computer Engineering and Networks Laboratory (TIK), Department of Electrical Engineering, Swiss Federal Institute of Technology (ETH), Zurich ETH Zentrum, Zurich, 2001.
22 Deb, K., Multi-objective Optimization using Evolutionary Algorithms, John Wiley & Sons, 2001.
23 Padhye, N., Deb, K., Multi-objective optimisation and multi-criteria decision making in SLS using evolutionary approaches, Rapid Prototyp. J. 17:6, 458–478 (2011).
24 Coello, C. A. C., Brambila, S. G., Gamboa, J. F., Tapia, M. G. C., Gómez, R. H., Evolutionary multiobjective optimization: open research areas and some challenges lying ahead, Complex Intell. Syst. https://doi.org/10.1007/s40747-019-01134 (2019).
25 Deb, K., Miettinen, K., Chaudhuri, S., Toward an estimation of nadir objective vector using a hybrid of evolutionary and local search approaches, IEEE T. Evolut. Comput. 14: 6, 821–841, 2010.

26 Sörensen, K., Metaheuristics – the metaphor exposed, Intl. Trans. in Op. Res. 22, 3–18, 2015.
27 Kirkpatrick, S., Gelatt, C., Vecchi, M., Optimization by simulated annealing, Science 220, 671–680, 1983.
28 Wah, B. W., Chen, Y., Wang, T., Simulated annealing with asymptotic convergence for nonlinear constrained optimization, J. Glob. Optim. 39, 1–37, 2007.
29 Walker, D. J., Everson, R. M., Fieldsend, J. E., Visualising mutually nondominating solution sets in many-objective optimization, IEEE T. Evolut. Comput. 17:2, 165–184, 2013.
30 Miettinen, K., Survey of methods to visualize alternatives in multiple criteria decision making problems, OR Spectrum 36, 3–37, 2014.
31 Li, M., Zhen, L., Yao, X., How to read many-objective solution sets in parallel coordinates [Educational Forum], IEEE Comput. Intell. M. 12:4, 88–100, 2017.
32 Wesner, N., Multiobjective optimization via visualization, Econ. Bull. 37:2, 1226-1233, 2017.

José A. Covas[1], Sidonie F. Costa[2], Fernado M. Duarte[1]

STUDYING THE COOLING STAGE IN FUSED FILAMENT FABRICATION

Abstract: *Fused Filament Fabrication (FFF) is one of the available techniques that is capable of producing parts by additive manufacturing, i.e., by depositing thin filaments of thermoplastic polymers or composites onto a support as a vertical series of horizontal 2D slices of a 3D part. This chapter approaches FFF from a phenomenological point of view, and then focus on the deposition and cooling stage. A code capable of predicting the evolution of temperature during deposition and until cooling is completed, as well as of the final bonding between filaments is presented. The tool is then used to enlighten the effect of major processing parameters on the quality of parts.*

Keywords: *additive manufacturing, fused filament fabrication, fused deposition modelling, build orientation, filament bonding*

1. Introduction

Additive Manufacturing (AM) is a group of technologies that produces three-dimensional physical objects by gradually adding material, without the use of a mould. Since the 1980s, AM evolved from a niche method for rapid prototyping to a competitive manufacturing route, with potential substantial societal impact on various sectors such as healthcare, transportation, aerospace, electronics and construction [1]. Nevertheless, despite of the diversity of AM techniques, only a few seem to meet the practical requirements of industrial manufacturing of small series. This is the case of fused filament fabrication techniques (FFF) [2].

FFF use continuous thin filaments of thermoplastic polymers or composites that are deposited onto a support as a vertical series of horizontal 2D slices of a 3D part, which can exhibit significant geometrical complexity (see Figure 1). FFF comprise Free Form Extrusion (FFE) and the trademarked Fused Deposition Modeling (FDM). The first uses an extruder to produce the filament, whereas the second melts and extrudes a previously extruded larger filament (standard filaments have diameters of 1.75mm and 3mm). Figure 1 presents an example of a printed part, in this case a gear made of Polyether ether ketone (PEEK) (light colour) and electrically conductive PEEK (dark colour). The device was used to assess the 3D printing ability of

[1] *University of Minho, Institute for Polymers and Composites and Department of Polymer Engineering, Campus Azurém, 4804-533 Guimarães, Portugal, jcovas@dep.uminho.pt; fduarte@dep.uminho.p*

[2] *Center for Research and Innovation in Business Sciences and Information Systems (CIICESI), Porto Polytechnic Institute, Felgueiras, Portugal, sfc@estg.ipp.pt*

materials to be used by the European Space Agency to manufacture parts for satellites and other space applications [3].

This chapter approaches FFF from a phenomenological point of view, and then focus on the important deposition and cooling stage. A code to predict the evolution of temperature during deposition and until cooling is completed, as well as the resulting quality of the bonding between filaments is presented. The code is then used to study the effect of major processing parameters on the quality of the printed parts.

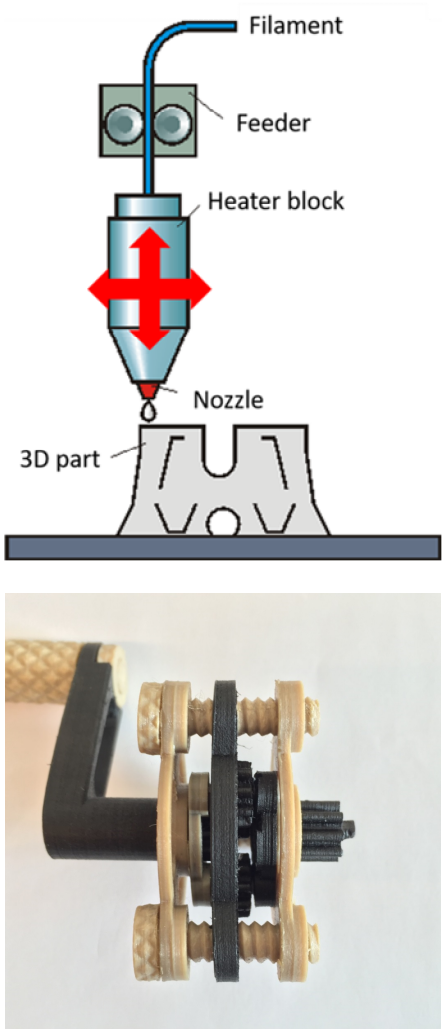

Fig. 1 Fused Filament Fabrication. Concept (top); example of a printed part made of PEEK (light colour) and electrically conductive PEEK (dark colour)(bottom).

2. Process stages

From a phenomenological point of view, FFF encompasses four main stages (see Figure 2). The first consists in feeding the filament (usually by means of a pair of counter-rotating rollers), which is then forced into the liquefier where it melts and is subsequently extruded through a nozzle (second stage). Since the filament is subjected to compression, it could eventually buckle. This led to a few technological improvements, such as using a filament guiding tube and a heat break (not represented). Flow in the liquefier is governed by the rheological properties of the melt. In the third stage, the viscoelastic melt simultaneously swells and is stretched axially by the movement of the printing head (because the velocity of the latter is usually higher than the linear velocity of the extrudate). Again, melt rheology is a determining factor.

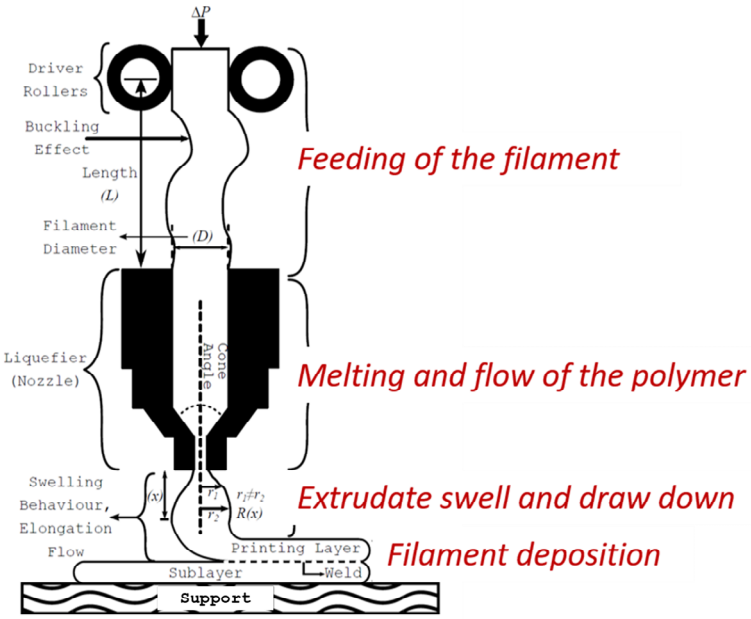

Fig.2 Main Stages of Fused Deposition Modeling

Figure 3 plots the viscosity curves (variation of viscosity with frequency) for a wide range of available commercial materials used in FFF. At the two frequencies considered (100 and 550s^{-1}), which are typically attained during printing with smaller and larger diameter filaments, respectively, the range of viscosities is relatively narrow, i.e., 320-1500s^{-1} and 195-540s^{-1}, respectively. This demonstrates

that despite its apparent simplicity and flexibility, FFF requires materials with relatively specific characteristics.

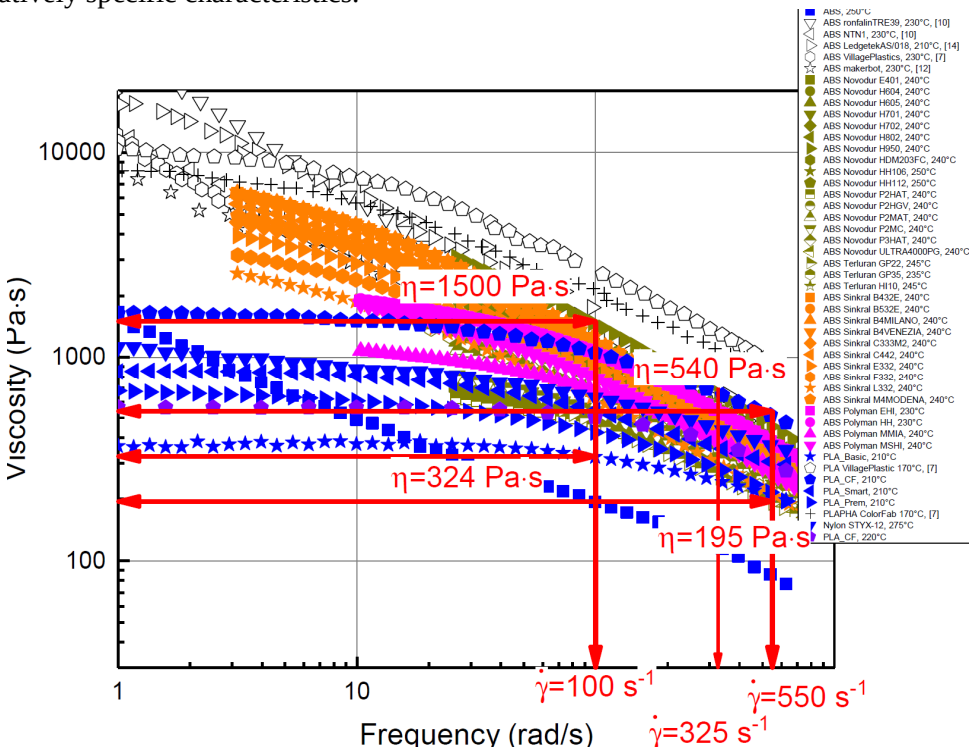

Fig. 3 Variation of viscosity with frequency for a variety of commercial materials used in FFF. The frequencies considered (100 and 550s^{-1}) are typically attained when printing with smaller and larger diameter filaments

The fourth stage consists of the actual manufacture of the part by filament deposition and cooling. As seen in Figure 4, the deposition stage involves filament deformation and bonding of contiguous filaments. Once deposited, each filament should solidify quickly to minimize the deformation due to gravity and/or the weight of the material that will be deposited above it. Conversely, it should remain sufficiently hot during enough time to ensure adequate bonding with the neighbouring filament(s). Simultaneously, differences in local shrinkage during cooling will induce the development of residual stresses which, in turn, may cause warping and eventual delamination [4]. Consequently, this stage is determinant for the quality of the final part in terms of engineering properties, surface quality and dimensional tolerances.

It has been shown experimentally that fabrication strategy, environment temperature and variations in convection determine the overall bond strength [5-7]. Figure 5 illustrates these concepts. It shows the interdependence between

temperature evolution in time and space, filament deformation and bonding between contiguous filaments, which determine the dimensional accuracy and mechanical performance, respectively. The processing parameters affecting temperature evolution are also identified.

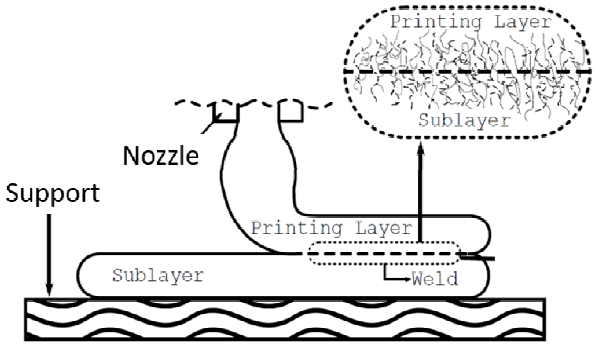

Fig 4 Filament deposition stage

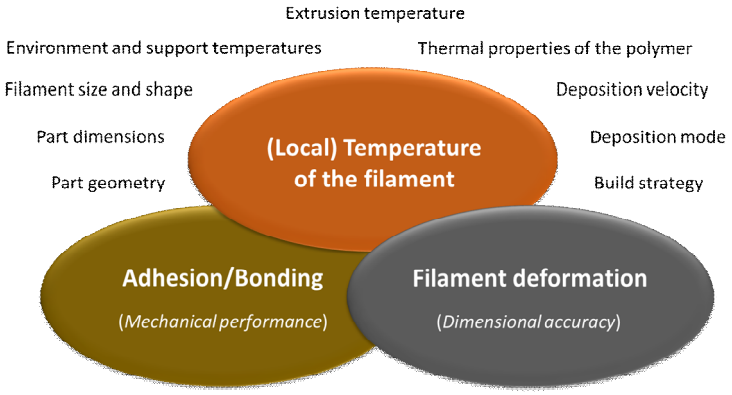

Fig 5. Effect of filament temperature on part quality and its influencing processing parameters

2. Modelling of cooling and bonding

Several authors, using different assumptions, have made predictions of filament temperature evolution during deposition. Initially, a single filament subjected to convection with the environment was considered [8, 9]. Then, cooling of a vertical filament stack was studied [10-12]. Only recently, the cooling of practical 3D parts has been tackled [13, 14].

During the deposition stage, heat exchanges by convection with the environment, by conduction between adjacent filaments and by conduction with the support are the most relevant. Moreover, the temperatures in any filament cross-section are relatively uniform [15]. Thus, modelling of heat transfer during cooling must consider the various possible contacts and corresponding heat transfer modes between any filament and its neighbors during the printing stage (see Figure 6). Filament contacts in the initial row/layer will be different from those between filaments in the remaining rows/layers, due to the presence of the support. The various heat transfer boundaries must be updated at small time increments as the deposition proceeds, being determined by the geometry of the part, build orientation and deposition sequence. Build orientation refers to the rotation of the part in the manufacturing space around the axes of the machine's coordinate system. Although it has been shown that it is a major parameter affecting the mechanical properties of parts [16], its optimization is generally performed in terms of geometrical parameters. Deposition sequence denotes the path taken by the filament during deposition, for example, unidirectional and aligned, unidirectional and skewed, or perpendicular. As with build orientation, its optimization has been mostly done with the aim of optimizing time paths, for example, by resorting to genetic algorithms [17,18]. However, the effect of deposition sequence on the mechanical properties of printed parts due to the associated changes in heat transfer has beeen recently recognized [19].

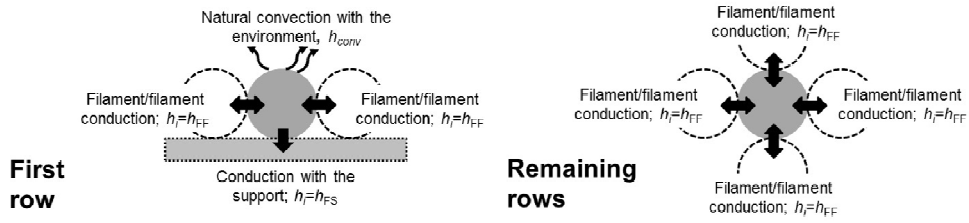

Fig. 6 Heat transfer modes in FFF for filaments in the first and remaining rows

Given the above, realistic modelling of cooling in FFF must include such aspects as thermal boundary conditions changing with time, different build orientations, and deposition sequence possibilities. The MatLab® computer code developed (Figure 7) contains an analytical solution to the transient heat conduction that is coupled to an algorithm that activates the relevant boundary conditions [13]. Also, the code incorporates a healing criterion [20], i.e., an assessment of the quality of bonding (dependent on local temperature history), that assumes non-isothermal conditions and is based on a formulation of reptation of polymer chains. The input parameters of the code include physical and thermal material properties, geometry of the part

and process parameters, such as extrusion velocity and temperature, deposition sequence, environment temperature, support temperature and filament dimensions.

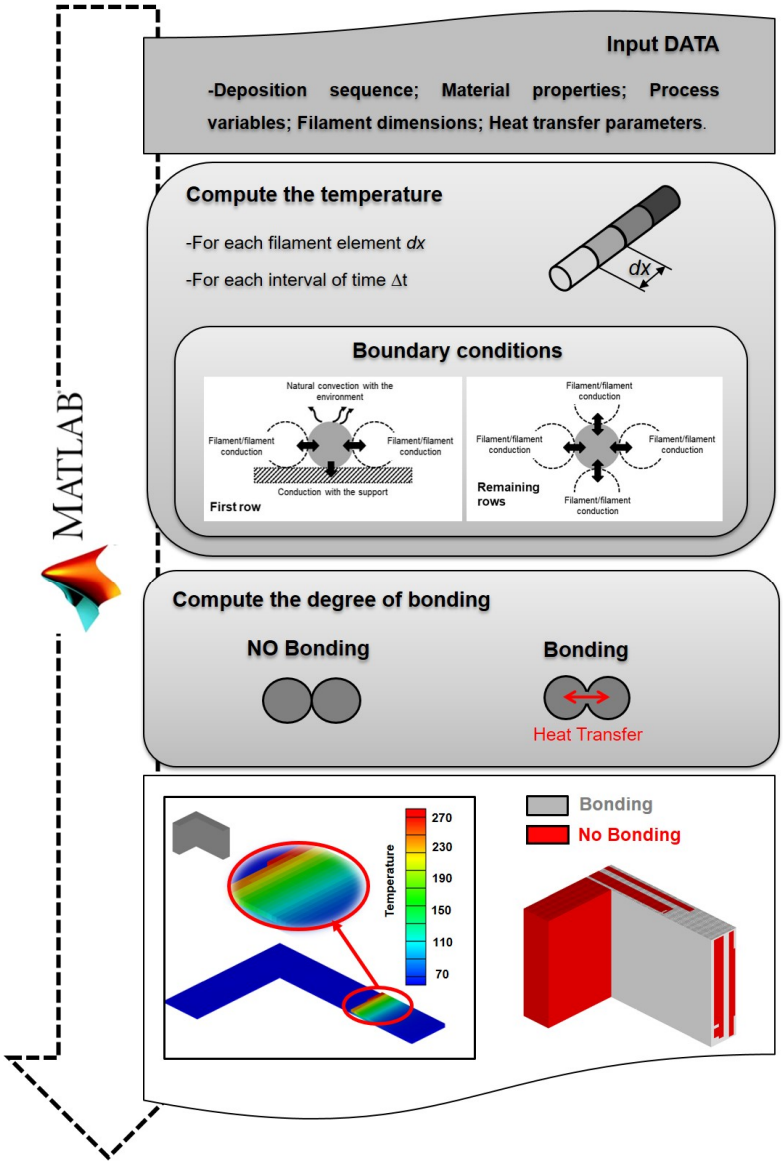

Fig. 7 Simplified flowchart of the computer code.

The predictions were experimentally validated [13]. For example, Figure 8 concerns the deposition of a vertical stack of 3 filaments. The plots are made for a

vertical cross-section distant 40 mm from the edge. Under the processing conditions used, the top filament was laid 6.7 s after the one in the middle, and 17.6 s after that at the bottom. The measured temperatures are in excellent agreement with the predictions.

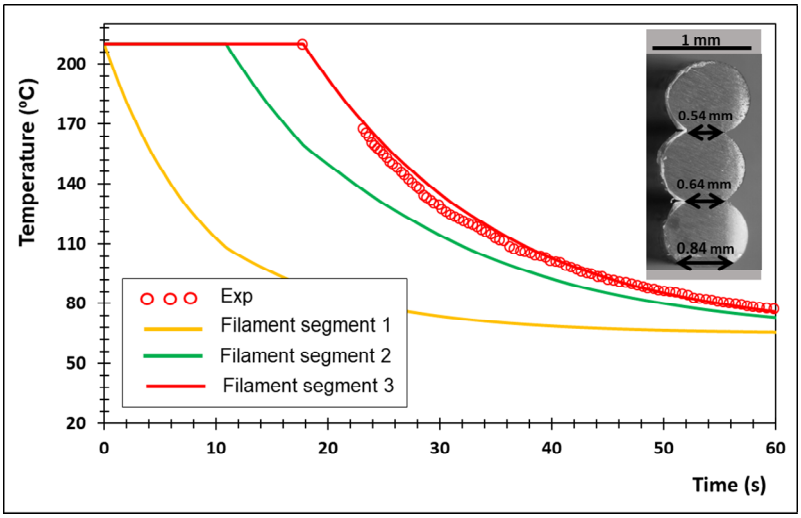

Fig. 8 Temperature evolution with time (at a vertical cross-section distant 40 mm from the edge) of a vertical stack of 3 filament segments (die set to 220ºC) (adapted from [13]).

Figures 9 and 10 illustrate the modelling capabilities of the code. Figure 9 depicts the time evolution of the temperature of ABS filaments 1–9 at a vertical cross-section at mid-length of the structure schematized in the inset. When a new filament is deposited, the temperature of the contacting filaments (previously deposited) increases and so their cooling is delayed. Even filament 1, which was the first to be deposited, is affected by the depostion of the remaining 8 filaments, although only filament 2 is in contact with it. These physical contacts can alter the local filament temperatures by as much as 18ºC. This raise in temperature, together with the time period during which it occurs, might be useful for bonding. Figure 10 presents the predicted time that is required for bonding between all pairs of contacting filaments of the structure represented in the inset, for three different extrusion temperatures. As expected, the higher the extrusion temperature, the lower the time required for bonding. In general, the latter is quite short, typically less than 0.25s, but while at the highest extrusion temperature all contacting filament pairs achieve bonding, this is not the case for the other two temperatures. For example, at 230ºC there is no bonding between filaments 1&2 (the first two filaments to be deposited), bonding between 2&3 and no bonding for pair 3&4. If there is no bonding, heat transfer

between filamentss 1 and 2 is limited. As a consequence, filament 2 remains sufficiently hot to bond to filament 3 when contact arises. For the same reasons, filament 3 cools faster and will not be able to bond to filament 4.

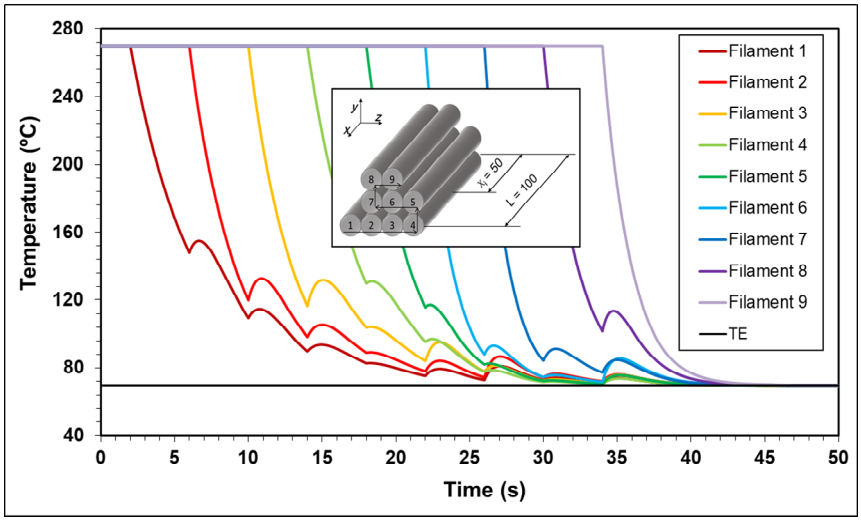

Fig. 9 Temperature evolution with time of filaments 1–9 for the geometry and deposition sequence illustrated in the inset at a vertical cross-section distant 50 mm from the edge (adapted from [13])

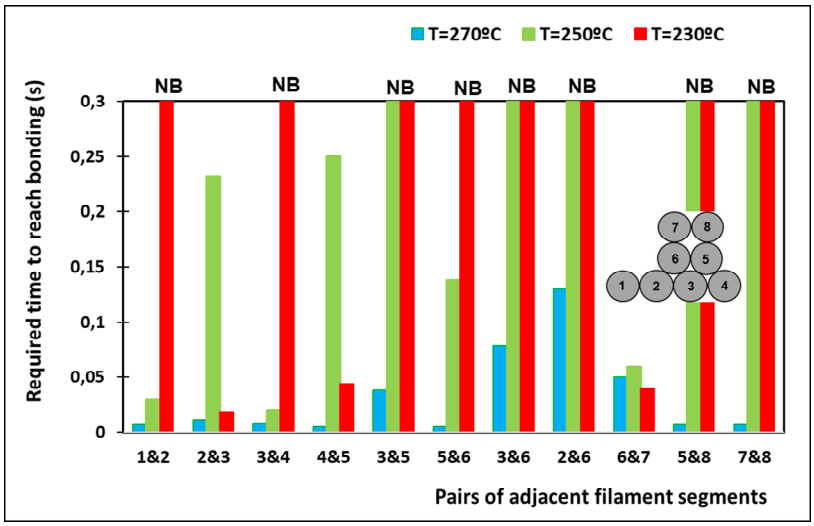

Fig. 10 Time required to achieve bonding between pairs of adjacent filaments segments for the geometry illustrated in the inset, at a vertical cross-section distant 50mm from the edge. NB –No Bonding (adapted from [13])

3. Effect of processing parameters on bonding

The part shown in Figure 11 will be considered in order to study the effect of processing parameters on the quality of bonding. It can be manufactured using six different build orientations (denoted as A do F), as demonstrated in Figure 12.

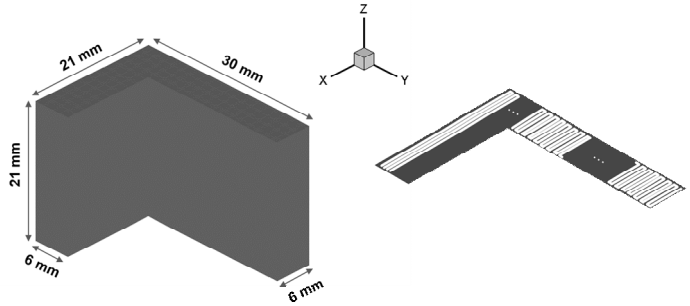

Fig. 11 Geometry, dimensions and deposition sequence (unidirectional aligned with 100% fill) of the part studied

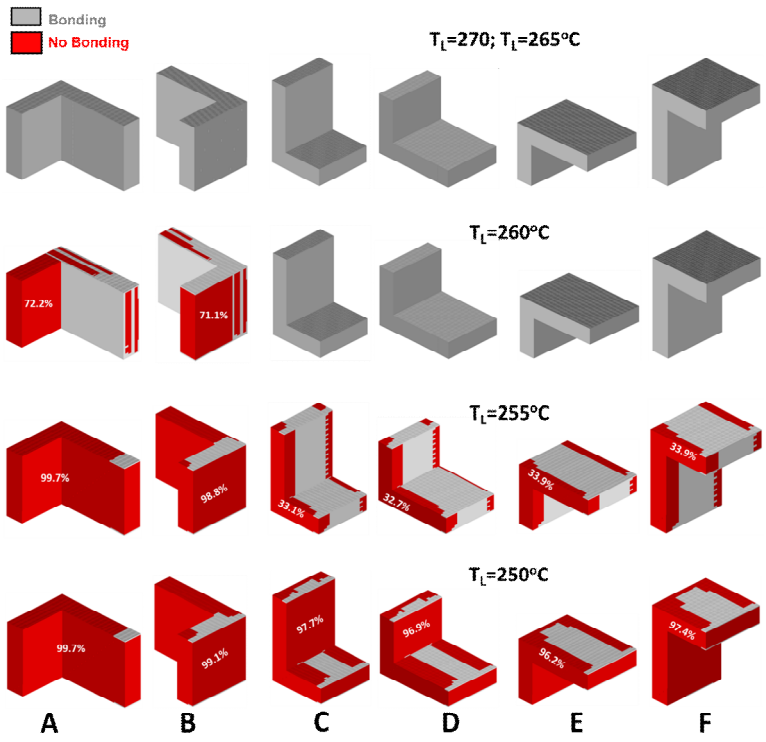

Fig.12 Influence of build orientation and extrusion temperature on bonding (environment temperature of 70ºC).

Orientations labelled E and F require support material. Orientations A to D involve the deposition of 3000 filaments, while orientations E and F are built from 7000 filaments. Obviously, this will result in different manufacturing times. Figure 12 gathers predictions of bonding quality (in terms of volume fraction of the part with bonding being achieved between filaments) when printing with different extrusion temperatures and using the six build orientations. For extrusion temperatures of 265ºC or 270ºC (typical extrusion temperature for ABS, a common polymer used in FFF), all parts exhibit good quality. When this temperature decreases, quality deteriorates progressively, and some delamination may become likely. At 250ºC, the parts should have little mechanical resistance. At constant extrusion temperature, build orientations A and B yield the worst bonding quality, while the remaining seem equivalent. However, orientations E and F entail longer manufacturing times.

Figure 13 represents graphically the correlation between extrusion temperature and bonding, for the various build conditions. Orientations A and B require extrusion temperatures 5ºC – 8ºC higher than the remaining to achieve parts with similar quality. The data follows two distinct patterns, one for orientations A and B, another for orientations C to F.

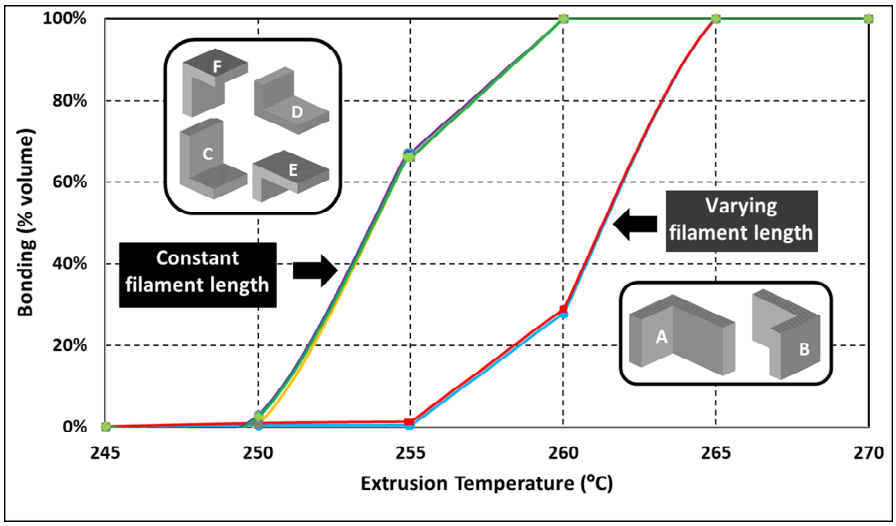

Fig. 13 Correlation between extrusion temperature and bonding, for various build conditions

As observed in Figure 11 (and indicated in Figure 13) build orientation A entails the deposition of long filaments in one side of the part, followed by short filaments in the another side. The reverse occurs for build orientation B.

However, in the remaining build orientations, the filaments have equal length. Since the printing velocity is constant, contacts between longer filaments occur at higher time intervals. Thus, these filaments are likely to cool down significantly before re-heating due to contact with a newly deposited filament. Simultaneously, the temperature raise may not be sufficient for bonding. This is further illustrated in Figure 14, which shows four snapshots of temperature at 10, 30, 45 and 75s of the deposition sequence for build orientation A, when extruding at 260ºC.

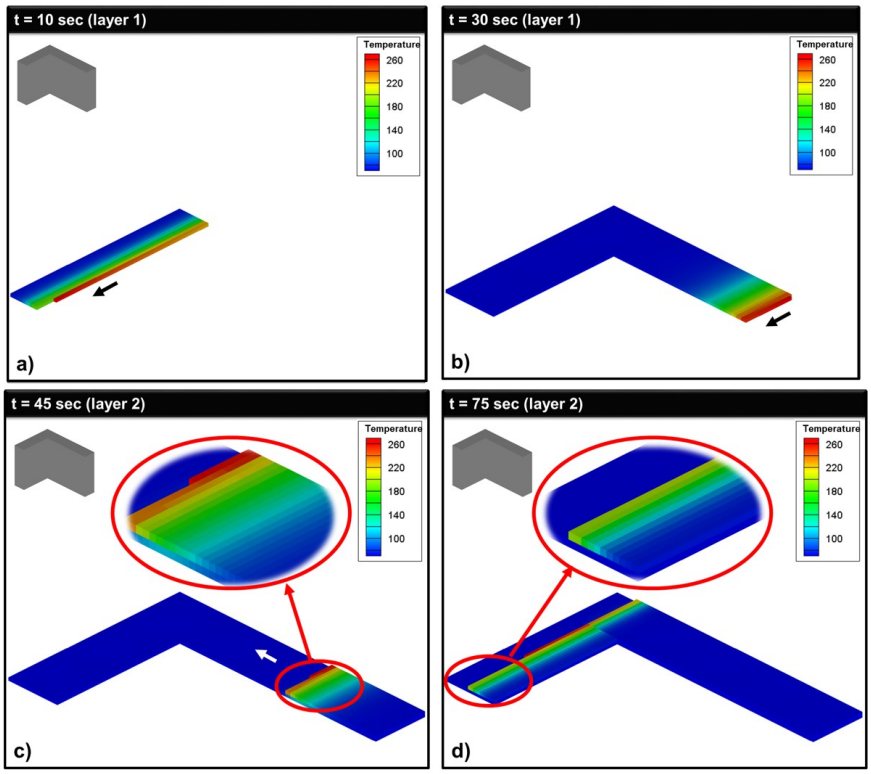

Fig. 14 Snapshots of material temperature at various instants of printing (build orientation A, extrusion temperature of 260ºC)

Printing begins at the left side of the first layer, which requires long filaments (Figure 14a). Then, the right side of the same layer is printed using short filaments (Figure 14b). The second layer is then laid, starting from the right side and progressively moving towards the left. This means that the new filaments of the second layer will be able to sufficiently re-heat the colder segments underneath to a temperature (during sufficient time) enabling bonding (Figure 14c). However, when printing the left hand side (figure 14d) the new filaments will be unable to reheat

meaningfully those of the first layer, as a long time since deposition of the latter has elapsed.

Close observation of the bonding quality shown in Figure 12 reveals regions alternating between bonding and no bonding, especially at 260ºC and for build orientations A and B. As discussed above and drafted in Figure 15 (left), if two filaments (1 and 2) become in contact after a long time, bonding will not be achieved. Filament 2 will remain relatively hot. Thus, when filament 3 contacts filament 2, bonding will be likely, if the time involved is sufficiently low. This sequence will continue, i.e., when filament 4 contacts filament 3, the time elapsed for their contact will determine whether bonding will occur. In more general terms, the lack of bonding between a pair of filaments prevents efficient heat transfer between them, causing slower cooling. In turn, might facilitate bonding with a newer hot filament. Conversely, when bonding develops, the higher heat transfer between them will promote faster cooling, which can hinder bonding with a newer filament (see illustration in Fig.15 (right)). The process is governed by the geometry of the part, build orientation and deposition sequence, but can be influenced by a proper choice of processing temperatures.

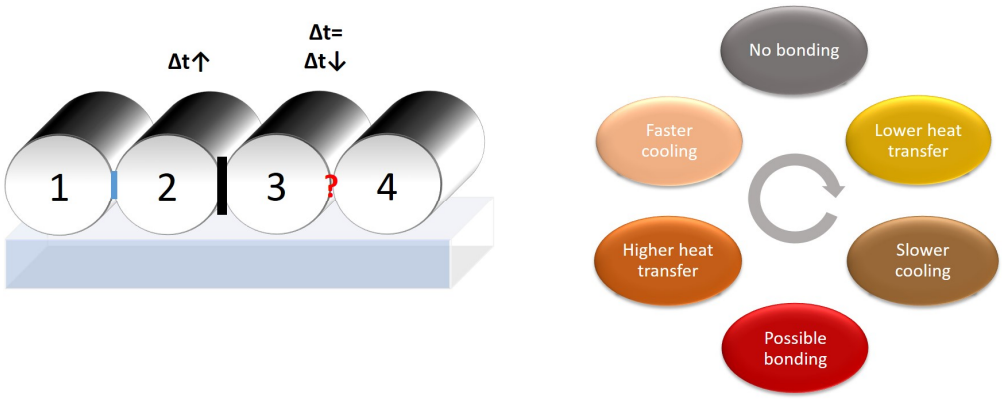

Fig. 15 A schematic explanation of how bonding between two filaments can hinder bonding with a third, newer filament

4. Selecting the printing conditions of a practical part

FFF are particulary advantageous for the manufacture of surgical instruments, due to their flexibility in terms of part geometry, easy adaptation to specific needs, and rapid manufacture. Figure 16 presents a scalpel handle, to be manufactured in ABS. Adopting unidirectional and aligned filament deposition and typical processing

conditions for ABS, it will take approximately 12 minutes to print the handle. Due to the geometry and thickness of the part, only two build orientations are feasible (Figure 16). They involve filament lengths ranging between 78 and 110 mm (orientation 1) and between 3 and 15 mm (orientation 2), respectively, thus affecting the instants at which contacts arise during deposition.

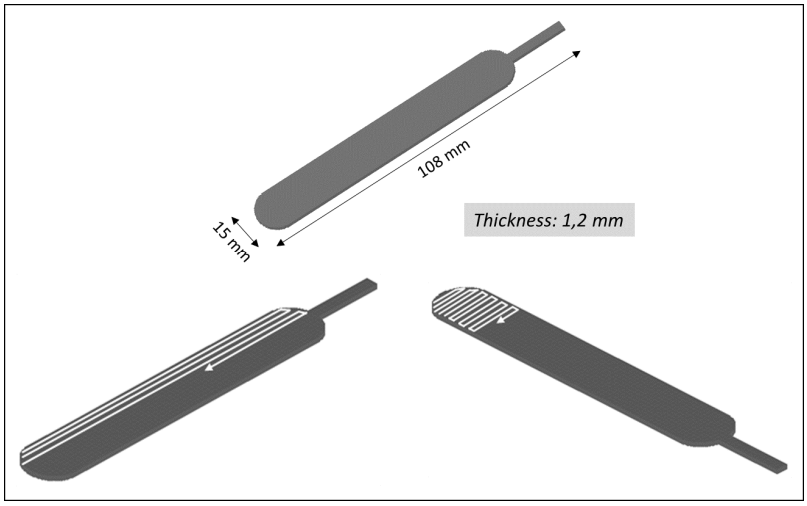

Fig. 16 Scalpel handle. Geometry of the part (top); build orientations (bottom)(left: orientation 1, involving 4 layers and 200 filaments; right: orientation 2, involving 4 layers and 1440 filaments).

Figure 17 predicts the correlation between extrusion temperature (ranging from 245 to 270ºC) and bonding, for the two build orientations. Below 260ºC, the handles will show poor mechanical performance. Raising the extrusion temperature to 270ºC solves the problem, which corroborates the practical choice of this temperature by most commercial 3D printers. Still, good parts could be obtained already at 265ºC, with build orientation 2. These predictions were made considering that the 3D printer is fitted with a (forced) convection oven with controlled temperature, which was kept at 70ºC. However, the most popular equipment operates at room temperature. Thus, assuming build orientation 2, natural convection, and the environment and support temperature $T_E = T_{sup}$ = 25ºC, Figure 18 presents bonding predictions for extrusion temperatures of 270ºC and 300ºC. Even raising the extrusion temperature well beyond its usual value, a handle with poor quality will be always obtained. As expected, bonding will be achieved only in the narrower edge, since here filaments are shorter and contact each other more frequently.

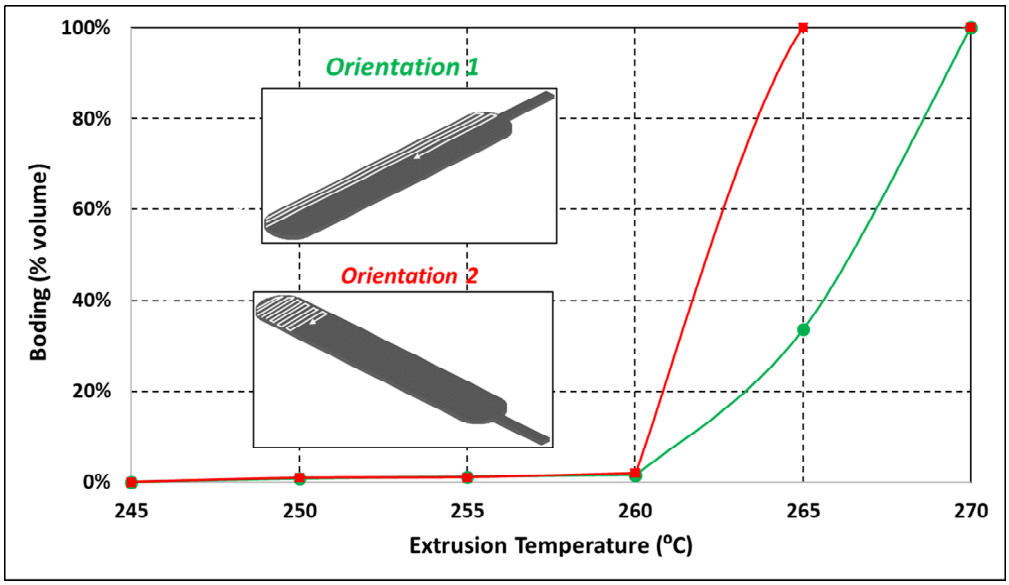

Fig. 17 Correlation between extrusion temperature and bonding of the scalpel handle, for two build conditions.

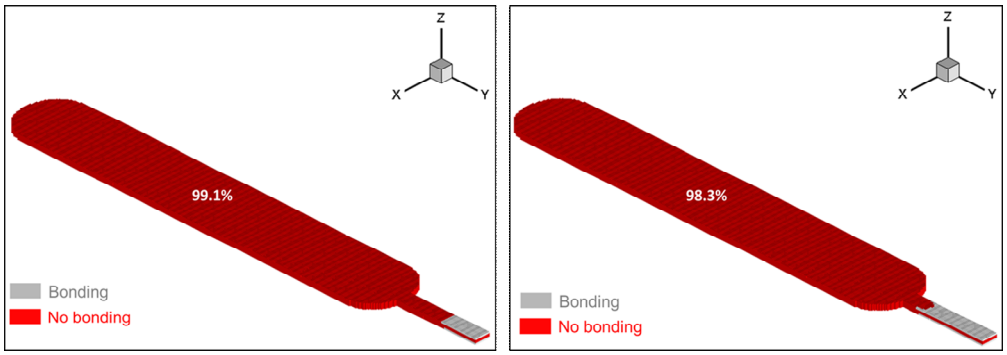

Fig. 18 Bonding predictions for build orientation 2, natural convection, environment and support temperature of 25ºC, extrusion velocity of 0.025m/s, for extrusion temperatures of 270ºC (left) and 300ºC (right).

One possible processing strategy to balance the heat losses to the environment would be to increase the extrusion velocity, as this would reduce the time between contacts. As seen in Figure 19, this route was only partially successful. When duplicating the extrusion velocity from 0.025m/s to 0.05m/s, the percentage of the part with poor bonding remained very high, albeit decreasing to 68% if extrusion is

performed at 300ºC.

In practice, most 3D printers allow to heat the support. Figure 20 displays bonding predictions assuming that the support is kept at T_{sup} = 100ºC, for two values of the thermal contact conductance with the support, extrusion velocity of 0.025m/s, and extrusion temperature of 270ºC. If the thermal conductance is sufficiently high, it is possible to obtain approximately half of the part with good bonding.

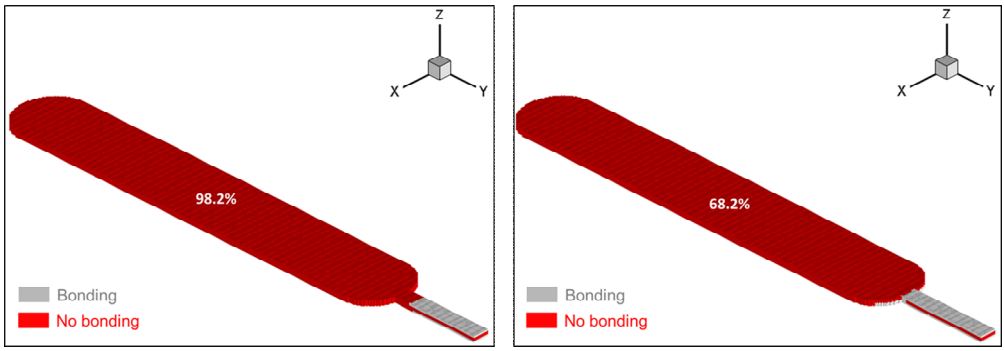

Fig. 19 Bonding predictions for build orientation 2, natural convection, environment and support temperature of 25ºC, extrusion velocity of 0.05m/s, for extrusion temperatures of 270ºC (left) and 300ºC (right).

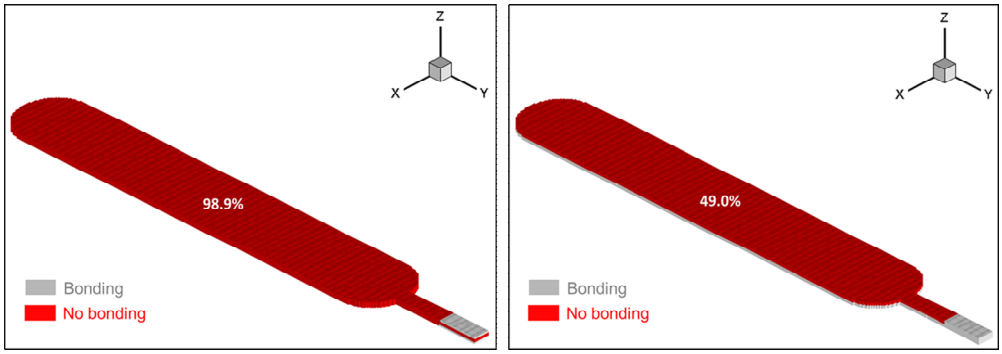

Fig. 20 Bonding predictions for build orientation 2, extrusion temperature of 270ºC, natural convection, environment temperature of 25ºC, support temperature of 100ºC, extrusion velocity of 0.025m/s, for thermal conductances of h_{sup}=10W/m^2.ºC (left) and h_{sup}=150W/m^2.ºC. (right).

5. Conclusions

This chapter studied FFF from a phenomenological point of view, focusing on the deposition and cooling stage due to its relevance to the characteristics of the final printed parts. Heat transfer is complex, and strongly influenced by both the geometry of the part and processing conditions. Therefore, process modelling tools can be quite useful not only to better understand the prevailing heat transfer mechanisms and related influencing parameters, but also to support the definition of adequate operating conditions for practical parts. The results showed that, whenever possible, 3D printers should be fitted with a convection oven, due to its helpful effect on bonding, which cannot be fully balanced by tuning other process parameters.

References

[1] J. R. C. Dizona, A. H. Espera Jr., Q. Chena, R. C. Advincula, Mechanical characterization of 3D-printed polymers. Addit. Manuf. 20 (2018) 44–67.

[2] S. Hertle, M. Drexler, D. Drummer, Additive Manufacturing of Poly(propylene) by Means of Melt Extrusion. Macromol. Mater. Eng. 301 (2016), 1482–1493.

[3] J. Gonçalves, P. Lima, B. Krause, P. Poetschke, U. Lafont, J. Gomes, C. Abreu, M. C. Paiva, J. A. Covas, Electrically conductive Polyetheretherketone nanocomposite filaments: from production to Fused Deposition Modelling, Polymers 10 (2018), 925-945

[4] A. Kantaros and D. Karalekas, Fiber Bragg grating based investigation of residual strains in ABS parts fabricated by fused deposition modelling process. Mater. Des. 50 (2013) 44–50.

[5] B. Céline, L. Longmei, Q. Sun, Q., P. Gu. Modelling of bond formation between polymer filaments in the fused deposition modelling process. J. Manuf. Process. 6 (2004) 170–178.

[6] Q. Sun, G. M. Rizvi, C. T. Bellehumeur, P. Gu, Effect of processing conditions on the bonding quality of FDM. Rapid Prototyp. J., 14 (2008) 72–80.

[7]] P.K. Gurrala, S. P. Regalla, Part strength evolution with bonding between filaments in fused deposition modelling. Virtual Phys. Prototyp. 9 (2014) 141–149.

[8]] M. A. Yardimci and S. Güçeri, Conceptual framework for the thermal process modelling of fused deposition, Rapid Prototyp. J., 2 (1996) 26-31.

[9] M. A. Yardimci, S. Güçeri., S. C. Danforth, 1997. Thermal analysis offused deposition. In: Proceedings in Solid Freeform Fabrication Symposium,Austin, TX (1997) 689–698.

[10] J. F. Rodriguez, J. P. Thomas, J. E. Renaud, J.E., 2000. Characterization of themesostructure of fused-deposition acrylonitrile-butadiene-styrene materials. Rapid Prototyp. J. 6, 175–185.

[11] J. F. Rodriguez, J. P. Thomas, J. E. Renaud, Design of fused-deposition ABScomponents for stiffness and strength. J. Mech. Des. 125 (2003) 545–551.

[12] - A. D'Amico, A. M. Peterson, An adaptable FEA simulation of material extrusion additive manufacturing heat transfer in 3D, Addit. Manuf. 21 (2018), 422–430.

[13] S. F. Costa, F. M Duarte, J. A. Covas, Estimation of filament temperature and adhesion development in Fused Deposition Techniques, J. Mat. Proc. Techn., 245 (2017) 167–179.
[14] Y. Zhang and V. Shapiro V. Linear-Time Thermal Simulation of As-Manufactured Fused Deposition Modeling Components, Journal of Manufacturing Science and Engineering, 140 (2018) 1-11.
[15] S. F. Costa, F. M. Duarte, J. A. Covas, Thermal conditions affecting heat transfer in FDM/FFE: a contribution towards the numerical modelling of the process, Virtual Phys. Prototyp., 10 (2015) 35-46
[16] J. Mueller and K. Shea, Buckling, build orientation, and scaling effects in 3D printed lattices, Mats. Today Commun., 17 (2018) 69-75
[17] P. K. Wah, K. G. Murty, A. Joneja, L. C. Chiu, Tool path optimi-zation in layered manufacturing. IEEE Transactions 34 (2002) 335–3479.
[18] G. Dreifus, K. Goodrick, S. Giles, M. Patel, R. M. Foster, C. Williams, J. Lindahl, B. Post, A. Roschli, L. Love, V. Kunc, Path optimization along lattices in additive manufacturing using the Chinesepostman problem. 3D. Print Addit Manuf 4 (2017) 98–10).
[19] N. Volpato and T. T. Zanotto, Analysis of deposition sequence in tool-path optimization for low-costmaterial extrusion additive manufacturing, The International Journal of Advanced Manufacturing Technology 101v(2019)v1855–1863.
[20] F. Yang and R. Pitchumani, Healing of Thermoplastic Polymers at an interface under Nonisothermal Conditions, Macromolecules, 35 (2002) 3213-3224.

José A Covas[1]

MONITORING OF POLYMER EXTRUSION AND COMPOUNDING PROCESSES

Abstract: *This work focuses on monitoring of polymer extrusion and melt compounding using single or twin-screw extruders. Standard extruder instrumentation aims at detecting eventual instabilities in flow and heat transfer in the extruder. Strategies for in-process monitoring considering the actual characteristics of the material being processed are presented and discussed. On-line and in-line approaches are defined. The advantages of sampling along the extruder barrel are demonstrated. Examples of the development and application of in-process optical spectroscopy and rheometry techniques are presented and discussed.*
Keywords: *extrusion, process monitoring, sampling, in-line, on-line*

1. Standard extruder instrumentation

The process control parameters of screw extruders include screw speed, feed rate (in the case of starve feeding, which is usually adopted in intermeshing twin screw extruders (TSE)), barrel and die temperatures, and vacuum level if the equipment is configured for a devolatilization stage. During operation, these parameters are kept within pre-defined intervals by programmable logic controllers (PLCs). Their values impact directly on the level of the thermomechanical stresses generated and on the residence time in the extruder.

Shear stress τ is the product of shear rate γ by melt viscosity η. If the latter follows a power law, τ is given by:

$$\tau = k \gamma^n H(T) \quad (1)$$

where *k* and *n* are the melt consistency and power law index, respectively, and H(T) is the temperature dependence, which can follow an Arrhenius-type law. Due to the complex flow patterns in the screw channels of an extruder, the shear rate varies locally but an average value γ_{av} can be estimated from:

$$\gamma_{av} = (\pi D N)/(60 h) \quad (2)$$

where *D* is the screw diameter, *N* is the screw speed and *h* is the channel depth. The maximum shear rate occurs in the gap betwen the crest of the screw flight (or the tip of the kneading disks, for co-rotating twin-screw extruders (co-TSE)) and the inner barrel wall. In the case of co-TSEs, the maximum shear rate is approximately 30

[1] *University of Minho, Institute for Polymers and Composites and Department of Polymer Engineering, Campus Azurém, 4804-533 Guimarães, Portugal, jcovas@dep.uminho.pt*

times higher than the average value [1].

The average residence time in the extruder is the ratio between the volume occupied by the material (assuming that the screw channel(s) work fully filled) and the volumetric output. Thus, this time is strongly influenced by the flow patterns developing along the various process stages along the screw(s) (typically, solids conveying, melting, melt conveying, mixing). For example, due to the helical flow pattern in the metering zone of a single screw extruder, the residence time in the center region of the channel is the lowest and increases towards the screw and barrel surfaces [2]. The total residence time distribution (RTD) has been used as a measure of the distributive mixing of the extruder [3], and is also important to estimate the necessary material thermal stability. Determining the average residence time and RTD in starve fed machines is even more complicated, as these characteristics are also influenced by the degree of fill. Either numerical modelling of the global plasticating process or experimental mesasurements using tracers can provide precise data on this topic.

Shear rate and melt viscosity will also affect viscous disspation, i.e., the increase in melt temperature resulting from intermolecular friction. Rauwendaal [2] showed analytically that in the metering zone of a single screw extruder the temperature rise increases with viscosity, channel length, screw diameter and screw speed, and decreases with melt density, specific heat, channel depth and helix angle. Figure 1 shows the effect of screw speed on the development of melt temperature along the length of a co-TSE during compounding of Polylactic Acid (PLA) with a chain extender. The barrel was fitted with a series of specially designed sample collecting devices [4] and kept at 210ºC. The melt temperature was measured by sticking a fast response thermocouple into the freshly collected melt (it takes less than 2 seconds to obtain a sample). Melting starts at screw turn number 9, as the material flows through a kneading block extending up to screw turn 11. Varying the screw speed between 100 and 300 rpm generated melt temperature differences of up to 60°C, and melt temperatures as high as 276ºC, i.e., almost 70ªC higher than the set value.

Given the complexity of flow and heat transfer in screw extruders illustrated above, it is obviously important to monitor the process, i.e., to obtain information in real time that helps to understand the phenomena developing in the extruder. This provides a better understanding of the process and opens the possibility to detect changes or anomalies that require action by the operator. Conventional extruder monitoring is usually limited to readings of motor amperage or torque, melt pressure and melt temperature, often measured at the die entrance. Motor torque can be used to calculate the specific mechanical energy (SME) (also known as specific energy consumption (SEC)), which represents the mechanical power consumed per unit mass of extrudate produced. Up to 70-80% of the total SME is consumed to raise the temperature of the solid polymer and melt it. SME can be computed by the following

equation, where the gearbox efficiency usally varies between 0.93 and 0.97:

SME [kWh/kg] = (nominal motor power) (applied torque/maximum torque) (screw speed/maximum screw speed) (gearbox efficiency) /mass throughput (3)

SEM can be used for quality control, to compare different manufacturing operations, or for scale up purposes. It correlates with screw speed, feed rate and barrel temperature. As wear increases, so does SME. Different materials exhibit distinct typical values of SME, from values lower than 0.25 kWh/kg for reactive polymer blending, to approximately 0.25 kWh/kg for polyolefins and up to 0.4kWh/kg for TPVs [2,5,6].

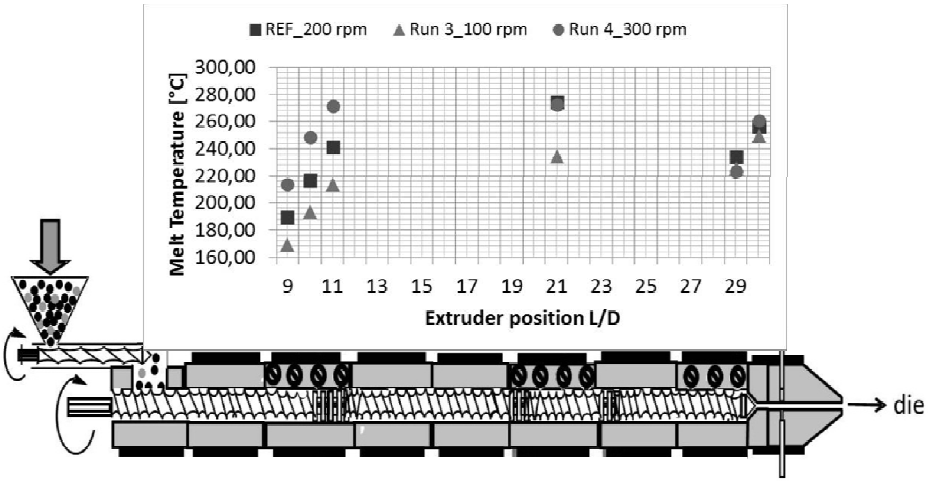

Fig. 1. Effect of screw speed on the development of melt temperature along the screw axis and die of a co-rotating twin screw extruder during compounding of Polylactic Acid with a chain extender (set temperature: 210ºC)

While readings of melt pressure are reliable and useful for process monitoring, the temperatures obtained from flush-mounted or even protuding temperature transducers can differ significantly from the true values, because these devices are ususally not insulated from the barrel wall and thus are largely influenced by its temperature [7]. Figure 2 compares the temperatures measured using flush-mounted transducers and a manual thermocouple stuck into the melt collected from sample collecting devices, for co-rotating twin-screw extrusion under different processing

conditions. Significant differences of up to 80°C were observed, as the readings of the transducers were largely influenced by the barrel temperature [7].

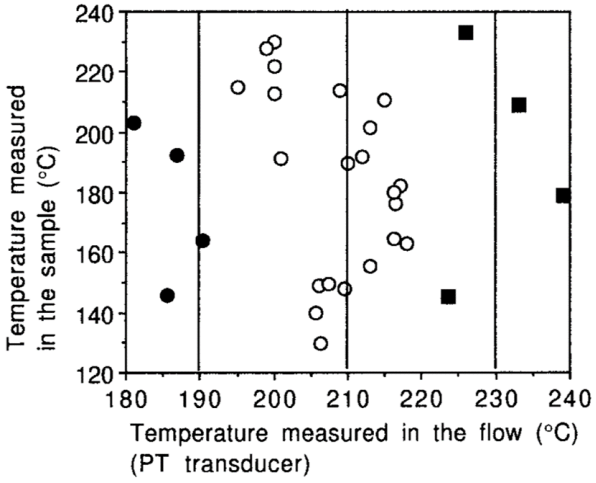

Fig. 2 Comparison between temperatures measured in the flow by PT transducers and in material samples collected from the extruder at the same locations: (full circles) T_b=190°C; (open circles) T_b =210°C; (squares) T_b=230°C [7]

2. Strategies for monitoring extrusion

Standard extrusion instrumentation aims at sensing attributes that relate to flow and heat transfer in the extruder. It is suited to assess process stability and to trigger corrective actions during operation whenever necessary. However, this type of instrumentation does not offer information on the actual characteristics of the material being processed. Consequently, practical material characterization often consists of collecting extrudate samples at regular intervals and perform tests in the laboratory. This off-line procedure is time consuming and entails important delays between sample collection and the eventually necessary adjustments to the extrusion operation (meanwhile, non-conform extrudate is being produced). These delays decline when the testing equipment is operated next to the processing equipment (known as at-line). A significant further reduction is achieved by coupling the testing device to the extruder and perform in-process measurements. When the data is obtained directly from the main melt stream (typically between extruder and die, or at die), measurements are named as in-line. On-line measurements are normally performed on a melt stream or material sample that was detoured from the main flow. After testing, the material is either wasted or returned to the main channel.

Figure 3 illustrates these concepts, using rheological measurements as example. In off-line testing, a sample is collected from the extrusion/compounding line and taken to the laboratory, where it is first subjected to compression moulding in order to obtain a disk that will be charged in the rotatioanl rheometer and re-heated prior to the messurement. Thus, during sample preparation, the material is subjected to two extra thermal cycles, which may trigger degradation or changes in morphology and/or in chemical conversion. On-line monitoring implies detouring a melt sample from the main flow channel, which is then tested under specific conditions (rate of deformation, temperature) and wasted or returned to the melt stream. During in-line monitoring, measurements are made in the main flow channel, usually at the die, or between the extruder and the die, under the local processing conditions.

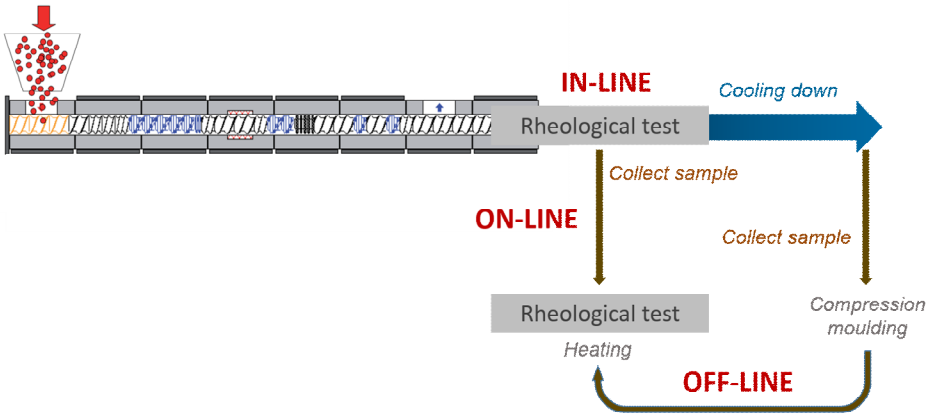

Fig.3 Off-line, on-line and in-line monitoring concepts in extrusion, using rheological measurements as example

In-process measurements are useful to assess both process stability and product quality, are essential for smart process control, and may contribute to swifter material and/or process development (e.g., fine tuning of a formulation, or determining the best operating window). A detailed discussion of in-process measurements advantages and requirements can be found elsewhere [8]. In extrusion, compounding and reactive extrusion, in-process monitoring can be performed using a variety of techniques, either alone or together, such as optical spectroscopy (Ultraviolet–Visible (UV–VIS), Infrared (IR), Fourier transform infrared (FTIR), Near-Infrared (NIR) and Raman), which deliver molecular or chemical composition information, rheometry, which is sensitive to the structure and morphological features at various dimensional scales, as well as other spectroscopy methods (e.g., fluorescence), small-angle light scattering (SALS), polarimetry, turbidity, ultrasonic attenuation and dielectric spectroscopy. Fluorescence

spectroscopy is often used to determine residence times and RTD by inserting fluorescent tracers in the flow stream [9-11]. SALS can estimate the size and shape of the droplets of the minor phase in a polymer blend or of the fillers in a polymer nanocomposite down to the sub-micron scale, but only for very low volume fractions [12,13]. Turbidity was utilized to estimate the particle size and shape of the dispersed phase in immiscible polymer blends [14], but again limitations in particle size and concentration apply. Polarimetry measures in real time polymer flow birefringence, which correlates with molecular weight, MW [15]. Ultrasound (vibrations with a frequency typically above 20 kHz) techniques have been frequently employed to monitor chemical conversion, MW, density, viscosity, melt temperature, orientation and relaxation, blend composition, blend morphology, RTD, melting evolution, etc. However, current commercial sensors can only sustain temperatures up to 150 ºC and 30 bar. Consequently, the testing set-up is relatively complicated, with measurements being made through-the-wall via a buffer and needing correction calculations [16]. Also, it may be difficult to discriminate the various effects in the signal captured. Dielectric spectroscopy was applied to detect variations in the composition of polymer/co-monomer [17] and liquid crystalline polymer (LCP)/PP blends [18].

Figure 4 depicts the in-process monitoring techniques developed at the University of Minho and presented in detail elsewhere [19-22]. Most of them can be applied at specific locations along the barrel of modified single and twin-screw extruders. Material sampling during operation enables subsequent off-line characterization, whilst shaping immediately after sampling yields specimens or disks for tensile testing or rotational rheometry, respectively (thus saving the material from being subjected to further thermal cycles). Capillary, rheo-optical slit, rotational and extensional rheometries are available on-line. RTD, electrical conductivity and NIR spectra can be measured directly on the flow in the screw channel, i.e., in-line.

The selection of the in-process technique(s) and experimental /procedure for a given extrusion or compounding operation depends on the type of data necessary, on the required rate of sensing, on the coupling possibilities to the extruder, among others [8]. Monitoring between extruder and die or at die are the most common, while obtaining data along the barrel of the extruder is rarely reported. The spectra produced by optical spectroscopy can be correlated with composition, and structural and morphological features. On-line capillary rheometry yields a viscosity flow curve (or the popular melt flow index (MFI)), which correlates with degree of polymerization, chain extension and degradation (either premature or controlled via reactive extrusion). Small amplitude oscillatory shear (SAOS) tests are commonly applied to analyze the in-situ compatibilization of polymer blends or the degree of filler dispersion in nanocomposites. Extensional viscosity is sensitive to changes in interfacial tension and thus is also relevant for polymer blends. Quality control requires good sensitivity to changes in the variable being monitored and reasonable

delay between sampling and obtaining data, while process control demands repetitive quick measurements. Various aspects of in-process monitoring techniques and applications have been discussed in the literature [8, 23-26].

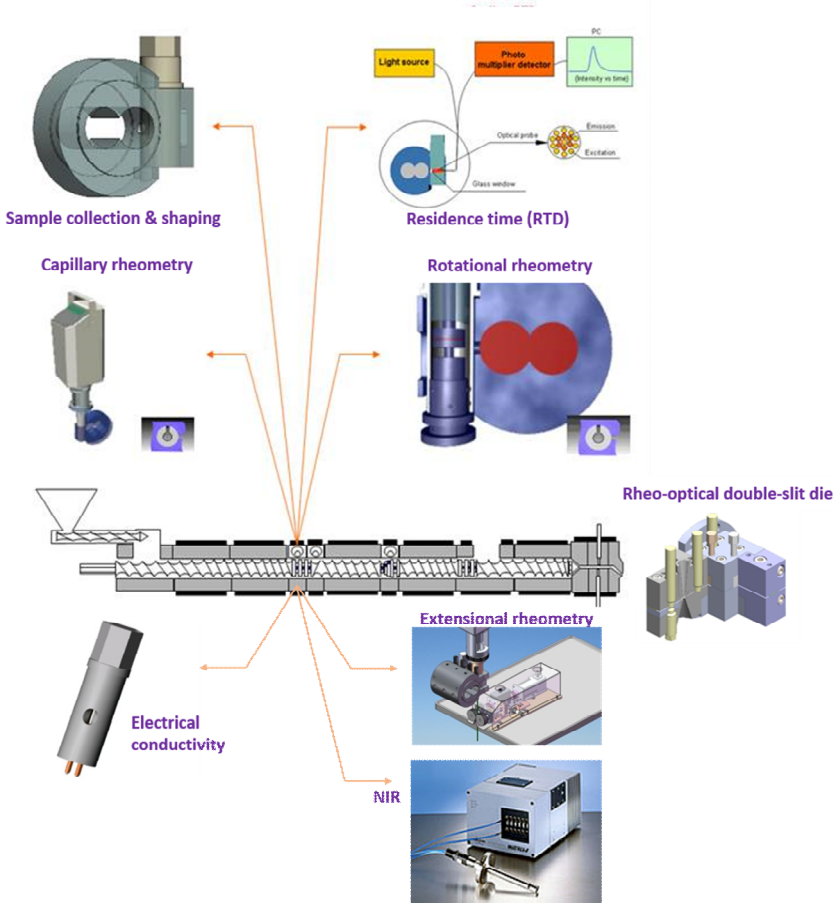

Fig. 4 In-process monitoring techniques for polymer extrusion and compounding implemented at the University of Minho

Figure 5 presents a mini-extrusion and compounding line (single and co-rotating twin-screw extruders can be interchanged) that was instrumented with the objective of charaterizing multiphase polymer systems, such as polymer blends and nanocomposites, using small amounts of material. The extruder is fitted with a series of sample collecting devices and is coupled to a rheo-optical slit die. The extrudates can be used to obtain test specimens for the measurement of engineering properties.

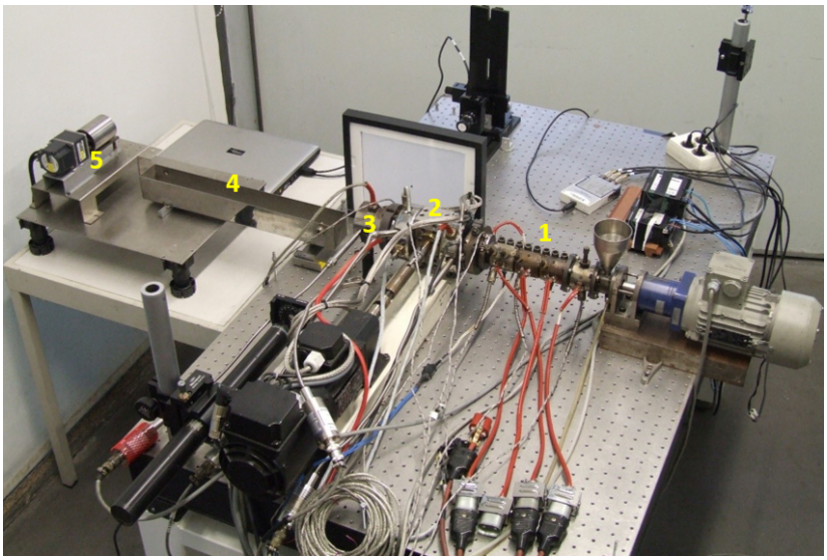

Fig. 5 – Mini-(single/twin) screw extrusion line with in-process monitoring capabilities; 1 - extruder with sample collecting devices; 2 - gear pump; 3 - rheo-optical slit die; 4 - water bath; 5 - winding

3. Sampling along the barrel

Monitoring along the axis of an extruder the development of melting, mixing, morphology, rheological response, chemical conversion and properties of a given polymer system may be important to uncover the underlying physico-chemical mechanisms and correlate them with the processing parameters, as well as to define the most adequate material recipe, screw geometry and/or operating conditions. In practice this is difficult to achieve, since the barrel of extruders is a black box. Therefore, a significant percentage of the experimental data obtained along the screw(s) was collected from screw-pulling experiments (known as Maddock-type, honouring the pionnner of this method) that involve interrupting extrusion, cooling down the barrel, removing the die and pulling out the screw(s) to expose the material. Not only this procedure is laborious and time-consuming, but since it is very difficult to freeze rapidly the material in the extruder, melting, coalescence or reagglomeration in the case of polymer belnds or nanocomposites, respectively, and chemical conversion if a reaction is taking place, may develop or continue during the process [27]. This situation is clearly demonstrated in Figure 6, which compares the evolution of the average particle size (computed here as equivalent circle diameter) of ethylene/propylene copolymer (EPM) droplets suspended in a polyamide 6 (PA6) matrix, measured on samples collected from the same axial locations, but obtained with the sampling devices mentioned above and with the classic screw pulling

experiments. Samples collected during operation of the machine showed that melting occurred upstream of the location inferred from conventional experiments. Moreover, particle sizes were generally smaller in the first case, thus indicating that during cooling of the extruder and extraction of the screws coalescence developed, which is not surprising since PA6/ and EPM form immiscible blends [28].

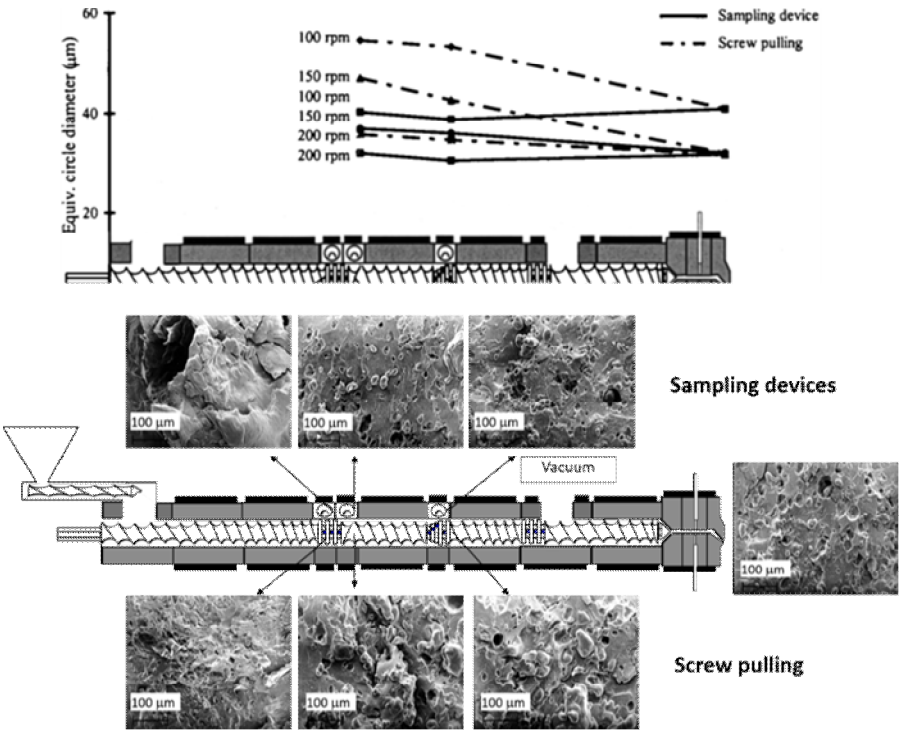

Fig. 6 Evolution of the morphology of a PA6/EPM immiscible blend along the axis of a co-rotating twin extruder, as measured on samples obtained at the same axial locations by sampling devices and screw pulling experiments [28]

Various experimental sampling methodologies have been developed, such as using a split barrel (known commercially as a clamshell extruder), a sliding-barrel, stopping the extruder and pour liquid nitrogen into entry ports, removing molten samples at entry ports with tweezers, or diverging a small amount of material from inside the extruder [4]. The ideal technique should be simple and allow quick access to representative material samples during operation of the extruder, without affecting

the local flow conditions.

Figures 7 and 8 demonstrate the relevance (and sometimes uniqueness) of the information that can be accessed by sampling along the extruder and perform a subsequent characterization in the laboratory. Figure 7 concerns the preparation of a PA-6/EPM-g-MA (80/20) wt% blend (EPM-g-MA denotes EPM with grafted maleic anhydride (MA)) in a twin screw extruder. Because of the screw design and operating conditions, at L/D =12 the PA-6 pellets are embedded in a continuous rubber phase. One screw turn later (L/D=13), the blend is already fully molten, exhibiting the usual matrix/suspended droplets morphology [4, 28]. Interestingly, at L/D=12, using higher magnification unveils a morphology at the PA-6/EPM-*g*-MA interface consisting of stretched, wavelike rubber domains perpendicular to the PA-6 surface, and thin spider-web-like filaments. These features confirm the validity of the dispersion mechanism of liquid-liquid systems proposed by Scott and Macosko [29], which was proposed based mostly on experiments performed in internal batch mixers.

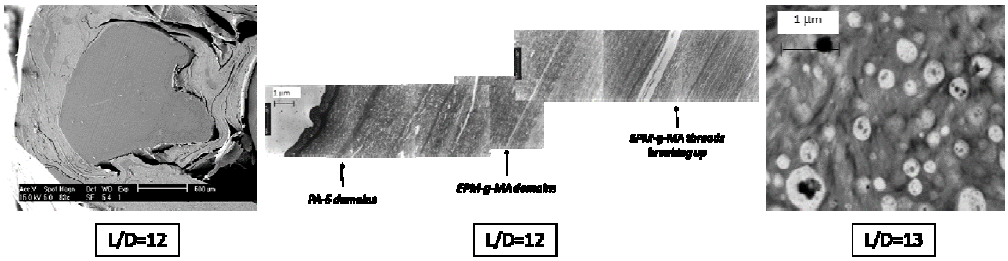

Fig.8 Evolution of the morphology of PA-6/EPM-g-MA (80/20) w/w blends at two consecutive screw turns of a twin-screw extruder (adapted from [4, 28])

Figure 8 refers to the grafting of MA onto polyolefins (polyethylene (PE), EPM and polypropylene (PP) [30]. The graph displays the relative variation of the rheological moduli (G' and G'') along the extruder for the three materials. The reaction is very fast, as can be confirmed by the sharp variation in the rheological responses, with very little change further downstream. The final grafting yield depends on the polyolefin, as a result of the competition between grafting and termination reactions. Specifically, as the ethylene content increases, the chemical mechanisms change from ß-scission of tertiary PP radicals, to small crosslinking in EPM and to severe crosslinking/gel formation, together with some degradation, in the case of PE.

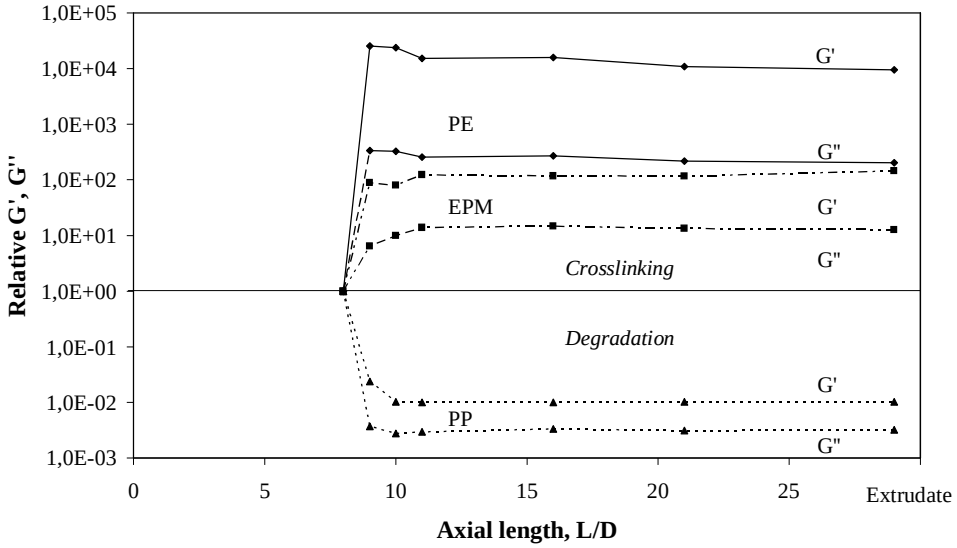

Fig. 9 Evolution of chemical conversion along the axis of a co-rotating twin-screw extruder during reactive grafting of polyolefins with MA. The rheological moduli G' and G'' (at 7 × 10^{-3} Hz) were normalized to the values of the starting materials [30]

4. In-process optical spectroscopy

Radiation at different wavelengths induces a range of molecular motions that can be used to obtain useful information on the polymers analyzed. UV-VIS (0 - 1000 nm) causes electronic transitions that enable assessing the concentration of a particular species. For example, the technique was applied to monitor the process-induced degradation of poly-llactic acid (PLLA) [31]. Within the IR region (12000 – 400 cm^{-1}), the MIR range (4000 to 400 cm^{-1}) is related to molecular vibrations, while NIR (12,000 – 4000 cm^{-1}) includes bands that result from harmonic overtones of fundamental and combination bands linked to hydrogen atoms (which are relevant for compounds containing CH, OH and NH bonds). A change in the absorbance band intensity can be associated to a variation in concentration. MIR was employed to monitor the reaction of styrene-maleic anhydride copolymer with a long chain alkyl amine [32]. Commercial NIR probes work either in transmission or in diffusive reflectance mode (thus enabling on-line and in-line measurements, respectively) (see [33] for a comparison of performance). For example, the technique was adopted to monitor the composition of PP/ethylene vinyl acetate (EVA) copolymer blends [34], to determine the MW of partly glycolised polyethylene terephthalate [35], to follow the graft copolymerisation of MA onto PP [36], to analyze the conversion of a

styrene/maleic anhydride co-polymer [32], to monitor the transesterification of EVA [36], and to investigate the esterification of an ethylene-vinyl-alcohol (EVOH) co-polymer [37]. In order to extract from NIR spectra as much information as possible, calibration models relating the spectral data to reference characterization parameters are developed – this is known as chemometrics. In principle, a single calibration model could yield information on chemical, physical and morphological characteristics, so that NIR could replace several other characterization techniques. However, a change in the material recipe or in the geometry of the extruder usually requires a new calibration of the chemometric model. Figure 10 demonstrates how in-line NIR can be used to monitor the evolution along the axis of the extruder of the level of dispersion of polymer/organoclay nanocomposites. The analysis by X-ray diffraction (a well established technique used to assess the degree of intercalation of this type of systems) of samples collected at various positions along the screws by sampling devices shows that intercalation increases along the screws (perhaps together with exfoliation), but during flow through the die part of the intercalation is apparently reverted (Figure 10a). These results were confirmed by NIR data (Figure 10b). Figure 10b also shows that, as expected, the rate of dispersion increases with increasing screw speed, but reversion of dispersion at the die was always observed. This phenomenon was attributed to the degradation of the clay surfactant that, in combination with lower melt viscosity due to viscous dissipation, facilitated the flow of the polymer out of the clay galleries [38].

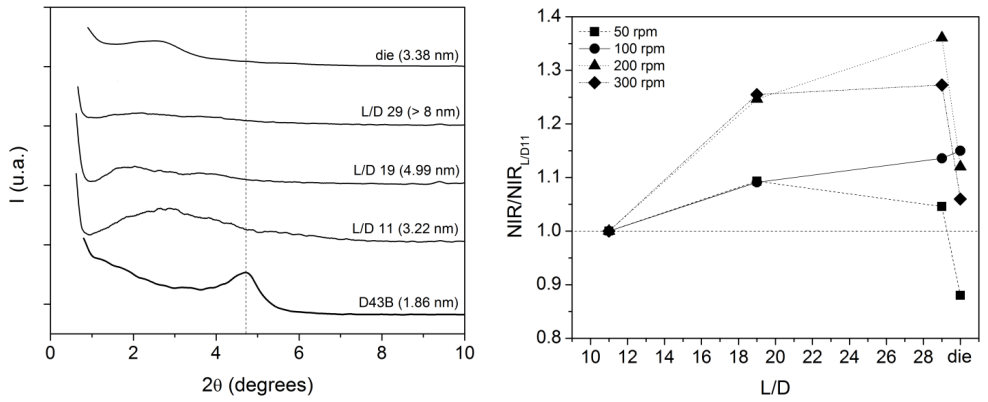

a) b)

Fig 10 Evolution of the dispersion along the screws of a PA6/organoclay (95/5 wt.%) nanocomposite (100 rpm, 3kg/h). a) X-ray diffraction spectra (100 rpm, 3kg/h); b) effect of screw speed on the degree of dispersion as measured by NIR (values along the screw were normalized to the value at L/D=112, where melting

was completed

The absorbance bands of ATR-FTIR spectra can be linked to chemical composition. However, since the technique involves a path length that is much shorter than the depth of the screw or die flow channels, on-line testing is required to obtain data representative of the bulk. The technique was applied to follow PE grafting with organosilanes [39], to follow the thermal degradation of polyoxymethylene (POM) [40] and to evaluate the monomer/polymer ratio during polymerization of ε-caprolactam [41]. Raman spectroscopy detects vibrations modifying the polarizability of a molecule, which enables analyzing the polymer backbone structure and conformation, usually by studying the intensity of the spectral band of interest. The technique was employed to monitor the grafting of glycidyl methacrylate (GMA) onto low density polyethylene (LDPE) [42]. Coates et al [43] used simultaneously on-line MIR, in-line transmission NIR and in-line Raman to monitor the single screw extrusion of HDPE/PP blends and concluded that NIR exhibited the best resolution, although it was challenging to quantify in real time changes in specific bond vibrations.

5. In-process rheometry

The rheological response of a polymer is sensitive to changes of MW, MWD and degree of branching, and to composition, interfacial stress and morphology of polymer blends. An increase in MW causes an increase in viscosity. In small amplitude oscillatory shear (SAOS), the curves of G' and G'' vs. frequency shift horizontally to lower frequencies with increasing MW. The maximum in G', G'' and the cross-over frequency assess the broadness of the MWD. Long-branching increases the shear rate dependence of linear polymers, and can be estimated from measurements of G', of the first normal stress difference N_1, or by measuring the strain hardening effect on the extensional viscosity. Compatibilized blends are usually less shear-thinning than the equivalent immiscible ones. The size of the dispersed droplets in a blend can be estimated from G' and N_1 [44]. The viscosity curves of compatibilized blends generally show two plateau regions, at low and moderate frequencies, the first stemming from interfacial effects. Similarly, an additional slow relaxation process in SAOS on both physical and chemically compatibilized blends was attributed to interfacial elasticity [44]. It becomes therefore evident that using the rheological toolbox by means of in-process monitoring is of great value.

In-line slit rheometry can be used straightforwardly by coupling a rheological die to an extruder. The die contains at least two flush mounted melt pressure transducers along the slit. Melt viscosity can be determined from measurements of throughput and of the lengthwise pressure difference. N_1 can be estimated from the hole-

pressure or exit pressure methods, but these require highly accurate experiments that may be difficult to perform in an industrial production environment [45]. The slit geometry can also easily accommodate flush mounted optical windows, for example to use SALS or polarized optical microscopy to obtain structural and morphology information or UV-fluorescence transducers to measure RTD. Figure 11 exhibits the shear viscosity, N_1 and SALS patterns as a function of shear rate for a PS/PMMA 98/2 wt.% blend [22]. SALS patterns exhibit an ellipsoid superimposed on a streak, both oriented normal to the flow direction, that are typically associated to the presence of a morphology consisting of elongated (ellipsoidal) droplets and filaments or strings (streaks). The pattern becomes more ellipsoidal with increasing shear rate, indicating more droplet elongation along the flow and the streak becomes more intense and thinner.

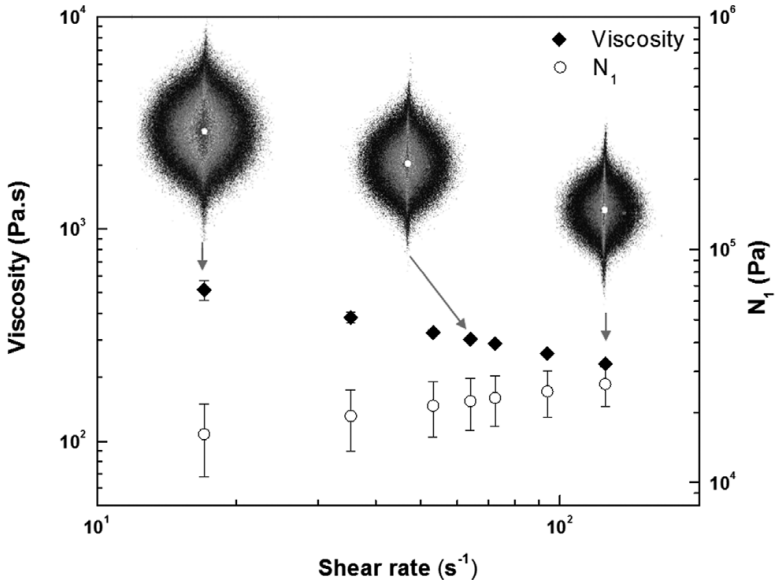

Fig. 11 Shear viscosity, N_1 and SALS patterns as a function of shear rate for a PS/PMMA 98/2 wt.% blend processed at 230 ºC (flow develops in the horizontal direction) (adapted from [22])

In-line slit rheometry also has some significant drawbacks. Coupling a slit die to an extruder eliminates the possibility of extruding products with other cross-sections, making this set-up mostly adequate for R&D work. Also, the real melt temperature along the die is unknown, not only because of the inherent viscous dissipation, but

also due to the fact that the thermomechanical history of the material in the extruder cannot be instantly relaxed up to the die entry. More importantly, measuring both the extrusion throughput and pressure drop will yield a single point of the viscosity vs. shear rate curve. To generate a range of shear rates, the output of the extruder must be changed, which will modify the thermomechanical history of the material inside the machine. In turn, this may lead to changes in chemical conversion, homogeneity, thermal stability and/or morphology, i.e., at each shear rate a different material would be characterized. To evade this problem, several variant slit die designs allowing to acquire various points of the flow curve in a single extrusion experiment have been suggested (for a review see [46]). For example, in the twin-slit design adopted by Teixeira *et al* [46] (Figure 12) the inlet flow channel contains a melt pressure transducer and is divided into two parallel slits, one being used for the measurements (and containing at least two melt pressure transducers along its length). Two vertically moving valves are located at the entrance of each channel. It is possible to change the shear rate at the measuring channel while keeping constant the total pressure drop in the die by moving its valve in one direction, and simultaneously adjust as necessary the other valve in the opposite direction.

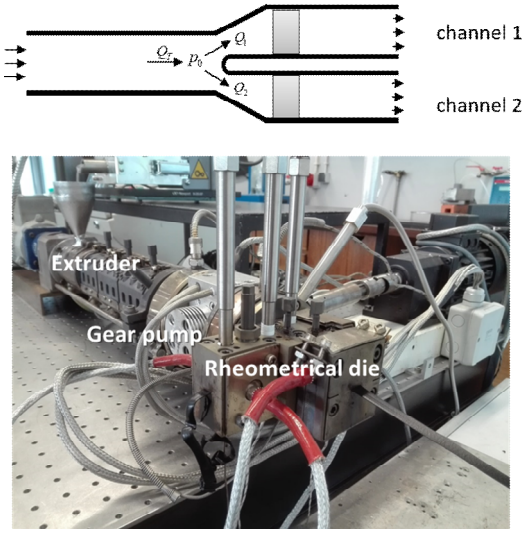

Fig. 12 Twin-slit rheometrical die: concept (top) and practical construction (bottom). The two channels are set at 90º. A gear pump is used to stabilize the flow from the extruder

On-line capillary rheometers analyze a material stream that was detoured from the

main flow channel, usually between extruder and die. In this way, the melt can be conditioned to the required testing temperature prior to the measurement and the shear rate can be changed independently. Various commercial solutions are available and used in production environment (see example in Figure 13). They vary in design, working ranges of shear stress and shear rate, time delay between sample collection and measurement, single vs. multiple measurements in parallel or in series (e.g. to perform the Bagley correction for end effects), amount of sample needed, and whether the material is wasted or returned to the main flow. Usually, a gear pump controls accurately the flow rate in the testing chamber, where the pressure drop is measured. A few instruments have interchangeable measuring geometries, allowing to switch between slits and capillaries. The latter are more popular, as they are easier to clean, provide a wider measuring range under moderate pressures and are more suitable to determine the MFI.

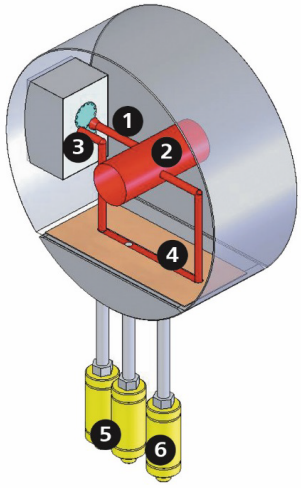

Fig. 13 Gneuss VIS on-line capillary rheometer: 1 – bypass; 2- main melt flow; 3 – gear pump; 4 – measuring geometries; 5 – temperature sensor; 6 - pressure transducers [47].

On-line capillary rheometry along the extruder is also possible. The device shown in Figure 14a is secured to a modified extruder barrel containing a channel linking the inner barrel wall to the reservoir of the rheometer. The instrument comprises the measuring head of a commercial rotational rheometer, a heated body, a replaceable die and a moving ram. The rotational movement of the rheometer shaft is converted into a linear vertical ram movement, while the torque is recorded and used to determine the apparent wall shear stress [48]. This prototype was used to monitor effect of peroxide content on the shear viscosity of PP along the extruder axis

(Figure 14b) [49]. The reaction is extremely rapid, and the higher the peroxide content, the lower the shear viscosity due to chain scission.

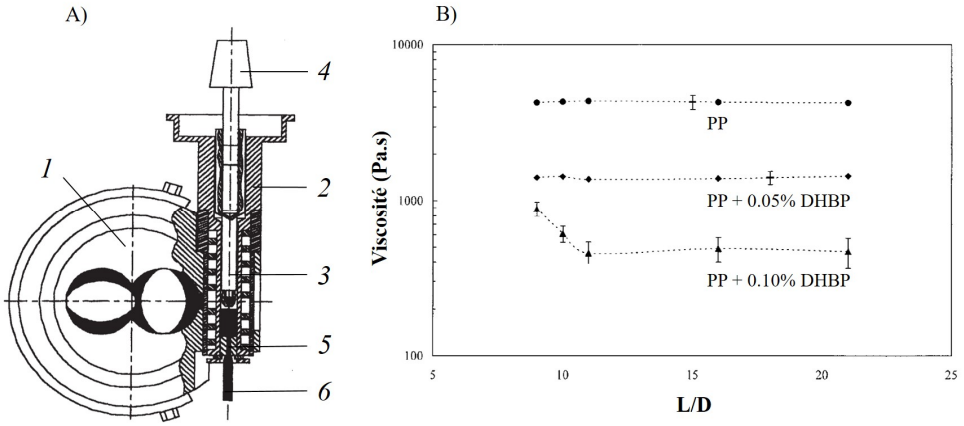

Fig. 14 On-line capillary rheometer. A) The instrument coupled to the modified barrel of an extruder(1 – extruder barrel; 2 – rheometer body; 3 – ram; 4 - rheometer shaft; 5 – capillary die; 6 – extrudate); B) influence of peroxide (2,5-bis(tert-butylperoxy)-2,5-dimethylhexane (DHBP)) content on the axial evolution along the extruder of the shear viscosity of PP [48,49]

Oscillatory rheometry is a convenient technique to characterize multiphase systems as it preserves the material morphology due to the small deformations involved, unlike capillary or slit rheometries. Commercial equipment is available, but the operational window is usually unsuitable to the practical temperatures/viscosity values required for polymer melts. Figure 15a presents the concept of an on-line rotational rheometer that can be coupled to a modified extruder barrel with the sensing capacities and testing modes of a conventional laboratory instrument [50,51]. The device controls the position of the lower plate, admits the material sampled and moves vertically a ring cleaning the outer surface of the test disk. A commercial rotational rheometer head executes the experiments. Figure 15b plots data obtained with this apparatus concerning the evolution of G' and G'' along the extruder for PLA and the same PLA with a chain extender (CE). As expected, the rheological moduli for PLA+CE are larger than those for neat PLA. The reaction took place upstream very quickly, upon melting. Further downstream, a slight reduction in the moduli is consistently observed and probably caused by thermal degradation.

In-process rheometers can also generate extensional flows. Superimposed shear and extensional flows develop in "zero length" or short convergences. Hyperbolically

converging dies induce uniform elongation rates [52]. The extensional viscosity can be extracted whan applying the well-known Cogwell [53] or Binding [54] analyses. Convergences can be created simply by joining two consecutive slits with different heights [55-58]. Kracalik et al [59] used a Rheotens (a device that pulls filaments by means of four rotating wheels connected to a displacement sensor [60]) to stretch extrudates. Figure 16 reports an on-line variant of this method, which can be applied along the axis of the extruder [61].

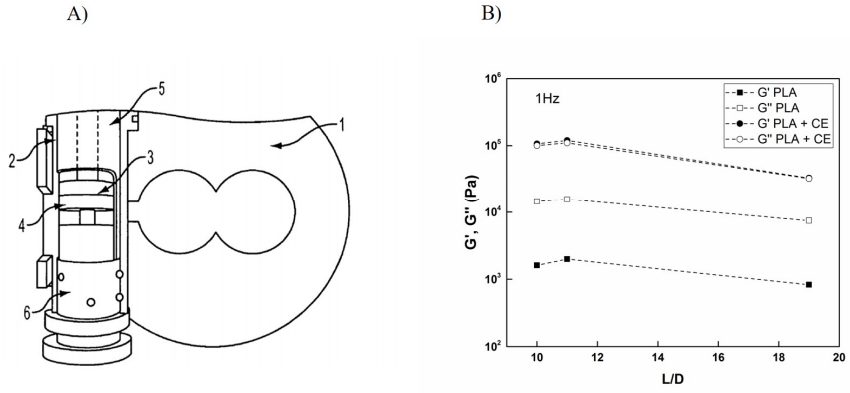

Fig. 15 On-line rotational/oscillatory rheometry. A) Rheometer coupled to the modified barrel of an extruder (1), consisting of a body (2), a cleaning ring (5), a lower support (6) and top (3) and bottom (4) parallel plates; rotation of (2) admits material from the extruder; the top plate (3) rotates/oscillates via coupling to the head of a commercial rheometer; B) progress of G' and G'' along the extruder for PLA and PLA with chain extender (CE)

6. Conclusions

In-process measurements in extrusion and compounding aim at obtaining information in real time about the characteritics of the materials that are being processed, rather than monitoring process variables that relate to flow and heat transfer conditions in the extruder, which is the approach of conventional instrumentation. Therefore, they must necessarily encompass a wide range of techniques. This chapter summarized approximately 30 years of efforts of many teams in academia and industry to develop in-line and on-line instruments and measuring techniques capable of extracting quickly relevant, representative, precise and reliable material data. A few application examples were discussed. Emphasis is given on the work carried out at the University of Minho, Portugal.

In-process monitoring techniques have gradually convincingly demonstrated their

usefulness both for R&D and production, particularly for material development and quality control. The future will certainly involve the implementation of smart process control on the basis of material attibutes and, for this purpose, in-processing messurements are indispensable. Therefore, the utilization of in-process monitoring in extrusion and compounding processes is expected to growth sunbstantially in the next coming years.

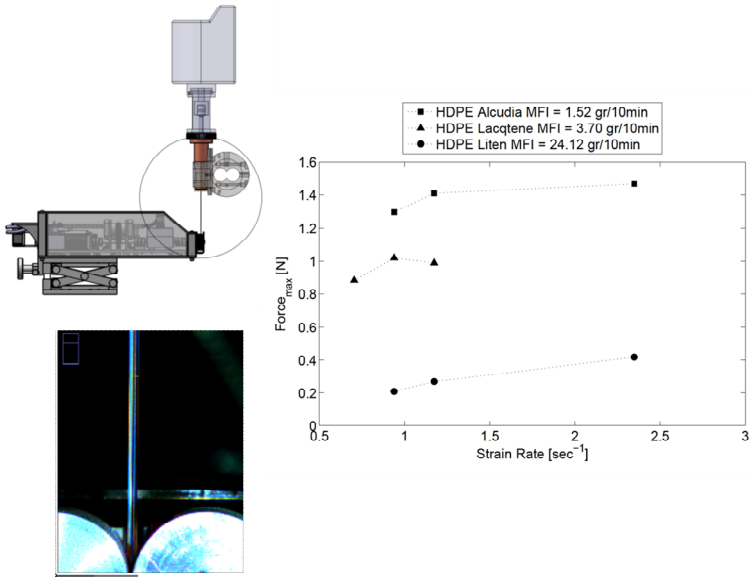

Fig. 16 On-line extensional rheometry. Schematic view of the device and image processing of a filament being stretched (left), and maximum stretching force at different strain rates for HDPE with various MFI (right) [61]

References

[1] K. Kohlgrüber, Co-Rotating Twin-Screw Extruders: Fundamentals, 2007, Hanser

[2] C. Rauwendaal, Polymer Extrusion, 2014, Hanser

[3] Z. Tadmor, C. Gogos, Principles of Polymer Processing, 2012, Wiley-Interscience

[4] A. V. Machado, J. A. Covas, M. van Duin, Evolution of Morphology and of Chemical Conversion along the Screw in a Corotating Twin Screw Extruder, J. Appl. Polym. Sci., 1999, 71, 135-141

[5] F. Berzin, F, A. Tara, L. Tighzert, B. Vergnes, Importance of Coupling Between Specific Energy and Viscosity in the Modeling of Twin Screw Extrusion of Starchy Products, Polym. Eng. Sci, 2010, 50, 1758-1766

[6] C. Martin, Twin Screw Extrusion for Pharmaceutical Processes, chapt.2 in M. A. Rapka, N. Langley, J. DiNunzio (eds.) Materials, Technology and Drug Product Design, 2013, Springer
[7] O. S. Carneiro, J. A. Covas, B. Vergnes, Experimental and Theoretical Study of Twin Screw Extrusion of Polypropylene, J. Appl. Polym. Sci., 2000, 78, 1419-1430
[8] J. A. Covas, In-process Measurements for Reactive Extrusion Monitoring and Control, in G. Beyer, C. Hopmann, (eds.) Reactive Extrusion: Principles and Applications, 2018, Wiley-VCH Verlag GmbH & Co. KGaA, 101-132
[9] S.E. Barnes, M.G. Sibley, H.G.M. Edwards, P.D. Coates, Process monitoring of polymer melts using in-line spectroscopy, Trans. Inst. Measur. Control, 2007, 29, 453-465
[10] K.B. Migler, A.J. Bur, Fluorescence based measurement of temperature profiles during polymer processing, Polym. Eng. Sci., 38, 1998, 213-221
[11] O.S. Carneiro, J. A. Covas, J. A. Ferreira, M.F. Cerqueira, On-Line Monitoring of the Residence Time Distribution Along a Kneading Block of a Twin-Screw Extruder, Polym. Testing, 2004, 23, 925-937
[12] P. F. Teixeira, J. A. Covas, J. M. Maia, L. Hilliou, In-line particle size assessment of polymer suspensions during processing, Polym. Testing, 2014, 37, 68-77
[13] P.F. Teixeira, F. Sutera, R. Scaffaro, J.A. Covas, L. Hilliou, Multi-parameter in-process monitoring of clay dispersion during melt compounding with PLA, eXPRESS Polym. Lett., 2019, 13, 276–285
[14] A.M. Cunha Santos, C.A. Cáceres, L.S. Calixto, L. Zborowski, S.V. Canevarolo, In-line Optical Techniques to Characterize the Polymer Extrusion, Polym. Eng. Sci., 2014, 54, 386-395
[15] K. Soares, A.M. Cunha Santos, S.V. Canevarolo, In-line rheo-polarimetry: A method to measure in real time the flow birefringence during polymer extrusion, Polym. Testing, 2011, 30, 848-855
[16] R. Kotzé, J. Wiklund, R. Haldenwang, Optimisation of Pulsed Ultrasonic Velocimetry system and transducer technology for industrial applications, Ultrasonics, 2013, 53, 459-469
[17] S. Perusich, M. McBrearty, Dielectric spectroscopy for polymer melt composition measurements, Polym. Eng. Sci., 2000, 40, 214-226
[18] A. Boersma, J. van Turnhout, Dielectric on-line spectroscopy during extrusion of polymer blends, Polymer, 1999, 40, 5023-5033
[19] J. A. Covas, O. S. Carneiro, J. M. Maia, S. A. Filipe, A. V. Machado, Evolution of Chemistry, Morphology and Rheology of various Polymer Systems along a Twin-Screw Extruder, CJChe, 2002, 80, 1065-1074
[20] J. A. Covas, O. S. Carneiro, P. Costa, A. V. Machado, J. M. Maia, On-line monitoring techniques for studying the evolution of physical, rheological and chemical effects along the extruder, Plast. Rubb. Comp. Macromol. Eng., 2004, 33, 55-61
[21] J. A. Covas, A. V. Machado, Monitoring reactive processes along the extruder,

Int. Polym. Proc., 2005, XX, 2, 121-127
[22] P. F. Teixeira, J. M. Maia, J. A. Covas, L. Hilliou, A small-scale experimental extrusion set-up for exploring relationships between process-induced structures and characteristics of multiphase polymer systems, Macromol. Mat. Eng., 2015, 300, 1278–1289
[23] J.M. Dealy, T.O. Broadhead, Process Rheometers for Molten Plastics: A Survey of Existing Technology, Polym. Eng. Sci., 1993, 33, 1513-1523
[24] L. Saerens, C. Vervaet, J.-P. Remon, T. De Beer, Process monitoring and visualization solutions for hot-melt extrusion: a review, J. Pharm. Pharmacol., 2014, 66, 180-203
[25] P. Cassagnau, V. Bounor-Legaré, F. Fenouillot, Reactive Processing of Thermoplastic Polymers: A Review of the Fundamental Aspects, Int.. Polym. Proc., 2007, XXII, 218-258
[26] I. Alig, B. Steinhoff, D. Lellinger, Monitoring of polymer melt processing, Meas. Sci. Technol., 2010, 21, 062001
[27] M. A. Huneault, M. F. Champagne, A. Luciani, Polymer blend mixing and dispersion in the kneading section of a twin-screw extruder, Polym Eng Sci., 1996, 36, 1694-1706
[28] A.V. Machado, J. A. Covas, M. van Duin, Effect of Composition and Processing Conditions on Chemical and Morphological Evolution of PA-6/EPM/EPM-g-MA Blends in a Twin Screw Extruder, J. Appl. Polym. Sci., 2001, 80, 1535-1546
[29] C.E. Scott, C.W. Macosko, Model Experiments Concerning Morphology Development During the Initial Stages of Polymer Blending, Polymer Bulletin, 1991, 26, 341-348
[30] A. V. Machado, J. A. Covas, M. van Duin, A Study of Grafting Reactions during Processing of Polyolefins, Adv. Polym. Tech., 2004, 23, 196-204
[31] Y. Wang, B. Steinhoff, C. Brinkmann, I. Alig, In-line monitoring of the thermal degradation of poly(L-lactic acid) during melt extrusion by UV-vis spectroscopy, Polymer, 2008, 49, 1257-1265
[32] L. Jakisch, D. Fischer, M. Stephan, K. J. Eichhorn, In-line-analytik von polymerreaktionen, Kunststoffe, 1995, 85, 1338-1344
[33] J.M. Barbas, A. V. Machado, J. A. Covas, In-line Near-Infrared Spectroscopy: a tool to monitor the preparation of Polymer-Clay Nanocomposites in Extruders, J. Appl. Polym. Sci., 2012, 127, 4899-4909
[34] D. Fischer, T. Bayer, K.-J. Eichhorn, M. Otto, In-Line Process Monitoring on Polymer Melts by NIR-Spectroscopy, J. Analyt. Chem., 1997, 359, 74-77
[35] B. Bergmann, W. Becker, J. Diemert, P. Elsner, On-Line Monitoring of Molecular Weight Using NIR Spectroscopy in Reactive Extrusion Process, Macromol. Symp., 2013, 333, 138-141
[36] L. Moghaddam, L. Rintoul, P. J. Halley, G. A. George, P. M. Fredericks, In-situ monitoring by fibre-optic NIR spectroscopy and rheometry of maleic anhydride grafting to polypropylene in a laboratory scale reactive extruder, Polym. Testing,

2012, 31, 155-163
[37] S. Sasic, Y. Kita, T. Furukawa, M. Watari, H. W. Siesler, **Y.** Ozaki, Monitoring the melt-extrusion transesterification of ethylene-vinylacetate copolymer by self-modeling curve resolution analysis of on-line near-infrared spectra, Analyst, 2000, 125, 2315-2321
[38] J. M. Barbas, A. V. Machado, J. A. Covas, Evolution of Dispersion Along the Extruder During the Manufacture of Polymer-Organoclay Nanocomposites, Chem. Eng. Sci, 2013, 98, 77-87
[39] H.-G. Fritz, S. Ultsch, Sensorentwicklung und Automatisierungstendenzen bei der Kunststoffaufbereitung, Kunststoffe, 1989, 79, 785-790
[40] V. V. Rajan, R. Waber, J. Wieser, Online Monitoring of the Thermal Degradation of POM During Melt Extrusion, J. Appl. Polym. Sci., 2010, 115, 2394-2401
[41] E. Haberstroh, L. Jakisch, E. Henuge, P. Schwarz, Real-Time Monitoring of Reactive Extrusion Processes by Means of In-Line Infrared Spectroscopy and Infrared Temperature Measurement, Macromol. Mat. Eng., 2002, 287, 203-208
[42] K. Jarukumjorn, K. Min, On-line monitoring of free radical grafting in a model twin screw extruder, SPE ANTEC 2000, 2064-2067
[43] P.D. Coates, S.E. Barnes, M.G. Sibley, E.C. Brown, H.G.M. Edwards, I.J. Scowen, In-process vibrational spectroscopy and ultrasound measurements in polymer melt extrusion, Polymer, 2003, 44, 5937-5949
[44] P. Van Puyvelde, S. Velankar, P. Moldenaers, (2001) Rheology and morphology of compatibilized polymer blends, Current Opinion Colloid Interf. Sci., 2001, 6, 457-463
[45] P.F. Teixeira, L. Hilliou, J.A. Covas, J.M. Maia, Assessing the practical utility of the hole-pressure method for the in-line rheological characterization of polymer melts, Rheol. Acta, 2013, 52, 661-672
[46] P.F. Teixeira, L.L. Ferrás, L. Hilliou, J.A. Covas, A new double-slit rheometrical die for in-process characterization and extrusion of thermo-mechanically sensitive polymer systems, Polym. Testing, 2018, 66, 137-145
[47] A. Hannemann, Online Viscometer VIS, Technical Report #E10, 2017, Gneuss Kunststofftechnik GmbH
[48] J. A. Covas, J.M. Nóbrega, J. M. Maia, Rheological measurements along an extruder with an on-line capillary rheometer, Polym. Testing, 2000,19, 165-176
[49] A. V. Machado, J. M. Maia, S. V. Canevarolo, J. A. Covas, Evolution of Peroxide-Induced Thermomechanical Degradation of Polypropylene Along the Extruder, J. Appl. Polym. Sci., 2004, 91, 2711-2720
[50] J.A. Covas, J.M. Maia, A.V. Machado, P. Costa, On-line rotational rheometry for extrusion and compounding operations, J. Non-Newt. Fluid Mech., 2008, 148, 88-96
[51] S. Mould, J. M. Barbas, A.V. Machado, J.M. Nóbrega, J.A. Covas, Measuring the rheological properties of polymer melts with on-line rotational rheometry, Polym. Testing, 2011, 30, 602-610

[52] D. G. Baird, J. Huang, Elongational Viscosity Measurements Using a Semi-Hyperbolic Die, Appl Rheology, 2006, 16, 312-320
[53] F.N. Cogswell, Converging flow of polymer melts in extrusion dies, Polym. Eng. Sci., 1972, 12, 64-73
[54] D.M. Binding, An approximate analysis for contraction and converging flows, J. Newt. Fluid Mech., 1988, 27, 173-189
[55] M.T. Martyn, C. Nakason, P.D. Coates, Measurement of apparent extensional viscosities of polyolefin melts from process contraction flows, J. Non-Newt. Fluid Mech., 2000, 92, 203-226
[56] T. Kopplmayr, H.-J. Luger, I. Burzic, M. G. Battisti, L. Perko, W. Friesenbichler, J. Miethlinger, A novel online rheometer for elongational viscosity measurement of polymer melts, Polym. Testing, 2016, 50, 208-215
[57] H.-J. Luger, J. Miethlinger, Development of an online rheometer for simultaneous measurement of shear and extensional viscosity during the polymer extrusion process, Polym Testing, 2019, 77, 105914
[58] https://extruders.leistritz.com/en/extruders-systems/control-and-measuring-technology/leistritz-elongational-rheometer.html
[59] M. Kracalik, S. Laske, A. Witschnigg, C. Holzer, Elongational and shear flow in polymer-clay nanocomposites measured by on-line extensional and off-line shear rheometry, Rheol Acta, 2011, 50, 937–944
[60] https://www.goettfert.com/products/elongation-testing/rheotens.html
[61] N. Donato, A contribution to the on-line extensional characterization of polymer melts, EURHEO-EMMC M.Sc Thesis, 2012, University of Minho, Portugal